# Fluoride Ion Batteries – Past, Present, and Future

Mohammad Ali Nowroozi[a,§], Mohammad Irshad[b,§], Palanivel Molaiyan[c,§], Kerstin Wissel[a,§], Anji Reddy Munnangi[d,*] and Oliver Clemens[a,*]

[a] Universität Stuttgart, Institut für Materialwissenschaft, Chemische Materialsynthese, Heisenbergstraße 3, 70569 Stuttgart, Germany

[b] Université Paris-Saclay, CEA, CNRS, NIMBE, LEEL, 91191, Gif-sur-Yvette, France

[c] Institute of Particle Technology, Technical University of Braunschweig, Volkmaroder Str. 5 38104 Braunschweig, Germany.

[d] College of Engineering, Swansea University, Fabian Way, Swansea SA1 8EN, United Kingdom

[§] These authors contributed equally

**Abstract**

Fluoride-Ion Batteries (FIBs) have been recently proposed as a post-lithium-ion battery system. This review article presents recent progress of the synthesis and application aspects of the cathode, electrolyte, and anode materials for fluoride-ion batteries. In this respect, improvements in solid-state electrolytes for FIBs as well as liquid electrolytes will be discussed. Furthermore, the achievements regarding the development of cathode and anode materials will be considered. With the improvements made, the field is currently attracting a steady increase of interest, and we will discuss the potentials of this technology together with necessary future milestones to be achieved in order to develop FIBs for future energy storage.

**Keywords:** fluoride ion batteries, liquid electrolytes, solid-state electrolytes, ionic conductivity, intercalation-based cathode materials, conversion-based cathode materials, intercalation-based anode materials, conversion-based anode materials

# 1 Introduction

Modern life is highly dependent on energy storage devices. From portable electronics to electric vehicles (EVs), electric trains and airplanes, which may or may not become the future of mobility, all benefit from modern rechargeable energy storage technologies. Moreover, energy storage devices are required to store the energy generated from solar, wind, and tidal sources. Therefore, the demand for efficient and sustainable systems is increasing drastically.

Lithium-ion batteries (LIBs) turned out to be the best choice for portable electronics and are the main contenders for emerging EVs due to their high energy density, specific power, and cycling stability.[1] However, the large adoption of LIBs for these applications led to the depletion of lithium resources, which are low in abundance and geometrically constrained. Not only the abundance of lithium, but also the abundance of other key elements (e. g., Co) used in LIBs is critical. Even if cobalt-free and high energy nickel-rich materials have been developed recently, the safety and thermal stability of such Ni-rich materials is a concern. Though this might not necessarily impact small scale technologies, these aspects will become of tremendous importance for large scale storage. In this context, it is important to consider alternative energy storage systems, which work based on shuttling ions other than $Li^+$ and might also lead to the use of other elements within the electrode materials.

In response, several alternative battery technologies were proposed and investigated. Alternative rechargeable battery systems, which perform based on shuttling of ions other than $Li^+$, have been investigated so far, including sodium-ion batteries (NIBs)[2, 3], magnesium-ion batteries[3, 4], calcium-ion batteries[5] and aluminum-ion batteries.[6] For these systems, the shuttling ions possess low standard reduction potentials (i.e., the ionic species can be reduced, but not oxidized), which are similar to lithium. In contrast, chloride-ion batteries[7] and fluoride-ion batteries (FIBs)[8] rely on shuttling ions with potentials at the other side of electromotive force (EMF) series (i.e., those species can be oxidized, but not be reduced). Fluorine has a lower atomic mass (18.9984 u[9]) as compared to $Na^+$ (22.9897 u[9]), $K^+$ (39.0983 u[9]). Therefore, FIBs potentially may reach higher gravimetric energy densities as compared to recently emerged rechargeable battery systems of sodium ion batteries and potassium ion batteries. Figure 1 compares the gravimetric and volumetric energy densities (these energy densities are theoretical and on the material basis), from which it can be seen that FIBs would be in principle favourable to LIBs in this respect. The volumetric energy density of FIBs is particularly high which is of interest for EV and large scale storage applications. Besides the high energy density, batteries based on a fluoride shuttle offer some further unique features. Fluorine is the strongest oxidizing agent and most electronegative element in the periodic table and consequently, the fluoride ion is a very redox-stable anion, which enables a wide electrochemical potential window. In this respect, FIBs can potentially provide a higher open circuit voltage as compared to sodium ion batteries and most of other multivalent batteries such as magnesium and aluminum ion batteries. Moreover, recent development in liquid electrolytes for FIBs proves that aqueous and non-aqueous liquid electrolytes can be used to build up FIBs. However, FIBs can also be made in all-solid-state modification. Therefore, safety issues as found in the Li-ion battery technology due to metal dendrite growth become irrelevant for FIBs. Additionally, fluoride containing materials are globally more abundant as compared to lithium reserves.[10]

In this review, the advancement of FIBs and their components, including solid and liquid electrolytes and electrode materials from the early stages to the most recent studies are presented. Further, recent advances in FIB chemistry and systems, fluoride-ion-transport mechanisms, and fundamental properties of solid-state/liquid fluoride electrolytes for FIBs will be discussed. Given the importance of next-generation energy storage applications and perspectives, challenges, opportunities, and potentials for future research directions will be highlighted.

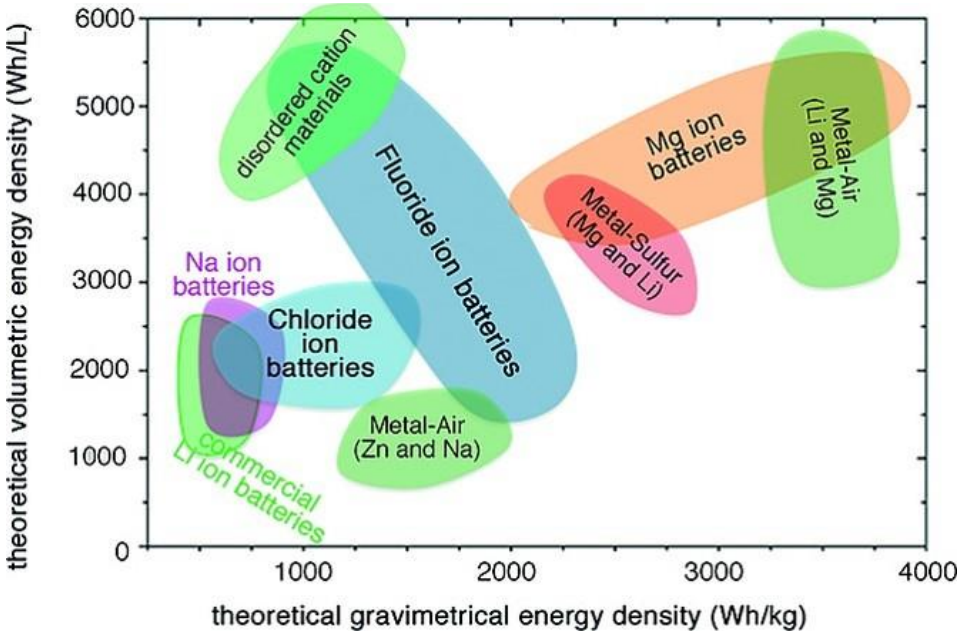


*Figure 1. Overview of secondary ion batteries for future battery technologies.[11] The charge transfer ions can be distinguished into cationic shuttles (such as $Li^+$, $Na^+$, and $Mg^{2+}$), and anionic shuttles (such as $Cl^-$ and $F^-$), providing a wide variety of different battery types. From bottom left to upper right: commercial Li-ion batteries (LIBs), sodium-ion batteries (SIBs), chloride-ion batteries (CIBs), Zn-air batteries, Na-air batteries, fluoride-ion batteries (FIBs), metal-sulphur batteries (with Mg and Li as the anode), magnesium-ion batteries, and top right for lithium-air and magnesium-air batteries. Reproduced from ref.[11] with permission[i].*

## 2 Early Work on Fluoride-ion Batteries

FIBs have been first proposed in the 1970s, and at the time they were mostly referred to as fluoride galvanic cells. Baukal[12] claimed that $CaF_2$ could serve as a solid electrolyte in an all-solid-state FIB in a high temperature range of 400 – 500 °C. However, no experimental results on the operation of a full cell were reported. Kennedy and Miles[13] showed the first experimental observation of an electrochemical cell based on shuttling of fluoride ions, using KF-doped β-$PbF_2$ as a solid electrolyte in $CuF_2$|β-$PbF_2$|Pb and AgF|β-$PbF_2$|Pb electrochemical cells. Although the observed starting potentials (0.70 V and 1.3 V for $CuF_2$|Pb and AgF|Pb cells, respectively) were close to the open cell voltage (OCV) (Pb + $CuF_2$ ⟶ $PbF_2$ + Cu; $\Delta E°$ = 0.72 V; Pb + 2 AgF ⟶ $PbF_2$ + 2 Ag; $\Delta E°$ = 1.32 V), poor capacities were observed. This has been related to strong polarizations which have been suggested to be a result of the formation of the α-$PbO_2$ phase in the anode material leading to a poor ionic conductivity of the cell. They also reported on discharging of a thin-film cell made up of $CuF_2$, Pb, and $PbF_2$ cathode, anode, and electrolyte

[i] 2017 WILEY-VCH Verlag GmbH & Co. KGaA, Weinheim

materials, respectively.[14] Results revealed that discharge capacities as large as ~ 40% of the theoretical capacity of $CuF_2$ (528 mAh $g^{-1}$) could be obtained, though further charging of the cell could not be achieved.

In 1976 Schoonman[15] reported on building a Pb|β-$PbF_2$:AgF|$BiO_{0.09}F_{2.82}$|Bi cell, which was fabricated by spring-loading the disks of Pb and Bi, which were painted with powders of β-$PbF_2$, AgF or $BiO_{0.09}F_{2.82}$, respectively, from dispersions in ethyl acetate. The observed discharge potential (0.330 – 0.335 V) was close to the OCV (0.37 V), showing that oxyfluorides can principally be candidates for the electrolyte materials in FIBs. However, no further information about the reversibility of the cell was reported. Following Schoonman's work, in 1978 Danto et al. reported on the reversible cycling of thin-film solid-state galvanic cells with a mean thickness of 0.55 µm made up of Pb as the anode, Bi/$BiF_3$ as the cathode, and $PbF_2$ (cubic β-$PbF_2$) as the electrolyte.[16] The measurements were performed at room temperature. They reported on a starting discharge potential as high as 353 mV, followed by a flat discharge plateau at around 280 mV for a current density of 40 µA/$cm^2$.

Investigations on the electrolytes for fluoride-ion galvanic cells were followed up by Schoonman. In 1979 he reported[17] on the solid solution based electrolyte $M_{1-x-y}U_xCe_yF_{2+2x+y}$ (M = Ca, Sr, Ba) for thin-film galvanic cells with $BiF_3$ and Ca as cathode and anode materials, respectively.

In 1981, the term solid-state fluoride-ion battery had been used for the first time by Schoonman and Wolfert.[18, 19] In these publications, they reported on improvements in ionic conductivity of $CaF_2$ anodes by doping with La or Yb (for instance forming the corresponding fluoride $Ca_{1-x}La_xF_{2+x}$).

## 3 Re-introduction of Rechargeable Fluoride-Ion Batteries: A Proof of Principle

Between 1981 and 2011, not much has been done in the field of FIBs. However, in 2011 FIBs attracted some attention again, when Reddy and Fichtner reported on reversible all-solid-state conversion-based FIBs using metal/metal fluoride electrode materials along with Ba doped $LaF_3$ ($La_{1-x}Ba_xF_{3-x}$) as a solid-state electrolyte. They were able to operate FIBs at elevated temperatures (~ 150 – 200 °C) with comparatively short life cycling performances. This study opened new horizons for battery technologies by introducing new battery chemistry. The cathodic and anodic reactions during discharging of a cell can be written as follows (also see Figure 2):

At cathode side: $xe^- + MF_x \longrightarrow M + xF^-$;

At anode side: $xF^- + M' \longrightarrow M'F_x + xe^-$.

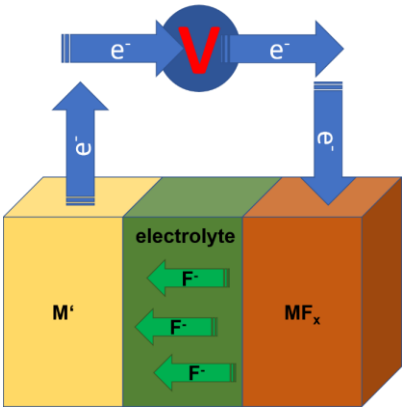


*Figure 2. A schematic illustration of the metal/metal fluoride conversion based FIB proposed by Reddy and Fichtner[8].*

In that study, it was shown that doping of Ba into tysonite-type $LaF_3$ results in a significant increase (roughly two orders of magnitude) of the ionic conductivity compared to the undoped state, and that this increase is necessary to obtain current densities reasonable high to achieve C-rates of ~ C/25 to C/50 to make testing at lab scale feasible. Results suggest that $La_{0.9}Ba_{0.1}F_{2.9}$, which was produced by mechanochemical milling of $BaF_2$ and $LaF_3$, has the highest ionic conductivity among all other $La_{1-x}Ba_xF_{3-x}$ ($0 \leq x \leq 0.15$) compounds (about $2.8 \times 10^{-4}$ S $cm^{-1}$ at 160 °C)[8] with a good electrochemical stability due to the low electrochemical potentials of $Ba^{2+}$ and $La^{3+}$. Various metal fluorides including $CuF_2$, $BiF_3$, $SnF_2$, and $KBiF_4$ were tested as cathode materials against Ce metal to make all-solid-state FIBs in their charged states. Since most of the electrode materials (e.g., $BiF_3$ and $CuF_2$) suffered from low ionic and electronic conductivity, they were mixed with the solid electrolyte and carbon for better electrochemical performance, and their conversion between the metal and metal fluoride state could be well confirmed with diffraction studies.

After this proof-of-concept paper, research on FIBs has gained increased attention over the last years, with studies appearing in the field of electrolyte (solid and liquid), electrode (conversion and intercalation), and cell design development. In the following, we will summarize the attempts that have been made together with the key findings.

## 4 Solid Electrolytes for FIBs

Solid-state batteries have certain advantages compared to liquid electrolyte batteries, particularly concerning safety. To operate solid-state batteries, solid electrolytes (SEs) are required. Interestingly, fluoride ions show a high mobility in the solid-state. Though the ionic size of $F^-$ is large (~ 1.33 Å)[20] it shows significant high mobility in solids, due to its monovalency and low charge density. Indeed, there are several solid fluoride conducting electrolytes that show significantly high conductivities at RT. For example, $PbSnF_4$ has an ionic conductivity of $1 \times 10^{-3}$ S $cm^{-1}$ at RT, which is well beyond the garnet based solid electrolytes for LIBs.[21] Apart from a high ionic conductivity, the electrolyte in a battery should fulfill certain criteria: Suitable electrolyte candidates must exhibit high ionic conductivity with a negligible electronic conductivity to avoid self-discharging of the cell.[22] They should possess a high electrochemical stability window, i.e., they must be electrochemically stable within the operating voltage of the cell. The electrolyte must be chemically compatible with the electrode materials (cathode and anode) to ensure fast ion transport of the charged species across the interfaces, which does not only require stability

towards redox reactions, but also an ion exchange within acid-base type of reactions. Further, SEs should possess certain mechanical properties, e.g., sufficient flexibility and softness, required for the fabrication of a solid state battery.

Most of the studies on fluoride-conducting electrolytes were carried out on single crystals. Some of the fluoride conducting single crystals show a high ionic conductivity. For example, barium doped lanthanum fluoride shows a fluoride ion conductivity in the order of $10^{-4}$ S $cm^{-1}$

, which is suitable to operate solid-state batteries with respect to the commonly encountered aspect ratios and charging/discharging rates. However, single crystals are expensive, difficult to grow and they are difficult to be integrated into an all-solid-state battery configuration. Thus, polycrystalline solid electrolytes are a more appropriate and realistic option. Ionic transport in polycrystalline materials is significantly different due to the presence of grain boundaries (GB) and an increase in surface to volume ratio. Thus, ionic transport mechanisms are more complex in nanocrystalline samples due to the surface charge regions.

In solid electrolytes, ionic transport generally depends on the structural framework, the intrinsic mobility of conducting ions and their thermal activation, the concentration of intrinsic and/or extrinsic defects, and further on the crystal field impact of the mobile ions. Ion diffusion mechanisms are mostly based on Schottky and anti-Frenkel point defects, comprising the vacancy mechanism, interstitial mechanism, and interstitial–substitutional exchange mechanism.[23] However, some materials with fluorite or tysonite type structure can achieve high ionic conductivities without a high defect concentration.[24, 25] Geometric frustration from size mismatch of the cation lattice was recently also discussed to play an important role for the conductivity of multinary fluorides with fluorite type structure.[26] In general, only a few stable fluorides exhibit significant ionic conductivity, while being insulators for the transport of electrons due to a wide bandgap.

Different fluoride conducting solid-electrolytes were reported in the literature. These solid electrolytes can be broadly categorized into two classes of compounds: tysonite-type ($LaF_3$ prototype) and fluorite-type ($CaF_2$ prototype). A considerable number of possibilities to achieve improved solid-state electrolyte/separator approaches for FIBs have been developed and will be addressed in this chapter. Different materials are discussed and grouped according to their structure type (e. g., rare-earth fluorides (tysonite-type structure) doped with alkaline-earth or alkaline-earth fluorides (fluorite-type structure) doped with rare-earth fluorides). This discussion also comprises further design aspects, such as the creation of surface defects by vapor pressure treatment ($CaF_2$-Hum), grain boundary activation using Lewis acids ($BF_3$), or critical geometry frustrations due to crystal deformations by multiple-phase systems.

## 4.1 Design of all-solid-state cells used for FIBs

FIBs have often been made in an all-solid-state modification. For all-solid-state FIBs, the most popular strategy is to make bulk pellets by cold (uniaxial) pressing of the powder precursors (cathode/electrolyte/anode). For this approach, it is important to note that most of the used active electrode materials for FIBs suffer from low electronic and ionic conductivity. For the powder-based electrodes, a suitable electron conduction pathway needs to be provided, which is commonly achieved by additives such as carbon black, graphite, nanotubes, metal surplus, etc.[24,

[27] The ionic conductivity is increased by the introduction of electrolyte materials. In most studies, the FIB active electrode materials are mixed with the electrolyte material and carbon black or nanotubes to form composite electrode materials.[8, 24, 27-29] Ball milling is by far the most used technique to prepare the composite electrodes and solid-state electrolytes. For the assembly of all-solid-state battery cells, Swagelok-type electrochemical cells are very common.[8, 24, 30] Figure 3 represents a typical Swagelok-type cell. Due to the low ionic conductivity of the most solid-state electrolytes for FIBs, the electrochemical cell setup should be heated most frequently up to 150 – 200 °C, and the cell-design helps to protect the Teflon-based sealings from plastic deformation or heat-induced degradation. Recently thin-film strategies have also been introduced to make FIB cells. For instance, Zhang et al. reported[31] on implementing a thin-film of Ba doped $LaF_3$ electrolyte by spin coating technique on a $CaF_2$ or $MgF_2$ anode composite as a substrate. Further, coin cell based systems were proposed by Grenier et al., where a high temperature stable epoxy resin can be used for sealing, facilitating improved longer-term operability.[32]

There also exist some reports[33, 34] on FIBs, which are based on liquid electrolytes and can then be investigated in the most common Swagelok-type setup. For instance, Davis et al. reported[34] on standard three electrode systems for FIBs based on a liquid electrolyte. In this study, copper nanoparticles or Cu@$LaF_3$ core-shell nanoparticles were made into a paste with polyvinylidene fluoride (PVDF) to prepare the working electrode platinum, and silver wires were used as the counter electrode and reference electrode, respectively. Moreover, bismuth, lead, cerium and calcium thin strip foils were used as the working electrode.

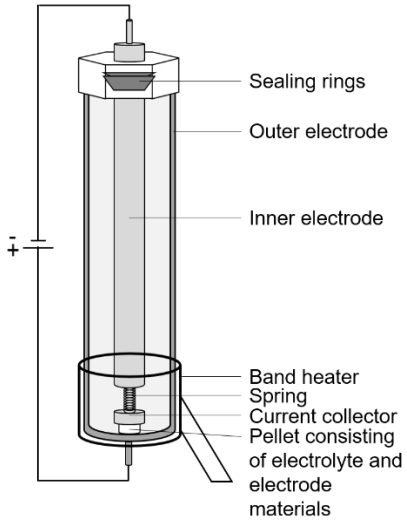


*Figure 3. A schematic of a high-temperature cell used for the electrochemical measurements conducted on all-solid-state FIBs.The figure has been reproduced from ref.[35].*

## 4.2 Ionic conductivity of rare-earth fluorides with tysonite-type structure

Tysonite-type $RE_{1-x}M_xF_{3-x}$ (RE = La, Ce, Sm, and M = Ba, Ca, Sr) fluorides are promising as SEs for FIBs as they show high ionic conductivities and large electrochemical stability window.[8, 36] In an undoped state, rare-earth fluorides show insufficient conductivities even for lab-scale operation. To improve the ionic conductivity in solid-state electrolytes defects are introduced into the crystal structure by increasing the concentration of mobile ionic species via aliovalent doping. It was shown that the doping of $LaF_3$ by $BaF_2$ enables the creation of fluoride vacancies.[37] These

$F^-$ vacancies promote a higher ionic mobility within the fluoride sublattice, leading to an increase of the fluoride conductivity by two orders of magnitude as compared to the stoichiometric compound.[38] Thus, the conduction mechanism in tysonite-type structures relies on a purely vacancy-type mechanism due to Schottky defects.[23, 39, 40] Reddy and Fichtner used Ba-doped $La_{1-x}Ba_xF_{3-x}$ ($0 \leq x \leq 0.15$) (LBF) as the SEs in FIBs in their initial studies (Figure 4a). They found a maximum conductivity for $La_{0.9}Ba_{0.1}F_{2.9}$. Further, LBF prepared by high energy ball milling method can be improved via sintering at high temperature.[8, 40, 41] The ionic conductivities of compacted, unsintered $La_{0.90}Ba_{0.10}F_{2.90}$ ($1.6 \times 10^{-4}$ S·cm$^{-1}$ at 160 °C) can be significantly improved by a further sintering step at 800 °C for 2 h to $10^{-5}$ S·cm$^{-1}$ at room temperature (Figure 4b). This observation within tysonite-type LBF fluoride ion conductors is explained by the differences in the grain boundary structure, which can result in a partial blocking of the migration pathways, and has been observed for various anion conducting compounds.[42] Thus, sintering treatments are viable methods to increase the ionic conductivity at the cost of the ease of cell fabrication. It is also worth acknowledging that the grain boundary influence can be compensated without increasing the grain size: In the case of a co-precipitated electrolyte, a slight increase of conductivity was attributed to reduced amounts of impurities during the synthesis process as compared to mechanical milling.[43]

In 2017, Chable et al. investigated the ionic conductivity of $La_{1-x}Ba_xF_{3-x}$ (LBF) synthesized by various methods, among them high-temperature solid-state reactions under inert atmosphere. [44] It was found (see Figure 4c) that the ionic conductivity at room temperature for the Ba-doped samples (≈ $6 \times 10^{-5}$ vs.$10^{-4}$ S·cm$^{-1}$ at RT for $La_{0.93}Ba_{0.07}F_{2.93}$) approaches the limit of the single crystalline state of pure $LaF_3$.[45] The observed conductivity was two orders of magnitude higher than observed earlier on cold-pressed pellets, with activation energies between 0.2 and 0.4 eV.[44] Still, compositional dependence is maintained, with the maximum conductivity at room temperature for a composition close to x=0.05 – 0.07 (see Figure 4d).[44] In addition, the compacted $La_{0.95}Ba_{0.05}F_{2.95}$ samples were tested and compared to powders that underwent the process at 900 °C with different combinations of cold uniaxial pressing and cold uniaxial plus isostatic pressing. From these experiments, the authors conclude that rare earth fluorides should be treated by a sintering process before or after the ball-milling to improve the ionic conductivity.

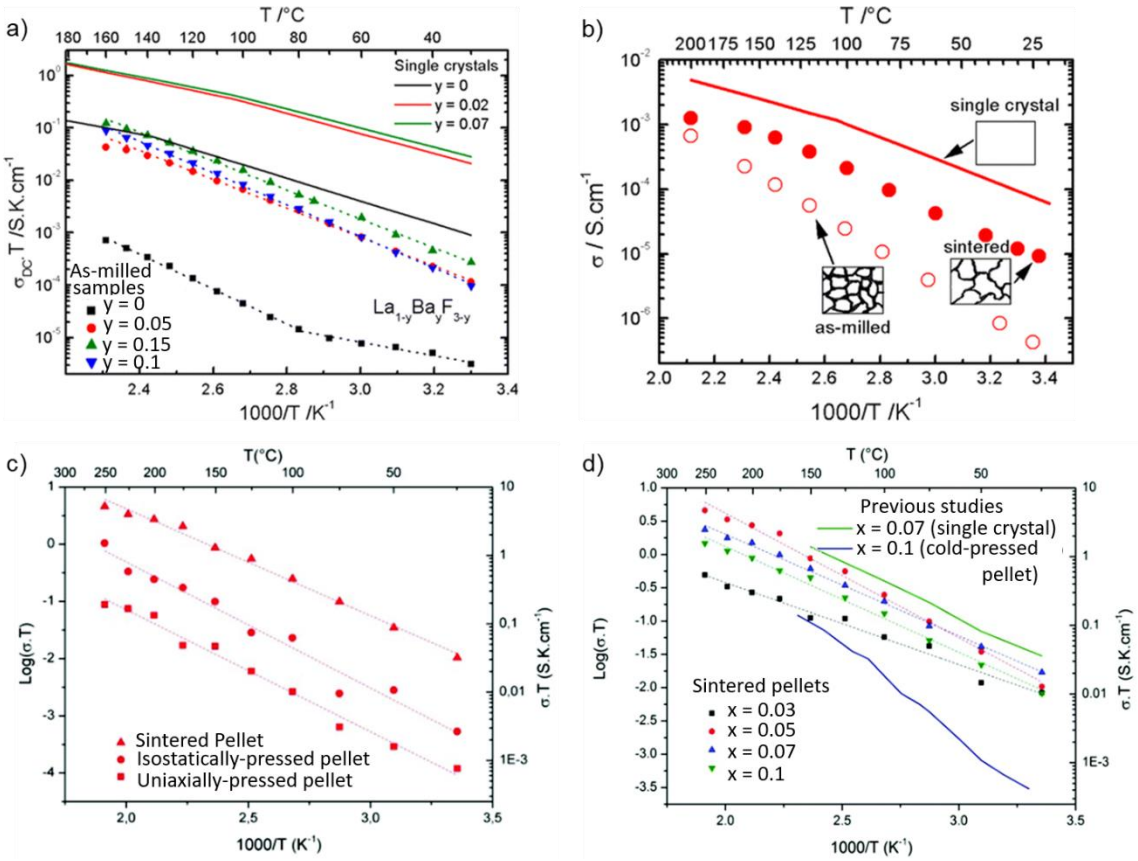


*Figure 4. (a) and (b) Arrhenius plots of the ionic conductivities of $La_{1-x}Ba_xF_{3-x}$. Parts (a) and (b) are reproduced with some modifications from ref.[37] with permission[ii]. (c) and (d) $La_{1-x}Ba_xF_{3-x}$ (x= 0.03,0.05, 0.07, 0.1) samples after cold-uniaxial pressing, cold isostatic pressing, and sintering of the pellets. Parts (c) and (d) are reproduced with some modifications from ref.[46] (an original RSC publication). In part (d) the blue and green lines from the single crystal of $La_{1-x}Ba_xF_{3-x}$ (x= 0.07, 0.1). Different pressing method applied for the $La_{0.95}Ba_{0.05}F_{2.95}$ sample for the ionic conductivity for cold-uniaxial pressed pellet, a cold-uniaxial, cold-isostatic pressed pellet and a sintered pellet are reported.*

Zhang et al.[47] investigated the ionic conductivity of $La_{1-x}Ba_xF_{3-x}$ ($0 \le x \le 0.15$) thin-films synthesized by a sol-gel assisted spin coating method based on mixtures of metal trifluoroacetate salts. They observed that the conductivity of the thin films could be significantly improved by increasing the sintering temperature and time. The conductivity value of the film was $1.6 \times 10^{-4}$ S·cm$^{-1}$, a significant improvement in comparison to porous films [36, 47], and an optimized thermal treatment condition was determined to be at 450 °C for 4h. When compared to the bulk-type electrolyte, the overall conductance of the film was improved by a factor of ~ 65. The thin film morphology is of special importance, since the overall resistance was significantly reduced due to the low thickness of the thin films. A comparison shows that the conductance of a bulk type electrolyte at 170 °C is similar to that of a thin-film electrolyte at 80 °C, which could help to build all-solid-state fluoride ion batteries working at more viable conditions.[36]

Not only lanthanum-based fluorides can be used as a solid electrolyte. Dieudonné et al. investigated the ionic conductivity of $SrF_2$ doped $CeF_3$ ($Ce_{1-x}Sr_xF_{3-x}$), synthesized by solid-state reaction at 900 °C for 24h.[48] A high ionic conductivity of $3\times10^{-4}$ S·cm$^{-1}$ was obtained for $Ce_{0.975}Sr_{0.025}F_{2.975}$ at RT, which is close to the conductivity of a corresponding single crystal and

[ii] Copyright (2014) American Chemical Society

better than previously reported fluoride compounds.[48] At room temperature, the ionic conductivity observed in various fluorides adopting the fluorite-type structure reached a maximum value at x = 0.025 with one of the lowest activation energies of 0.31 eV. The $Sr^{2+}$ substitution for $Ce^{3+}$ ions in this network associated with the creation of anionic vacancies modifies the fluoride ion mobility drastically. A maximum $F^-$ conductivity for x = 0.025 corresponds to the largest difference in bond distances between the F2 (4*d* site) and F3 (2*a* site) ion to the surrounding Sr/Ce ion and the highest buckling of the $RE_{1-x}AE_xF_{3-x}$ layers, which appears to result in low activation energy in addition (Figure 5a). They further concluded that in tysonite-type $RE_{1-x}AE_xF_{3-x}$ (RE = rare-earth and AE = alkaline-earth) the difference in the ionic sizes of the host element (RE) and the dopant (AE) plays a vital role for achieving high ionic conductivity: When the ionic sizes are comparable, the conductivity reaches to the maximum at a low substitution rate due to network relaxation of the $RE_{1-x}AE_xF_{3-x}$ slabs in competition with the chemical pressure, which leads to a strong variation of sheet thickness.

Further detailed investigations have been carried out on tysonite-type Ca-doped $SmF_3$, $Sm_{1-x}Ca_xF_{3-x}$ ($0.05 \leq x \leq 0.17$), again by Dieudonné *et al*.[49] The SEs were prepared using solid-state synthesis followed by sintering at 1000 °C. Analysis of the XRD data showed a reduction in the unit cell volume with an increasing amount of Ca dopant. This volume reduction of the cell has been attributed to the creation of anionic vacancies that decrease cationic coordination, and could further be explained by increased cation repulsion due to the loss of shielding. The best ionic conductivity as high as $1.0\times10^{-4}$ S $cm^{-1}$ was obtained for $Sm_{0.95}Ca_{0.05}F_{2.95}$ at RT. In $Sm_{1-x}Ca_xF_{3-x}$, the difference (+0.05 Å) of ionic radii for nine-fold coordination between $Ca^{2+}$ (1.18 Å) and $Sm^{3+}$ (1.13 Å) leads to a predominant influence of the network relaxation with a decrease of cell volume related to segregation of anionic vacancies. Both the thickness of $[Sm_{1-x}Ca_xF_{3-x}]$ layers (≈ 1.20 Å) and the ionic conductivity are maximal for a composition of x = 0.05. This observation was explained by a modification of the fluorine environments and segregation of the vacancies around the calcium by increasing the x values. In contrast, for $La_{1-x}Ba_xF_{3-x}$, the large difference of cationic radii (+0.25 Å) introduces a significant chemical pressure and microstrain together with a significant increase in the cell volume. Comparison with $La_{1-x}Ba_xF_{3-x}$, $Ce_{1-x}Sr_xF_{3-x}$, and $La_{1-x}Sr_xF_{3-x,}$ shows that the higher the buckling effect of $RE_{1-x}AE_xF_{2-x}$, which affects the distortion of the F1 site, the higher the ionic conductivity. This explains the evolution with x of the RT ionic conductivity of different solid electrolytes (Figure 5b), which hardly correlates with simple volume changes only. They suggested that a moderate ionic radii difference serves to optimize the ionic conductivity: Y-Ca, Eu-Ca and Gd-Ca could fulfill this requirement. However, there are no experimental results on the suggested systems so far. Most recently, $Sm_{1-x}Ca_xF_{3-x}$ solid electrolytes were prepared by high-energy planetary ball-milling as an alternative method and studied with NMR by Molaiyan et al.[50], which helped to correlate the ionic conductivity to the detailed structural arrangements and relaxations taking place within this compound.

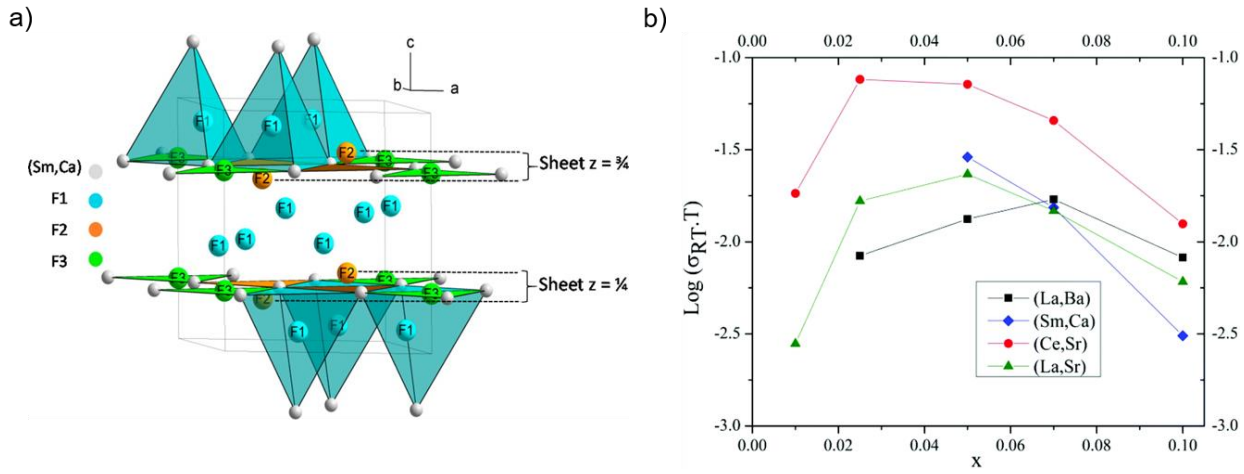


*Figure 5. (a) The crystal structure representation of the tysonite-type structure. (b) Impedance plot and complex fits of the $Sm_{0.95}Ca_{0.05}F_{2.95}$ at room temperature. (a, b: Reproduced from ref. [49] with permission[iii]) (c) Variation of the ionic conductivity vs temperature for $Ce_{1-x}Sr_xF_{3-x}$ (x = 0, 0.01, 0.025, 0.05, 0.07, 0.10). (d) Evolution with x of the room temperature ionic conductivity of $RE_{1-x}AE_xF_{3-x}$ (RE= La, Ce, Sm; AE= Ba, Sr, Ca). (c, d: Reproduced from ref.[48] (an original RSC publication)).*

## 4.3 Alkaline-Earth Fluorides with Fluorite-type Structure

### 4.3.1 $AE_{1-x}RE_xF_{2+x}$ Compounds

Solid-state fluorite-type electrolyte systems are found at the alkaline earth richer end of the series with a general chemical formula of $AE_{1-x}M_xF_{2+x}$ (AE = Ca, Sr, Ba; M = RE), and also for a binary mixture between two alkaline earth fluorides. Most of these fluoride-conducting electrolytes have been synthesized by a high energy ball-milling method, e. g., for the formation of the series $Ba_xCa_{1-x}F_2$.[39, 51, 52] An ionic conductivity of 1.16 $\times 10^{-5}$ $S \cdot cm^{-1}$ for $Ba_xCa_{1-x}F_2$ at 413 K was reported,[52] which is lower than for the tysonite type systems. Apart from isovalent doping, also aliovalent series of $BaF_2$ doped with $LaF_3$ were taken into consideration.[42, 53] $Ba_{0.6}La_{0.4}F_{2.4}$ shows the highest conductivity among the $Ba_{1-x}La_xF_{2+x}$ solid solutions (Figure 6a). Ball-milling of coarse-grained $BaF_2$ yields a nano-crystalline sample, which shows a conductivity of almost two orders of magnitudes higher as compared to non-milled material. The ionic conductivity can be further improved by further addition of calcium [54], by which a non-equilibrium phase is obtained. In contrast, the increase of conductivity was explained here from the increase of disorder and strain introduced when the cations are of different sizes.[55, 56]

Düvel et al. [57] reported a detailed NMR study of $Ba_{1-x}La_xF_{2+x}$ ($0 \le x \le 1$) compositions synthesized by a ball milling method at ambient temperature. The $Ba_{1-x}La_xF_{2+x}$ compounds crystallized in the fluorite-type structure from $0 \le x \lesssim 0.775$, with phase mixtures beyond this range and tysonite-type structures for $x > 0.85$. From $x \approx 0.70$ to $x \approx 0.85$, the NMR spectra indicate structural aspects of both crystal structures, though there is still a decrease of the chemical shift of the fluoride ions on the F2/3 sites with increasing $BaF_2$ content (Figure 6b). The authors showed that changes of chemical shifts associated with the structural transition can be correlated with the transitions in the bond distances *d*(M–F). Further, there seems to be an intrinsic change of bonding to the F1

[iii] Copyright © 2015, American Chemical Society

ion in the range from $x = 0.55$ to $x = 1$ making the fluoride site in the fluorite-type structure more similar to the F1 ion in the tysonite-type structure (Figure 6b).

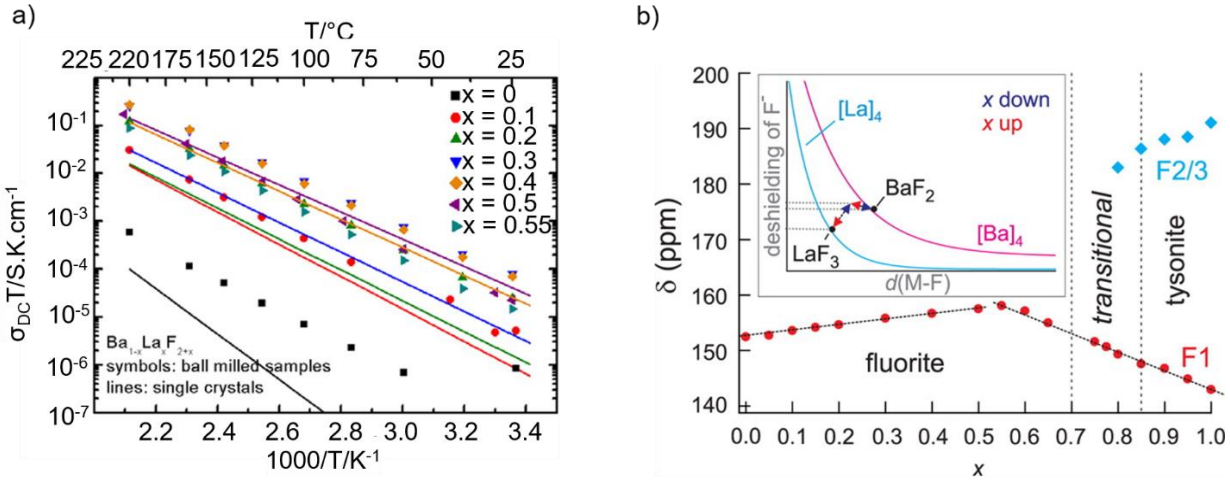


*Figure 6. (a) Ionic conductivity for $Ba_{1-x}La_xF_{2+x}$ ($0 \le x \le 0.55$) solid solutions in comparison with ball-milled and single crystals of $Ba_{1-x}La_xF_{2+x}$.The best performance of ionic conductivity was reported for the sample x = 0.40. (Reproduced with some modifications from ref.[58] with permission[iv]). (b) $^{19}F$ Nuclear Magnetic Resonance (NMR) studies reported for the chemical shift changes of $Ba_{1-x}La_xF_{2+x}$ with x. The red points indicate that the fluoride ions on the anion site in the fluorite-type structure and F1 sites in the tysonite structure appear to show a transition between each other. The NMR lines of $Ba_{1-x}La_xF_{2+x}$ ($x \ge 0.80$) corresponding to F1 on F2 and F3 sites with the tysonite-type structure as blue rhombs. (Reproduced from ref.[57] with permission[v]).*

### 4.3.2 Tetragonal $BaSnF_4$ and Interlayer Electrolytes ($La_{0.9}Ba_{0.1}F_{2.9}/BaSnF_4$)

$SnF_2$ containing compounds like $MSnF_4$ (M = Pb, Ba, Ca, Sr) can show ordering between the M and the Sn site cations in an otherwise fluorite-type structural setting. Such ordering can lead to a high conductivity even at room temperature.[59-61] The high ionic conductivity in $SnF_2$ containing compounds results from the presence of the $5s^2$ lone pair on the $Sn^{2+}$ atom, which requires space (the lone pair is known to require as much space as a fluoride ion itself[62, 63]). This strongly distorts the fluoride sublattice in combination with the ordering of cations. The crystal structure of tetragonal $BaSnF_4$ (Figure 7a) can be derived from the cubic fluorite-type structure by ordering of the Sn and Ba cations in Sn-Sn, Ba-Sn, and Ba-Ba layers, along the *c*-direction of the tetragonal cell. This ordering results in three different fluoride sites, termed as F1 ($^3/_4$, $^1/_4$, 0.19), F2 ($^3/_4$, $^1/_4$, $^1/_2$), and F3 ($^1/_4$, $^1/_4$, 0.68), and they reside in Sn-Sn, Ba-Sn, and Ba-Ba layers, respectively. The stereoactive lone pair induces a repulsive interaction between the lone pair electron and negatively charged fluoride ion, which leads to a depletion of the fluoride ions in the Sn−Sn and Sn−Ba layers of the $BaSnF_4$ crystal structure. Hence, the fluoride ions between Sn-Sn and Sn-Ba layers become mobile since the lone pair is polarizable and can reorient on movement, thus becoming involved in the conduction process. The ionic conductivity of $BaSnF_4$ is in the order of $1 \times 10^{-4}$ $S \cdot cm^{-1}$ at RT.[64] Interestingly, its cold-pressed powders also exhibit high conductivity at RT, which makes it suitable candidates as solid electrolytes for fluoride ion batteries. Recently,

[iv] Copyright © 2013 American Chemical Society
[v] Copyright © 2014 American Chemical Society

Mohammad et al. have demonstrated rechargeable RT-FIBs utilizing $BaSnF_4$ as a solid electrolyte [65], where the electrode materials were chosen to take into account the limited electrochemical stability of the electrolyte. The ionic conductivity of $3.5 \times 10^{-4}$ S·cm$^{-1}$ at RT for the electrolyte (see Figure 7b) can be sufficient for RT fluoride-ion battery applications. The cells were based on $BaSnF_4$ as the electrolyte, $BiF_3$ as the cathode, and Zn or Sn as the anode. The electrochemical results on Zn/$BaSnF_4$/$BiF_3$ cell are displayed in Figure 7c,d. The cyclic voltammetry profile of the cell features a cathodic and anodic peak confirming the reduction of $BiF_3$ and oxidation of Bi, respectively (Figure 7c). The cell exhibits a first discharge and charge capacity of 56 and 43 mAh·g$^{-1}$, respectively (Figure 7d). At subsequent discharging and charging, the capacity is found to increase slightly, which can be explained by increased electrochemical accessibility of the Zn anode.

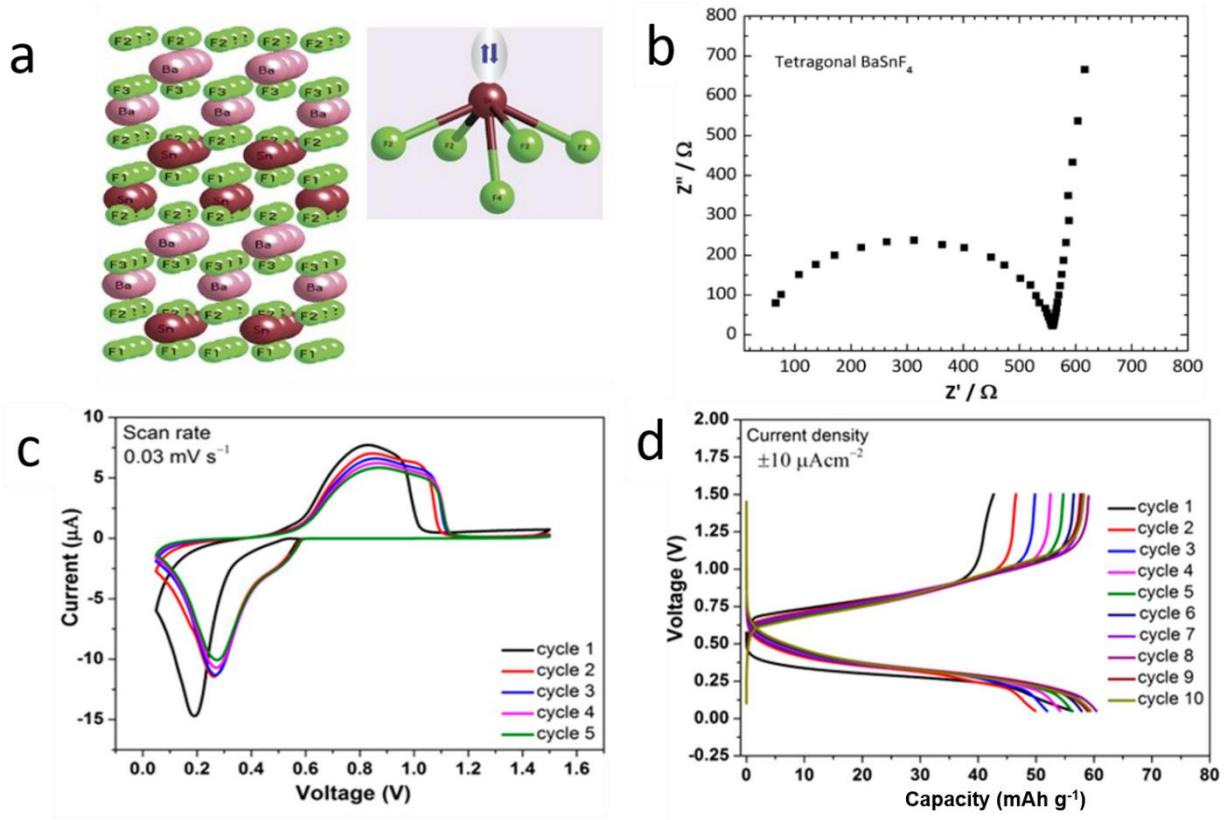


*Figure 7. (a) Layered structure of tetragonal $BaSnF_4$ displaying different cation layers and fluoride ions with Sn coordination environment of $BaSnF_4$ showing lone pairs on $Sn^{2+}$ pointing in the c-direction (figure a is reproduced from ref.[59] with permission[vi]; (b) Nyquist plot of tetragonal $BaSnF_4$ obtained at 25 °C (reproduced from[66]), (c) Cyclic voltammogram profiles of Zn/$BaSnF_4$/$BiF_3$ cells obtained at 25 °C; (d) Voltage-composition profiles of Zn/$BaSnF_4$/$BiF_3$ cells obtained at 25 °C (reproduced with some modifications from ref. with permission [vii]).*

Currently, the low electrochemical stability of $BaSnF_4$ limits the use of highly reductive anode materials or highly oxidizing cathode materials, because $Sn^{2+}$ can both be oxidized or reduced at intermediate potentials already. To build high potential FIBs, high electropositive metals (Ce, Mg, La) should be used as anodes, which are compatible with electrolytes like tysonite-type $La_{0.9}Ba_{0.1}F_{2.9}$. $La_{0.9}Ba_{0.1}F_{2.9}$ electrolytes with low RT conductivity ($4 \times 10^{-7}$ S cm$^{-1}$). To overcome

[vi] Copyright © 2002 American Chemical Society
[vii] Copyright © 2018, American Chemical Society

these limitations of the low electrolyte stability and low ionic conductivity, Mohammad et al. developed an interlayer electrolyte concept to build high-potential RT-FIBs.[67] This approach is developed by combining synergies of $BaSnF_4$ and $La_{0.9}Ba_{0.1}F_{2.9}$ electrolytes. A thin layer of $La_{0.9}Ba_{0.1}F_{2.9}$ was pressed together with a thick layer of $BaSnF_4$. The use of low conductive $La_{0.9}Ba_{0.1}F_{2.9}$ succeeded in maintaining the high total conductivity of the electrolyte (compared to pure $La_{0.9}Ba_{0.1}F_{2.9}$), and in physically isolating the less stable and highly conductive electrolyte ($BaSnF_4$) from the electropositive anode. In fact, such a modification is due to the fact that $BaSnF_4$ offers a narrow potential stability. Therefore, to increase the potential window two thin layers of conductive $La_{0.9}Ba_{0.1}F_{2.9}$ could be attached to the $BaSnF_4$ layer. However, $La_{0.9}Ba_{0.1}F_{2.9}$ has a much lower conductivity at room temperature than $BaSnF_4$. Figure 8a shows the cross-sectional SEM image obtained for an inter-layer electrolyte pellet ($La_{0.9}B_{0.1}F_{2.9}$ (90 µm)/$BaSnF_4$ (650 µm)), which highlights that both layers stick uniformly to each other without intermixing. Impedance analyses are used to investigate the conductivity and interface stability of the interlayer electrolyte as shown in Figure 8b and c. The figure compares the Nyquist plots of interlayer electrolyte with different relative thicknesses of $La_{0.9}Ba_{0.1}F_{2.9}$ obtained at 25 °C, and show a strong difference on to which extent grain, grain boundary and electrode responses are expressed, though the resistance appears to scale linearly with the thicknesses of the different layers. In the mentioned report, only the $La_{0.9}B_{0.1}F_{2.9}$ (90 µm)/$BaSnF_4$ (650 µm) electrolyte was utilized for electrochemical tests. The other electrolyte with thinner $La_{0.9}B_{0.1}F_{2.9}$ (<45 µm) layer has provided higher conductivity, however it was not employed for the electrochemical tests due to the possibility of physical contact between the anode (Ce composite) and $BaSnF_4$ electrolyte (through the penetration of the thin LBF layer). The thickness of interlayer electrolytes was optimized to $La_{0.9}B_{0.1}F_{2.9}$ (<45 µm)/ $BaSnF_4$ (<650 µm), further optimization was not possible due to mechanical stability and sample preparation technique reason (manual powder spreading and pressing). The authors conclude that with improved coating methods, it might be possible to achieve high ionic conductivities similar to that of $BaSnF_4$ while extending its electrochemical stability window. Electrochemical performance testing of the interlayer electrolyte was conducted using $BiF_3$ as a cathode and Ce as an anode. The charge-discharge profiles of the interlayer electrolyte-based cell is displayed in Figure 8d. The cell shows an open circuit voltage of 2.6 V at room temperature. It delivered a first discharge capacity of 27 $mA{\cdot}h{\cdot}g^{-1}$ at an average voltage of 1.4 V. During the second and subsequent cycles, the discharge and charge profiles show high average voltage plateau. In the following cycling, quick capacity fading was observed, resulting in 3 $mA{\cdot}h{\cdot}g^{-1}$ after five cycles Figure 8d).

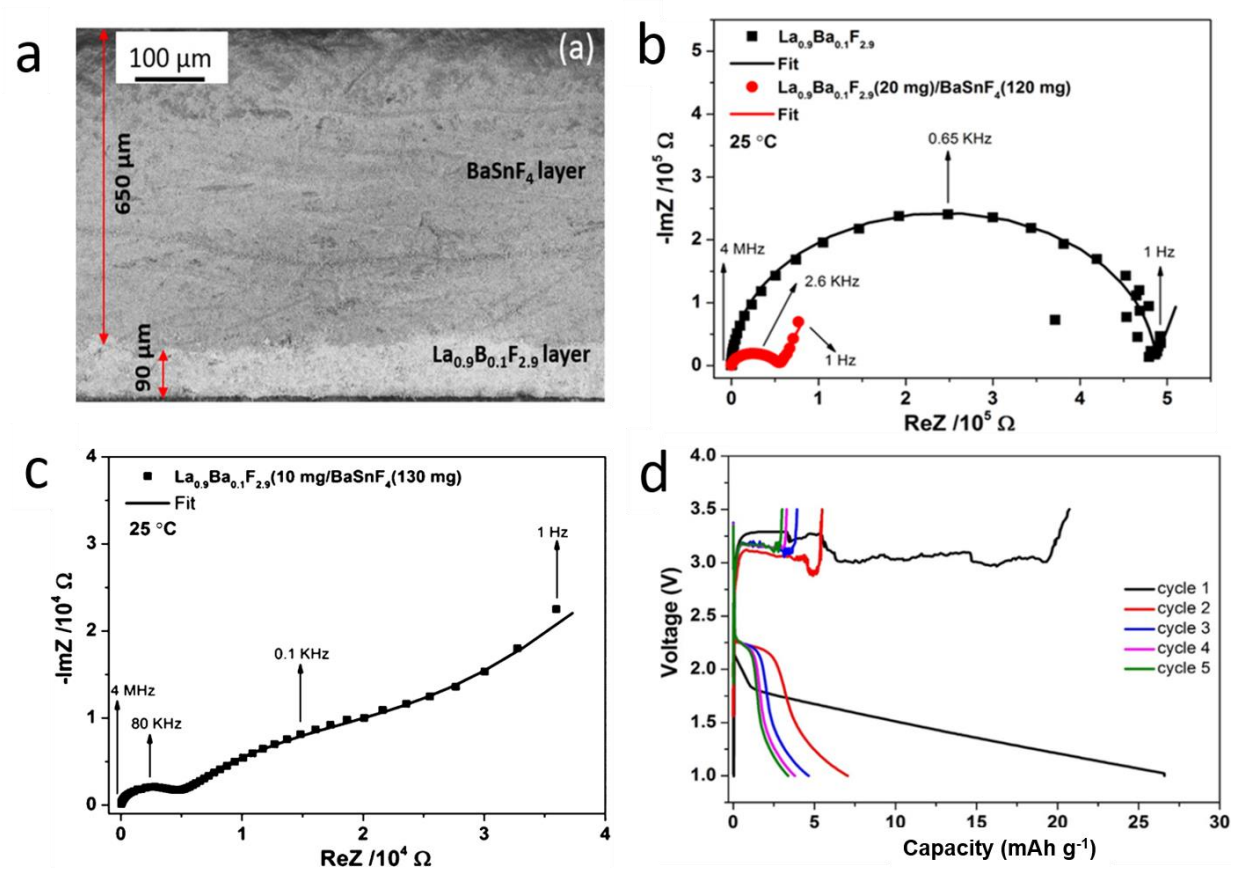


Figure 8. *(a) Cross-sectional SEM image of $La_{0.9}Ba_{0.1}F_{2.9}$ (20 mg)/$BaSnF_4$ (120 mg) pellet, (b) Nyquist plots (symbols) and the corresponding fit (lines) of $La_{0.9}Ba_{0.1}F_{2.9}$ (20 mg)/$BaSnF_4$ (120 mg) and $La_{0.9}Ba_{0.1}F_{2.9}$ obtained at 25 °C, (c) Nyquist plots (symbols) and corresponding fit (line) for $La_{0.9}Ba_{0.1}F_{2.9}$ (10 mg)/$BaSnF_4$ (130 mg) electrolyte obtained at 25 ℃, (d). Voltage-composition profiles of Ce/$La_{0.9}Ba_{0.1}F_{2.9}$/$BaSnF_4$/$BiF_3$ cell obtained at 25 °C with a current density of ±10 µA·cm$^{-2}$ (reproduced with some modifications from ref.[67] with permission[viii]).*

### 4.4 Nano-crystalline Fluorite-type $Ba_{1-x}Sb_xF_{2+x}$ ($0 \le x \le 0.4$)

Besides $Sn^{2+}$, there are other cations containing lone pairs of electrons such as $Sb^{3+}$, $Bi^{3+}$, and $Tl^{+}$, which might have a similar effect on the ionic conductivity. In an attempt to mimic the idea of the lone pair effect for the ionic conductivity enhancement, Mohammad et al. have recently synthesized $SbF_3$-doped $BaF_2$ via ball-milling, assuming that $ns^2$ configured $Sb^{3+}$ might strongly participate to an increase of the ionic conductivity of $BaF_2$.[68] The doping of $SbF_3$ in the $BaF_2$ crystal was limited to $x < 0.5$, confirmed by an XRD analysis (displayed in Figure 9a). This means a comparably lower amount of $SbF_3$ is sufficient in order to obtain a higher occupancy of the interstitial site. In the crystal structure of $Ba_{1-x}Sb_xF_{2+x}$ ($0 \le x \le 0.4$), Ba and Sb (represented in grey) form an *fcc* array in which fluoride ions (represented in blue) occupy all tetrahedral sites (Figure 9b). During doping, extra fluoride ions due to the higher valancy of the dopant $Sb^{3+}$ occupy the interstitial positions such as F2 and F3. The interstitial site F1 ($^1/_2$, $^1/_2$, $^1/_2$) is being occupied at a lower concentration of the dopant, whereas the related sites with off-centre shifts, F2 ($^1/_2$, 0.37, 0.37) and F3 ($^1/_2$, 0.41, 0.41), are occupied at higher concentrations of the dopant. The ion conductivity of the solid solution was increased with increasing dopant concentration, indicating

[viii] Copyright © 2019, American Chemical Society

that these off-centre shifts can be considered crucial for obtaining functional ceramics. Further, the temperature dependent evolution of the ionic conductivity of $Ba_{1-x}Sb_xF_{2+x}$ ($0 \le x \le 0.4$) was investigated (Figure 9c). By this, it was found that it can reach twice the conductivity of the isostructural $Ba_{0.7}La_{0.3}F_{2.3}$ ($1.55 \times 10^{-4}$ S·cm$^{-1}$ at 160 °C), meaning that the additional increment of conductivity might result most plausibly from the stereochemical impact of the ns$^2$ cation. The material can also be used within a full battery against Ce anodes. Figure 9d shows the electrochemical profiles of the cell for the first five cycles, showing high electrochemical accessibility of the active electrode material of ~ 66% of the theoretical specific capacity of $SbF_3$ (450 mAh·g$^{-1}$). However, rapid capacity fading was observed for prolonged cycling. This considerable capacity fading is probably due to large volume and structural changes in the electrode materials and not necessarily linked to the electrolyte itself.

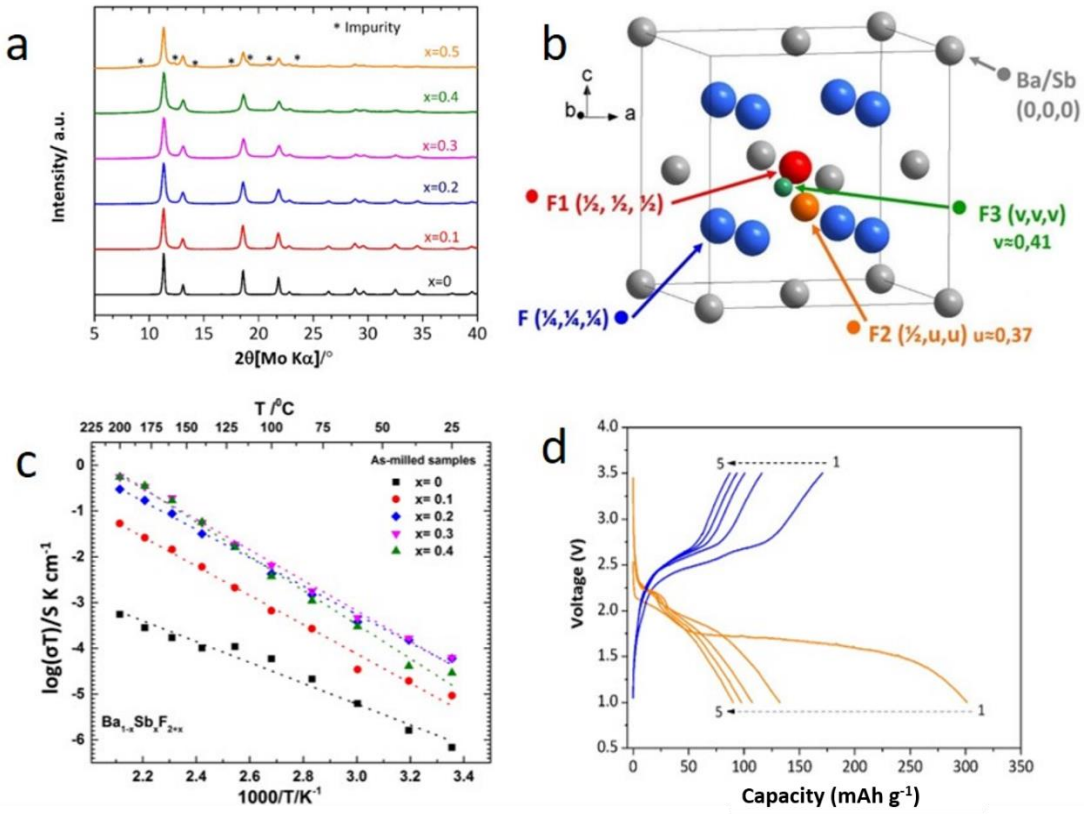


**Figure 9** (a) *XRD patterns of $Ba_{1-x}Sb_xF_{2+x}$ ($0 \le x \le 0.5$) compounds, (b)Representative structural view of $Ba_{1-x}Sb_xF_{2+x}$ (doped fluorite), (c) Arrhenius plots of the ionic conductivity of $Ba_{1-x}Sb_xF_{2+x}$ ($0 \le x \le 0.4$) compounds (symbols) and their fits (dotted lines). (d) Voltage-capacity profiles of $Ba_{0.7}Sb_{0.3}F_{2.3}$/$La_{0.9}Ba_{0.1}F_{2.9}$/Ce cell obtained at 150 °C with a current density of 10 μA·cm$^{-2}$ (figures are reproduced with some modifications from ref.[68] with permission [ix]).*

## 4.5 $PbSnF_4$ based Solid Fluoride Electrolytes

In-depth investigations and improvements of the ionic conductivities of solid-state electrolytes are emerging areas of FIBs. So far, $Pb_xSn_{2-x}F_4$ (Figure 10a) is one the best superionic fluoride conductors.[69] $^{19}$F MAS NMR results show the that mechanochemical synthesis drives the system mainly into the cubic *β*-phase, with the introduction of surface defects, which exchange with the

[ix] Copyright © 2018, American Chemical Society

nanoparticle core.[69, 70] This interaction also promotes conductivities within the crystallite and at the particle boundaries, with ion mobility at the macroscopic material level, which is in slight contrast to what is reported in previous studies.[71-73] Low activation energies result in high ionic conductivities at room temperature (Figure 10b), with values close to single crystals and better than what was found previously for fluorite type materials.[74, 75] The solid electrolytes of $Pb_xSn_{2-x}F_4$ were also prepared by high-energy planetary ball-milling.[76] Such electrolytes showed a fluoride ion conductivity equal to that of the electrolytes synthesized using a melting method with an activation energy of 0.30 eV for x = 1.1.

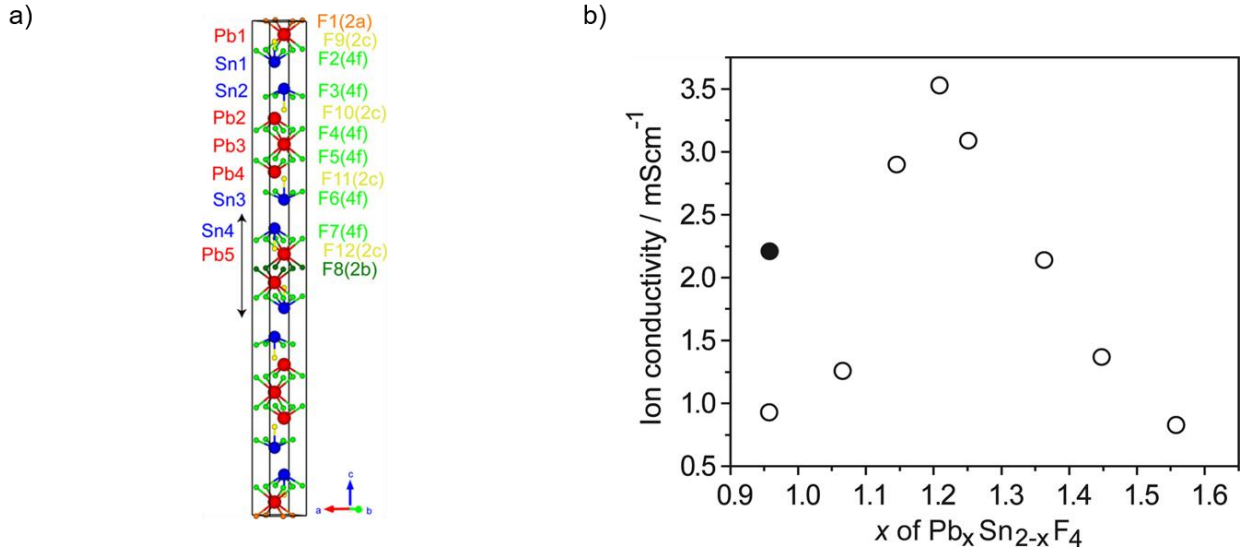


*Figure 10. (a) Packing of β+-$PbSnF_4$ in the unit cell. Blue and red balls are Sn and Pb, respectively. (b) Dependence of the conductivity at room temperature on the Pb/Sn molar ratio in the $Pb_xSn_{2-x}F_4$ pressed-powder samples (x = 0.96–1.56) annealed at 400 °C (open circle) and 200 °C (filled circle) (figures are reproduced from ref.[77] with permission[x]).*

## 4.6 $CaF_2$ based Solid Electrolytes for FIBs

$CaF_2$ would be a cheap electrolyte material with a high electrochemical stability; however, pure $CaF_2$ is a bad ionic conductor, due to the hard nature of the $Ca^{2+}$ ion.[78] Yuria Saito et al. reported that an ionic conductivity enhancement of $CaF_2$ could be achieved using Lewis acids [79], but not via the creation of grain conductivity on doping. The effect of the addition of a Lewis acid, e. g., $SbF_5$ or $BF_3$, on the fluoride ion conductivity in $CaF_2$ indicated a surface activation of the particles. The conductivity enhancement mechanism is based on the adsorption of Lewis acids, which attract fluoride ions out of the $CaF_2$ boundary regions to create vacancies at the $CaF_2/SbF_5$ or $CaF_2/BF_3$ interfaces, giving rise to a strong increase of the ionic conductivity. The conductivity results based on $CaF_2$ thin films also confirmed the presence of space-charge regions as a consequence of the attractive forces of the adsorbed Lewis acid.[79]

Molaiyan et al. have recently reported that the surface activation and conductivity enhancement of calcium fluoride synthesized via ball milling is possible.[80] The pure $CaF_2$ powder was exposed to salt water with a relative humidity (RH) of 88%, and ball-milled subsequently. The reported ionic conductivity of synthesized humidified $CaF_2$ electrolyte was around $1.9 \times 10^{-5}$ $S \cdot cm^{-1}$ at room

[x] Copyright © 2008 American Chemical Society

temperature. The reported values are several orders of magnitude higher than pure and ball-milled $CaF_2$ ($2 \times 10^{-7}$ to $1.6 \times 10^{-11}$ $S \cdot cm^{-1}$).[81] The reported activation energy of the humidified $CaF_2$ was around 0.35 eV, which was related to the surface formation of interstitial fluoride sites with suggested formation energies of around 0.25 eV,[82, 83] making the material applicable in fluoride ion batteries.[84] The ionic conductivity increases with higher temperature up to a certain critical temperature, after which the decomposition of the defect structure is promoted and the conductivity decreases. From this study, it can be concluded that crystal surface defects strongly influence overall bulk conductivities[85, 86] and can provide an alternative route as compared to bulk modifications.[87, 88]

## 4.7 Synthesis of Solid Electrolytes: Ball-Milling Method and other methods

Solid-state reactions generally occur at higher temperatures and often lead to powder morphologies that are unfavorable for battery cell fabrication. In favorable cases, reactions can be carried out merely by grinding the reagents via mechanochemical synthesis [89], and this method has been widely studied for the preparation of multinary fluorides.[42, 52, 57, 73, 90-93] On the lab-scale level, such synthesis will be done with a high-energy milling method. The crystalline reagents are being impacted with the milling balls at high kinetic energies, which causes high impact energies and can reduce the crystalline regions down to nanometer size with the introduction of crystal defects also.[42] Higher rotational speeds introduce a higher energy to the system leading to reduction in the crystallite size or even a destruction of the crystal structure and a creation of more defects including point defects and grain boundaries. Therefore, ball milling can be a method of choice when nanostructure/amorphous phases are desired. Furthermore, especially in the case of doping purposes, a higher energy results in a more homogenous distribution of the dopant. The optimal milling rotational speed highly depends on the type and the mechanism of ion transport within the solid electrolyte. For instance, nanocrystallization of $CaF_2$ and $Ba_{1-x}La_xF_{2+x}$ serves to make more defects and is in favor of obtaining higher conductivities due to migration of vacancies along the grain boundaries. The mechanism of conductivity in tysonite-type structures of $La_{1-x}Ba_xF_{3-x}$, however, is different from fluorite-type samples and the presence of grain boundaries may block the migration of vacancies through the sample.[94] In this case, increasing milling rotational speed is not in favor of increasing the conductivity, although, it results in a more homogenous distribution of the dopant which eventually significantly increases the ionic conductivity. In this respect, it is reported that sintering of nanoparticles of $La_{1-x}Ba_xF_{3-x}$ (as a sort of post-ball-milling treatment) can remarkably improve the ionic conductivity of the compound.[43] Thus, mechanochemical synthesis may become an essential method for the synthesis of new nanomaterials and nanocomposite materials, as it is relatively cheap and energy-efficient. In addition, further advantages of mechanochemical synthesis comprise a more reliable, easy operation to ensure reproducibility and large scale synthesis. As a disadvantage, one must acknowledge that due to high-speed rotation of the vial usually for few hours, contaminations might be introduced into the system. This can be even more severe for fluoride-based materials, which can be reactive towards many milling vials (e.g., silica or alumina based materials). Further, the magnitude of the contamination in a ball milling process depends on time of milling, intensity of milling, atmosphere in which the powder is milled, nature and size of the milling medium and differences in the hardness of the powder and the milling container.[95] Milling parameters such as time directly influence the energy provided with the milling process and it is not always possible to reduce the milling time or rotational speed. Therefore, to provide the required energy for the milling and simultaneously keep the contamination as low as possible, several strategies have been suggested such as minimizing the impurity within the starting materials, coat the inner walls of the milling container by alike powders, use grinding medium and container that is harder than the powder being milled, pursue the milling process under an inert gas such as Ar (for instance,

fill the milling container inside a high Ar purity glove box)[95] and finally introduce sufficient breaks in order to avoid local increase in temperature resulting in crystallite growth or occurrence of undesired reactions.[96]

As discussed in the previous section, post-ball-milling treatments such as high-temperature sintering can often be required to reach the highest ionic conductivities, where the increase of conductivity must be balanced against particle growth, which can be unfavorable for cell fabrication. The ionic conductivity is highly dependent on the microstructure of the polycrystalline material, as conduction properties are different within the grain boundaries and in bulk.[97] In polycrystalline solid electrolytes, especially when milled to the nanoscale, the conduction properties can be radically different from their single-crystalline counterparts. This is due to the fact that high amounts of grain boundaries must be surpassed and since such powders are often richer in defects.[98] From a microscopic viewpoint, properties are different for the bulk, which generally presents the same conduction properties as a single crystal, and for the surface, where many defects are present at the grain boundaries.[48] While the conduction is limited by the migration of the ionic species in the grain boundaries, if the powder processed by cold uniaxial pressing, the sintered samples are normally dominated by bulk conduction.[99]

Apart from ball-milling, only a few reports exist which emphasize on the preparation of nano-crystalline materials via other approaches. Since most electrolytes are based on alkaline earth or lanthanide metals, precipitation routes are feasible for the fabrication of nano-crystalline defect rich powders. This is based on the low solubility of these fluorides, even in an aqueous solution. Bhatia et al.[43] found that this fabrication method can give similar properties as the ball-milling procedure. Due to the similar low solubility of $LaF_3$ and $BaF_2$, this method can even be used for the preparation of mixed crystals of higher complexity, such as $La_{1-x}Ba_xF_{3-x}$. Further, up-scaling of powder production could also be considered easier for wet-chemical approaches in contrast to milling based reaction routes.

## 4.8 Temperature-dependence of Fluoride conducting Materials – A comparison

From the early days until now, the detailed understanding of structural and conductivity features of inorganic fluorides has opened the path for the development of many solid fluoride electrolytes with improved ionic conductivity and their use in lab-scale batteries in various electrochemical studies. In a nutshell, the doping of pure fluoride electrolytes with aliovalent fluorides (e.g., $BaF_2$-doped $LaF_3$, KF-doped β-$PbF_2$ or $BiF_3$-doped β-$PbF_2$) leads to an increase in the ionic conductivity of the doped material due to the creation of fluoride point defects most often. Defects present in the crystal structure provide fast diffusion pathways for fluoride ions and result in the conductivity enhancement required to obtain reasonable charging times. An overview of ionic conductivities reported previously for a variety of materials is given in Table 1.

***Table 1.*** *Summary of synthesis methods for different solid-state fluoride electrolytes with their electrochemical properties. RT refers to room temperature. *LBF: $La_{0.9}Ba_{0.1}F_{2.9}$.*

| Solid-state Fluoride electrolyte | Ionic conductivity: σ (S·cm$^{-1}$) | Synthesis Method | Anode / Cathode | Capacity (mAh g$^{-1}$) at 1$^{st}$ discharge | Discharging stability (mAh g$^{-1}$) | Coulombic Efficiency (at 1st cycle) | Current density | Ref. |
|---|---|---|---|---|---|---|---|---|
| $La_{0.95}Ba_{0.05}F_{2.95}$ | $1.26 \times 10^{-4}$ (60°C) | Co-precipitation method | Ce/$BiF_3$ (150 °C) | 245 | 90 (8$^{th}$ cycle) | 83 % | 4 mA g$^{-1}$ | [43] |

| | | | | | | | | |
|---|---|---|---|---|---|---|---|---|
| $La_{0.90}Ba_{0.10}F_{2.90}$ (90 µm)/$BaSnF_4$ (650 µm) | $3.5 \times 10^{-6}$ (RT) | High energy ball milling + annealing | $Ce/BiF_3$ (25 °C) | 27 | 3 (5th cycle | 85% | 10 µA $cm^{-2}$ | 67 |
| | | | $Ce/BiF_3$ (150 °C) | 251 | 119 (5th cycle) | 93 % | 10 µA $cm^{-2}$ | |
| $La_{0.95}Ba_{0.05}F_{2.95}$@PEO | $5.75 \times 10^{-6}$ (90℃) | Co-precipitation method | $Li/FeF_3$ (70 °C) | 113.5 | 18 (5th) | 92 % | 71 mA $g^{-1}$ | 100 |
| $La_{0.90}Ba_{0.10}F_{2.90}$ | $1.20 \times 10^{-6}$ (RT) | High energy ball-milling + sintering | Not reported | | | | | 101 |
| $La_{0.90}Ba_{0.10}F_{2.90}$ | $4 \times 10^{-7}$ (RT) | High energy ball milling | See Table 3 | | | | | 67 |
| $La_{0.90}Ba_{0.10}F_{2.90}$ | $2.36 \times 10^{-4}$ (200℃) | High energy ball milling | | | | | | 102 |
| $La_{0.95}Sr_{0.05}F_{2.95}$ | $2.0 \times 10^{-6}$ (RT) | Single crystal | Not reported | | | | | 103 |
| $La_{0.8}Ca_{0.2}F_{2.8}$ | $1.0 \times 10^{-6}$ (RT) | Ball-milling + annealing | Not reported | | | | | 55 |
| $La_{0.95}Sr_{0.05}F_{2.95}$ | $3.0 \times 10^{-5}$ (RT) | Single crystal + high energy ball-milling + sintering | Not reported | | | | | 104 |
| $Sm_{0.95}Ca_{0.05}F_{2.95}$ | $1.0 \times 10^{-4}$ (RT) | Sintering + solid state synthesis + mixing | Not reported | | | | | 49 |
| $Sm_{0.95}Ca_{0.05}F_{2.95}$ | $2.8 \times 10^{-5}$ (RT) | High energy ball-milling | Not reported | - | - | 1 µA $cm^{-2}$ | 80,107 | |
| β-$PbSnF_4$ | $1.20 \times 10^{-3}$ (RT) | Sintering + mixing | Not reported | | | | | 87, |
| $Pb_{0.55}Sn_{0.45}F_2$ | $2.53 \times 10^{-3}$ (RT) | High energy ball-milling | Not reported | | | | | 76 |
| $Pb_xSn_{2-x}F_4$ ($x$ = 1.21) | $3.53 \times 10^{-3}$ (RT) | High energy ball-milling + Annealing | Not reported | | | | | 77 |

## 5 Liquid and Polymer-based Electrolytes for Fluoride-Ion Batteries

Fluoride ion batteries have mostly been studied using solid electrolytes, mainly leading to operating temperatures of 150 °C or even above. However, more and more reports have been demonstrating the fluoride ion battery concept using a liquid electrolyte in very recent years.

The preparation of liquid electrolytes for FIBs is significantly different as compared to LIBs. For Li-ion batteries, liquid electrolytes typically consist of simple lithium salts such as $LiPF_6$ or $LiClO_4$ in organic solvents. However, this cannot be mimicked for fluoride ion batteries because simple fluoride salts such as KF and CsF are almost insoluble in organic aprotic solvents. So far, two strategies were adopted to prepare fluoride ion conducting liquid electrolytes: The first one is by dissolving fluoride salts in organic solvents, and the second one is by mixing organic fluorides into ionic liquids (ILs). For the latter, only one patent has claimed the fabrication of a FIB cell using an IL based electrolyte, which was composed of tetramethylammonium fluoride (TMAF) and 1-methyl-1-propylpiperidinium bis(tri-fluoromethanesulfonyl)imide (MPPTFSI).[108] The assembled cell showed an electrochemical performance for two cycles with an initial capacity of 103 mAh $g^{-1}$, but the structural data of electrodes before and after discharge was not reported. To date, several patents have been reported, claiming the feasibility of FIBs containing a liquid electrolyte.[109-112] Thus, several attempts have been made in order to develop liquid fluoride conducting electrolytes and test them in battery setups. In an initial report, Gschwind et al. prepared a polymer-based electrolyte based on ammonium bifluoride-doped polyethylene glycol

(PEG) matrix.[33, 113] Their objective was to form a hydrogen-bonded PEG matrix to trap difluorides for fluoride conduction. Figure 11a shows a schematic drawing of the possible hydrogen bonding, which could be expected in a polymer electrolyte containing bifluoride ions ($FHF^-$). The electrolyte showed an ionic conductivity of 2.1 mS $cm^{-1}$ at room temperature for an optimized concentration of 0.02 M. The assembled cell with $BiF_3$ as the cathode, Mg as the anode and this polymer electrolyte showed a good first discharge capacity. However, it fails to deliver any reversible capacity (Figure 11b). To find the exact reason of the non-reversibility of the cell, SEM analysis was performed on the Mg electrode before and after discharging, which reveals a snowflake-like formation of $MgF_2$ layers on the Mg surface.[113] This is a very poor ionic conductor, acts as a passivation layer for $F^-$ diffusion, and can be considered as the main reason for irreversibility. Recently, a new fluoride ion-conducting polymer system consisting of poly(ethylene)oxide (PEO), metal fluoride salts, and anion acceptors has been reported.[114] The polymer electrolyte exhibited the ionic conductivity of $1 \times 10^{-6}$ S $cm^{-1}$ at 303 K, with fluoride transference numbers as large as 0.8. A FIB utilizing a liquid electrolyte for fluoride transport was reported recently by Ogumi et al., where the electrolyte was made from mixing an organic fluoride (1-methyl-1-propylpiperidinium fluoride: MPPF) in an ionic liquid (N,N,N-trimethyl-N-propylammonium bis(trifluoromethanesulfonyl)amide: TMPA/TFSA).[115] The electrolyte shows a conductivity of 2.5 mS $cm^{-1}$ at room temperature for a concentration of 0.35 M. The electrochemical stability of the electrolyte was investigated by cyclic voltammetry using Pt or Bi as working electrode, and a fluorinated Pb plate as counter and reference electrode (Figure 11c), indicating a small electrochemical stability window of 0.7 V vs $Pb/Pb^{2+}$. The full cell assembly utilizing the electrolyte showed significant charge and discharge capacities for few cycles at low operating voltage (~ 0.2 V) (Figure 11d).

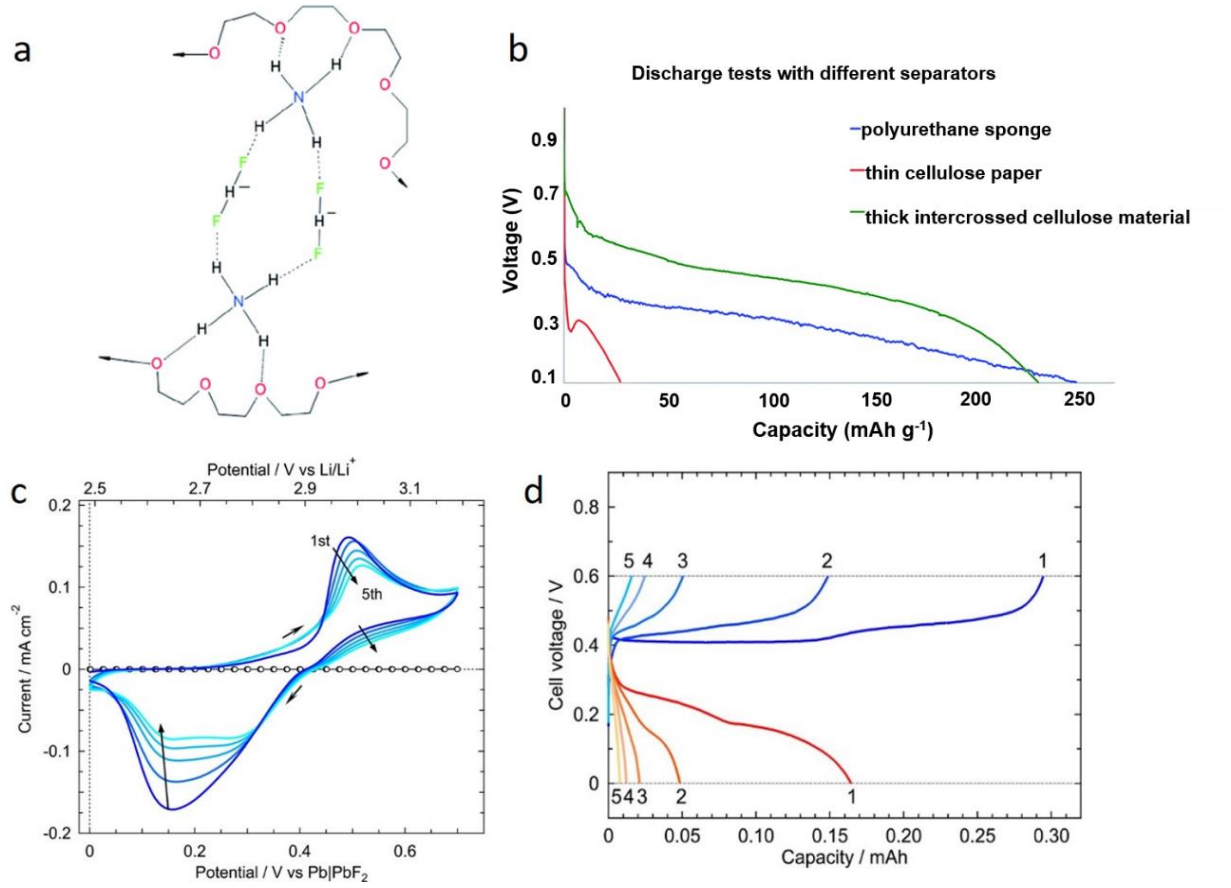


*Figure 11 (a) A schematic drawing of possible hydrogen bonds, which could occur in a hydrogenbifluoride-doped PEG matrix (reproduced from ref.[33] (an original RSC publication)), (b) Discharge curves of $BiF_3$ against Mg using PEG matrix based electrolyte with three different separators (reproduced with some modifications from ref.[113] (an original RSC publication)), (c) CVs of the Bi and Pt electrodes in ~ 0.07 mol.dm$^{-3}$ MPPF/TMPA-TFSA at a scan rate of 1.0 mV.s$^{-1}$ (Blue lines: Bi. Gray lines with circles: Pt), (d) Cycling test of the bismuth electrode in ~ 0.35 mol dm$^{-3}$ MPPF/TMPA-TFSA at current densities of 20 µA.cm$^{-2}$ (parts c and d are reproduced from ref.[115] with permission[xi]).*

Later, the same group has further developed FIBs by introducing a new type of electrolyte synthesized by dissolving a fluoride salt in an organic solvent with the help of an anion acceptor.[116] The idea was to develop an electrolyte that can dissolve and deposit the active material to facilitate the electrochemical reaction of FIBs. The electrolyte solution was prepared by using bis [2-(2-methoxyethoxy) ethyl] ether (tetraglyme:G4) as the solvent containing 0.45 M cesium fluoride (CsF) with addition of 0.5 mol $L^{-1}$ of a boron-based anion acceptor (fluorobis (2,4,6-trimethylphenyl) borane: FBTMPhB). The anion acceptor was added mainly to enhance the solubility of CsF in the tetraglyme solvent by reducing the cation-anion interaction between $Cs^+$ and $F^-$. DFT calculations confirm the capability of FBTMPhB as anion acceptor to bind fluoride ions. Figure 12a shows the most stable binding site for the fluoride ion at the boron atom. The electrochemical stability of this liquid electrolyte was investigated by cyclic voltammetry (displayed in Figure 12b), where the CsF(0.45)-FBTMPhB(0.5)-G4 composition shows a stability window between -2.2 to -0.3 V vs. $Ag/Ag^+$. Furthermore, the performance of this electrolyte was demonstrated in a FIB half cell constituting of $BiF_3$ as a working cathode and a Pt mesh as a counter electrode. The cell delivered a first discharge capacity of 316 mAh $g^{-1}$ (slightly higher than

[xi] Copyright © 2017 American Chemical Society

the theoretical capacity, indicating some side reactions), but in the subsequent cycles the capacity faded rapidly and decreased close to zero after 10 cycles. The electrochemical performance of $PbF_2$ as an active material has also been investigated within a FIB system with the same liquid electrolyte.[117] In this work, the discharge capacity reduced to almost half after only three cycles, though, the XRD measurements confirm occurrence of the charge/discharge reactions within the second and third cycles.

Later, the effect of two other boron-containing compounds, triphenylboroxine (TPhBX) and triphenylborane (TPhB), as anion acceptors was investigated.[118] The authors concluded that the addition of TPhBX and TPhB can significantly increase the solubility of CsF in G4. Still, a significant capacity fading (from ~350 mAh $g^{-1}$ in the first cycle to ~75 mAh $g^{-1}$ in the third cycle for CsF-TPhB-G4) can be observed during the cell operation. A similar argument holds true when $PbF_2$ is used as the electrode material instead of $BiF_3$.[119] This poor behavior of TPhBX has been related to the dissolution of Bi[120] and Pb[119] ions. It is also shown that the amount of CsF in the solution can influence the cycling stability: The discharge capacity of the system based on the electrolyte with G4 containing saturated CsF and 0.50 M TPhBX can increase the discharge capacity of $BiF_3$ in the second and third cycles to almost 100 % as compared to that within the system based on the electrolyte with G4 containing 0.45 M CsF and 0.50 M TPhBX.[120] In the same system, other factors such as microparticulation of the $BiF_3$ and adhesion of the conductive material to $BiF_3$ by ball milling were investigated later, showing that while reducing the particle size only slightly affects the practical capacity, adhesion of the $BiF_3$ to carbon particles can significantly increase the charge/discharge capacities.[121] To further improve the cycling performance, a $PbF_2$ electrode was later used by the same research group to build up a FIB cell based on bis[2-(2-methoxyethoxy)ethyl] ether containing cesium fluoride and TPhB as the electrolyte.[122] This resulted in a better capacity retention during the first three cycles (~210 mAh $g^{-1}$ and ~100 mAh $g^{-1}$ at the first and third cycles, respectively) as compared to that with $BiF_3$ as the electrode material.[123, 124] In another study,[125] $PbF_2$ has been investigated using a similar liquid-based electrolyte but with the addition of TPhBX as the anion acceptor. There, the effects of pulverization of $PbF_2$ and carbon additive were elaborated and the authors conclude that a mixture of $PbF_2$ and carbon, which is pulverized by ball milling, can increase the capacity of the cell.

A liquid fluoride conducting electrolyte with high ionic conductivity and wide electrochemical stability was designed and developed by Davis et al.[34] A highly concentrated (>2.2 M) electrolyte was synthesized by dissolving dry N,N,Ntrimethyl-N-neopentylammonium fluoride (Np1F) in the organic solvent Bis(2,2,2-trifluoroethyl) ether (BTFE) (Figure 12c). They also investigated the solubility of Np1F in several non-aqueous solvents in order to find the most suitable electrolyte for FIBs.[126] The 0.75 M Np1F/BTFE electrolyte, in particular, displays ionic conductivity of 7.95 mS $cm^{-1}$ at room temperature. The electrochemical stability window of 0.75 M Np1F/BTFE was determined by linear sweep voltammetry, showing a potential window between 0.7 V (cathodic voltage limit) and 4.8 V (anodic voltage limit) versus $Li^+/Li$ (Figure 12d). However, the electrochemical cycling of various metallic electrodes (such as: Cu, Pb, Bi, Ce and Ca) revealed that there is a considerable amount of metal dissolution into the electrolyte, which leads to poor performances. To avoid the electrolyte breakdown due to direct contact with the metal, a fluoride conductive layer protecting the electrode materials was introduced. The Ce electrode was engineered with a fluorinated solid electrolyte interphase (SEI) layer, whereas Cu particles were encapsulated in a thin layer of $LaF_3$ in a core-shell setup, referred to as Cu@$LaF_3$. The fabricated

cell comprised of the modified electrodes and the liquid electrolyte was cycled reversibly at room temperature with a reversible capacity of around 60 mAh $g^{-1}$, which is 8 times less than the theoretical capacity of $CuF_2$ (528 mAh $g^{-1}$), meaning an incomplete reaction occurred at the electrodes. Another report describes a new electrolyte based on fluorohydrogenate ionic liquid [C2C1im][(FH)2.3F] (C2C1im = 1-ethyl-3-methylimidazolium), with an ionic conductivity as high as 100 mS $cm^{-1}$ at 25 °C.[127] Here, the FIB cell with $CuF_2$ cathode delivered an excellent first discharge capacity of 500 mAh $g^{-1}$, which is close to the theoretical capacity of $CuF_2$. The reversible capacity reaches to 475 mAh $g^{-1}$ during the first cycle, resulting in a Coulombic efficiency of 92 %, which is already higher than the value observed in previous reports. In the following cycles, the performance of the cell degraded gradually; as result, the $10^{th}$ reversal capacity reaches to 264 mAh $g^{-1}$. Thus, one can conclude that realizing full utilization of active material at room temperature is a very challenging task, whose implementation requires the development of other electrolytes.

Apart from using organic solvents to develop liquid electrolytes for FIBs, aqueous solutions have also been considered for the same purpose. For instance, cells based on fluoride and sodium ion (dual) transfer were proposed by Zhang et al.[128] In their study, aqueous sodium fluoride was used as a liquid electrolyte while $BiF_3$ and sodium manganese oxides (NMO) were used as the positive and negative electrodes, respectively. The cell delivered a reversible and stable discharge capacity of 47.3 mAh $g^{-1}$ after 40 cycles. A NaF salt solution has also been used as a liquid electrolyte to build up a FIB cell by Hou et al.[129] In this study, $BiF_3$ has been used as an anode and cycled against a 4-hydroxy-TEMPO cathode, i.e., a persistent radical that is sterically protected by four α-methyl groups and undergoes one electron oxidation.[129] The electrodes were implemented as a paste (slurry method) on graphite paper and a high-quality anion exchange membrane was used to prevent side effects of insoluble compounds ensuring only fluoride ions are transported during the operation of the cell. Here the results show stable cycling performance at least for 85 cycles with a reversible capacity of around 90 mAh $g^{-1}$. However, a relatively large voltage hysteresis (~ 1.0 V on average) can be observed.

A summary of the reported liquid electrolytes and their electrochemical properties can be found in Table 2.

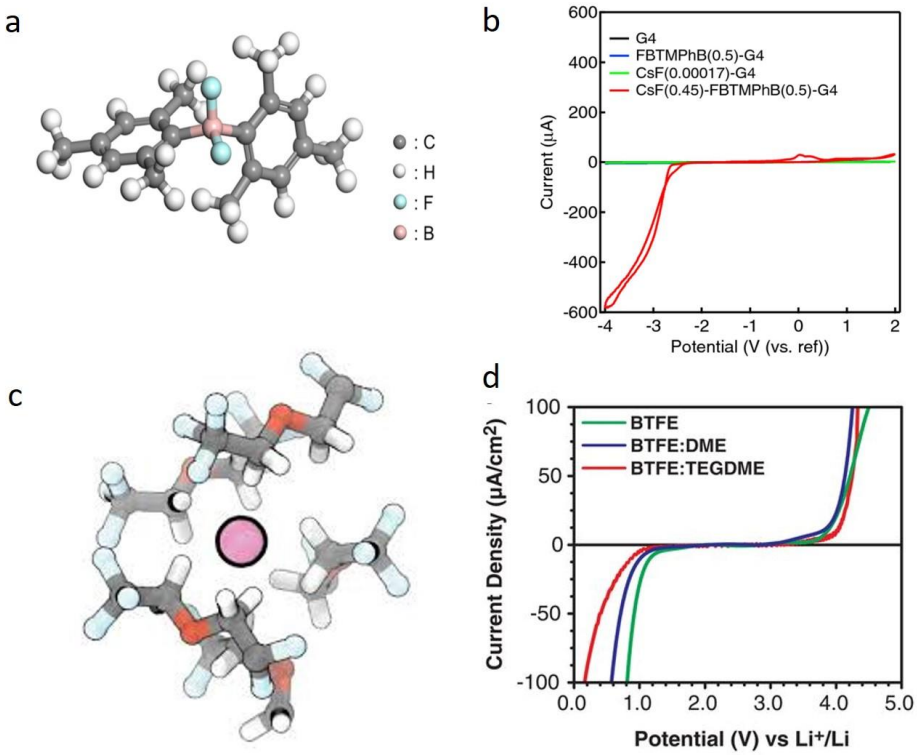


Figure 12. (a) *Optimized molecular structure of FBTMPhB−F⁻, (b) Cyclic voltammograms of the CsF(0.45)-FBTMPhB(0.5)-G4 (parts a and b are reproduced from ref.[116] with permission[xii]); (c) Simulated solvation shell of BTFE molecules surrounding F⁻ (pink sphere) (d) Linear sweep voltammograms for 0.75 M Np1F in BTFE, collected using a scan rate of 1 mV.s$^{-1}$. (parts c and d are reproduced from ref.[34] with permission[xiii]).*

[xii] Copyright © 2017 The Electrochemical Society
[xiii] Copyright © 2019 American Association for the Advancement of Science.

*Table 2. Liquid electrolytes for FIBs and their electrochemical property.*

| Electrolyte | σ (S $cm^{-1}$) at 25 °C | Stability -Window (V) | Anode / Cathode | Capacity (mAh $g^{-1}$) 1st discharge | Cycle life (mAh $g^{-1}$) discharge | Coulombic Efficiency (at 1st cycle) | Current density | Ref. |
|---|---|---|---|---|---|---|---|---|
| 0.1M TMAF/MPPTFSI | $1 \times 10^{-3}$ | -3.5 to 4.0 (vs $Ag/Ag^{+}$) | $PbF_2$ / PANI | 103 | 96 (2nd) | 49% (ca.) | - | 108 |
| 0.02M FHF doped PEG | $2.1 \times 10^{-3}$ | - | Mg / $BiF_3$ | 250 | - | - | 10 µA | 33 |
| 0.35M MPPF/TMPA-TFSA | $2.5 \times 10^{-3}$ | 0 to 0.7 (vs $Pb/PbF_2$) | $PbF_2$ / Bi | 0.16 mAh | 0.01 mAh (5th) | 56% | 20 µA $cm^{-2}$ | 115 |
| CsF(0.45M)-FBTMPhB(0.5M)-G4 | - | -2.2 to -0.3 (vs $BiF_3$/Bi) | Pt / $BiF_3$ | 316 | Close to 0 (10th) | 70 % | 7.5 mA $g^{-1}$ | 116 |
| 0.75 M Np1F/BTFE | $7.9 \times 10^{-3}$ | 0.7 to 4.8 (vs $Li/Li^{+}$) | Pt / Cu@$LaF_3$ | 50 | 63 (7th) | 78 % | 10 µA | 34 |
| [C2C1im][(FH)2.3F] | $1 \times 10^{-1}$ | -0.3 to 0.7 (vs $CuF_2$/Cu) | $CuF_2$ / Cu+$CuF_2$ | 517 | 270 (10th) | 92% | 26 mA $g^{-1}$ | 127 |
| 1M $LiPF_6$ in EC/DME | - | 0 to 3.0 (vs $Mg/MgF_2$) | Mg+$MgF_2$ / $BiF_3$ | 160 | 27 (10th) | 53% | 38 µA $cm^{-2}$ | 130 |
| | | | Mg+$MgF_2$ / $SnF_2$ | 142 | 24 (10th) | 56% | 38 µA $cm^{-2}$ | |
| P(EO/PO)/MF/AA | $1 \times 10^{-6}$ | - | - | - | - | - | - | 114 |
| Aqueous 0.8 M NaF | - | 0 to 1.5 (Ag/AgCl) | NMO / $BiF_3$ | 137 | 47 (40th) | 52% | 100 mA $g^{-1}$ | 128 |

# 6 Electrode Materials

## 6.1 Conversion Vs. Intercalation Mechanism

In fluoride ion battery systems, storage of the ions in electrodes can take place through two main types of reaction mechanisms. As it was highlighted in section 3, the suitability of FIBs for reversible energy storage systems has been first demonstrated for cells containing conversion-based electrode materials. Such conversion-based electrodes generally offer the highest specific capacities due to their ability to accommodate more electrons per redox-active metal species and often lower molar mass of the active electrode material. However, in a conversion-reaction, the electrode material undergoes a redox reaction during fluorination/de-fluorination, which is accompanied by a change in the crystal structure leading to breaking and recombining of the chemical bonds and often a large volume change in the active electrode material.[1] This large volume change results in a loss of physical contact between the active electrode material, the conductive particle and the ion conductor (see the scheme in Figure 13), which can lead to a significant deterioration in the electrochemical performance of the electrode material.

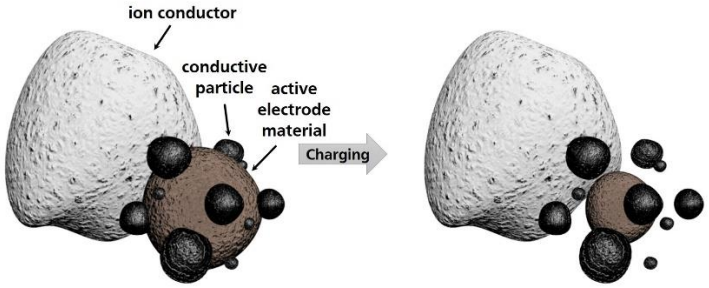


*Figure 13. Schematic illustration of the volume changes in the contact surface area of the active anode material/electrolyte/carbon grains taking place during electrochemical charge/discharge. Reproduced from ref.[28].*

The second reaction for storage of the fluoride ions is based on the intercalation mechanism (sometimes also called insertion or solid solution reactions,[131] depending on the detailed structural arrangement of the host and the substructure of the incorporated species and nature of bonding therein). In the following, we refer to an intercalation-based electrode material for FIBs as a solid host network, which can store guest ions within the vacant positions in the host lattice, without referring to the dimensionality of this host sublattice explicitely. In other words, the guest species are inserted into normally unoccupied interstitial sites or anion vacancies in the crystal structure of a stable host material. The great advantage of the intercalation-based electrode materials relates to the fact that the ions can be inserted or removed into/from the host network reversibly with much lower volume changes during the redox reaction (e.g., in the order of 2 % for $LiCoO_2$[132] as an intercalation-based cathode for lithium-ion batteries) while the basic crystal structure or amounts of the phase in the microstructure do not change significantly.[131] Therefore, intercalation-based electrode materials can often provide a better cycling performance as compared to conversion-based electrode materials, with improved charging and discharging rates. However, this normally comes at the cost of lower specific capacities [1], as intercalation-based materials are usually heavier in weight than the conversion-based electrode materials due to the existence of redox-inactive lattice atoms within the materials and the capability of accommodating fewer ions per redox-active species (for instance, theoretical capacity for intercalation-based $LiCoO_2$ is calculated to be 140 mAh $g^{-1}$, for lithiation/de-lithiation of 0.5 Li-ions [133] in comparison to conversion-based $Li/Li_2S$[1] with a theoretical capacity of 1675 mAh $g^{-1}$).

The following sections aim to provide an overview of the different electrode materials investigated previously. Table 3 provides an overview about the cathode and anode materials that have been developed so far for the FIB systems and briefly summarize their electrochemical performances. It is also worth mentioning that as yet no evidence suggests the migration of other ions such as La, Sn or Sr ions during the redox reactions within the reviewed FIB systems. These ions have low mobility at the temperatures used for the battery experiment as compared to $F^-$, and those ions cannot take the same diffusion paths as $F^-$ within the ionic lattice.

*Table 3. A summary of the electrochemical performances of different cathode/anode materials that will be discussed in this section. *$La_{0.9}Ba_{0.1}F_{2.9}$; §$Ce_{0.95}Ba_{0.05}F_{2.95}$; ¥$BaSnF_4$.*

| Cathode/Electrolyte/Anode | Average discharge potential range (V) | 1st discharge capacity (mAh $g^{-1}$) | Cycling performance | T (°C) | Current density | Ref. |
|---|---|---|---|---|---|---|
| $BiF_3$ (composite)/LBF*/Ce | ~2.5 | ~125 | Not reported | 150 | 10 μA $cm^{-2}$ | 8 |
| $BiF_3$ (solid-solution)/LBF*/Ce | ~2.15 | ~190 | 26 % capacity retention after 40 cycles | 150 | 10 μA $cm^{-2}$ | 8 |
| $BiF_3$/(co-precipitated LBF* electrolyte)/Ce | ~2.4 | ~250 | Discharge capacity: 90 mAh $g^{-1}$ at cycle 8 | 150 | ±4 mA $g^{-1}$ | 43 |
| $BiF_3$/LBF*/Ce | Dropped rapidly | <5 [1] | No cycle life | 150 | ±4 mA $g^{-1}$ | 24 |
| $BiF_3$/LBF*/Mg | Dropped rapidly | <5 | No cycle life | 150 | ±4 mA $g^{-1}$ | 24 |
| $BiF_3$/LBF*/Mg+$MgF_2$ | 2.1 – 2.7 | ~80 | <25 mAh $g^{-1}$ at cycle 10 | 150 | ±4 mA $g^{-1}$ | 24 |
| $Bi_{0.7}Fe_{1.3}O_{1.5}F_{1.7}$/CBF§/Pb | ~0.3 | 360 | Not reported | 140 | | 135 |
| $CuF_2$/LBF*/Ce | ~2.5 | ~322 | Not reported | 150 | 10 μA $cm^{-2}$ | 8 |
| $CuF_2$/LBF*/Mg+$MgF_2$ | ~2.8 – 1.5 | 33 | <20 mAh $g^{-1}$ after cycle 10 | 150 | ±4 mA $g^{-1}$ | 24 |
| Cu@LaF3 in standard three-electrode cell/1 M Np1F\|BTFE/Pt wires | ~2.3 – 2.0 | ~52 | Low capacity fading over first 7 cycles | RT | 10 μA | 34 |
| $SnF_2$/LBF*/Ce | ~2.1 | ~180 | Not reported | 150 | 10 μA $cm^{-2}$ | 8 |
| $KBiF_4$/LBF*/Ce | ~2.2 | ~170 | Not reported | 150 | 10 μA $cm^{-2}$ | 8 |
| Sn/BSF¥/$BiF_3$ | ~0.3 – 0 | ~120 | Large capacity fading from ~120 mAh $g^{-1}$ at the 1st cycle to <10 mAh $g^{-1}$ at cycle 10 | 25 | ±10 μA $cm^{-2}$ | 65 |
| Zn/BSF¥/$BiF_3$ | ~0.5 –0 | ~60 | Cycle stable up to cycle 20 | 25 | ±10 μA $cm^{-2}$ | 65 |
| $La_2NiO_{4+d}$/LBF*/Zn+$ZnF_2$ | ~1.3 – 0.5 | 72 | Cyclic stability over 220 cycles only at cutoff voltage of 30 mAh $g^{-1}$ | 170 | +24 μA $cm^{-2}$ -12 μA $cm^{-2}$ | 134 |
| $La_2NiO_{4+d}$/LBF*/Pb+$PbF_2$ | ~0.9 – 0.3 | 55 | Discharge capacity increases to 55 mAh $g^{-1}$ up to cycle 10 then reduces to 24 mAh $g^{-1}$ up to cycle 20 | 170 | +24 μA $cm^{-2}$ -12 μA $cm^{-2}$ | 28 |
| $La_2NiO_3F_2$/LBF*/Pb+$PbF_2$ | ~1.0 – 0.4 | 22.5 | Discharge capacity increases from ~12 mAh $g^{-1}$ up to ~23 mAh $g^{-1}$ at cycle 50 | 170 | 2.5 mA $g^{-1}$ | 136 |
| $La_2CoO_{4+d}$/LBF*/Zn+$ZnF_2$ | ~1.0 – 0.3 | 40 | Discharge capacity drops to 32 mAh $g^{-1}$ in the 2nd cycle then gradually reaches to 8 mAh $g^{-1}$ at cycle 50 | 170 | +24 μA $cm^{-2}$ -2.4 μA $cm^{-2}$ | 137 |
| $La_2CoO_{4+d}$/LBF*/Pb+$PbF_2$ | ~0.6 – 0.2 | 32 | Discharge capacity: ~8 mAh $g^{-1}$ at cycle 50 | 170 | +24 μA $cm^{-2}$ -2.4 μA $cm^{-2}$ | 30 |
| $LaSrMnO_4$/LBF*/$PbF_2$ | ~1.0 – 0.2 | 35 | Not reported | 170 | +24 μA $cm^{-2}$ -2.4 μA $cm^{-2}$ | 96 |
| $LaSrMnO_4$/LBF*/Pb+$PbF_2$ | ~1.0 – 0.2 | 36 | Not reported | 170 | +24 μA $cm^{-2}$ -2.4 μA $cm^{-2}$ | 96 |
| $La_{1.3}Sr_{1.7}Mn_2O_7$/LBF*/Pb+$PbF_2$ | ~0.5 - 0 | 25 | No significant capacity fading over 40 cycles | 170 | 5.1 μA | 138 |
| $LaSrFeO_4$/LBF*/Pb+$PbF_2$ | ~0.8 – 0 | 6 | Not reported | 170 | +24 μA $cm^{-2}$ -2.4 μA $cm^{-2}$ | 28 |

| | | | | | | |
|---|---|---|---|---|---|---|
| $LaSrCoO_4$/LBF*/Pb+$PbF_2$ | ~0.8 – 0 | 16 | Not reported | 170 | +24 μA $cm^{-2}$<br>-2.4 μA $cm^{-2}$ | [28] |
| $Co_{0.5}Fe_{0.5}Sb_2O_4$/LBF*/Pb+$PbF_2$ | ~0.5 – 0 | 6 | Not reported | 170 | +24 μA $cm^{-2}$<br>-2.4 μA $cm^{-2}$ | [139] |
| $Mg_{0.5}Fe_{0.5}Sb_2O_4$/LBF*/Pb+$PbF_2$ | ~0.5 – 0 | 3 | Not reported | 170 | +24 μA $cm^{-2}$<br>-2.4 μA $cm^{-2}$ | [139] |
| $BaFeO_{2.5}$/LBF*/$MgF_2$ | ~2.5 – 1.0 | 6 | Only three cycles were reported which shows a slight capacity fading | 150 | 10 μA $cm^{-2}$ | [140] |

## 6.2 Conversion-based Cathode Materials

$BiF_3$ and $CuF_2$ are by far the most used cathode materials in conversion-based FIBs.[8, 24, 33, 34, 65, 141] Reddy and Fichtner reported on the cycling behaviour of $BiF_3$ as cathode material against a Ce anode material in an all-solid-state cell modification using $La_{0.9}Ba_{0.1}F_{2.9}$ as the electrolyte.[8] In addition, they reported the first discharge behaviour of several metal fluorides. Figure 14 summarizes the first discharge profile of various metal fluorides as cathode materials (against Ce anode material) compared to $BiF_3$ and $CuF_2$. It is worth mentioning that in this study the cathode materials were made in a charged state (i.e., $MF_x$). The results revealed that for the $CuF_2$ composite material the highest discharge capacity of 322 mAh $g^{-1}$ (in the first cycle) with a flat discharge potential of around 2.7 V could be obtained when the cell was discharged at 150 °C using a current density of 10 μA/$cm^2$. The high discharge capacity of $CuF_2$ is due to the high theoretical capacity of $CuF_2$, which arises from the low molar mass of Cu (e.g. theoretical capacities of Cu/$CuF_2$ and Bi/$BiF_3$ are calculated to be ~ 843 and 384 mAh $g^{-1}$, respectively). The Cu/$CuF_2$ redox couple has been used as a conversion-based cathode in a nanostructure core-shell modification,[34] as discussed in section 5. For the $BiF_3$ cathode composite, a flat plateau around 2.5 V with a discharge capacity of 126 mAh $g^{-1}$ was observed. The discharge capacity could be further increased up to 190 mAh $g^{-1}$ by synthesizing a $BiF_3$ (tysonite-type) solid solution (via mechanical milling of the $BiF_3$ active cathode material together with the electrolyte material with increased rotational speed up to 600 rpm). However, the average discharge potential slightly reduced to ~ 2.15 V for the $BiF_3$ solid solution. The improvement of the discharge capacity has been attributed to a higher fluoride ion mobility within the $BiF_3$ solid solution as compared to a $BiF_3$ composite.

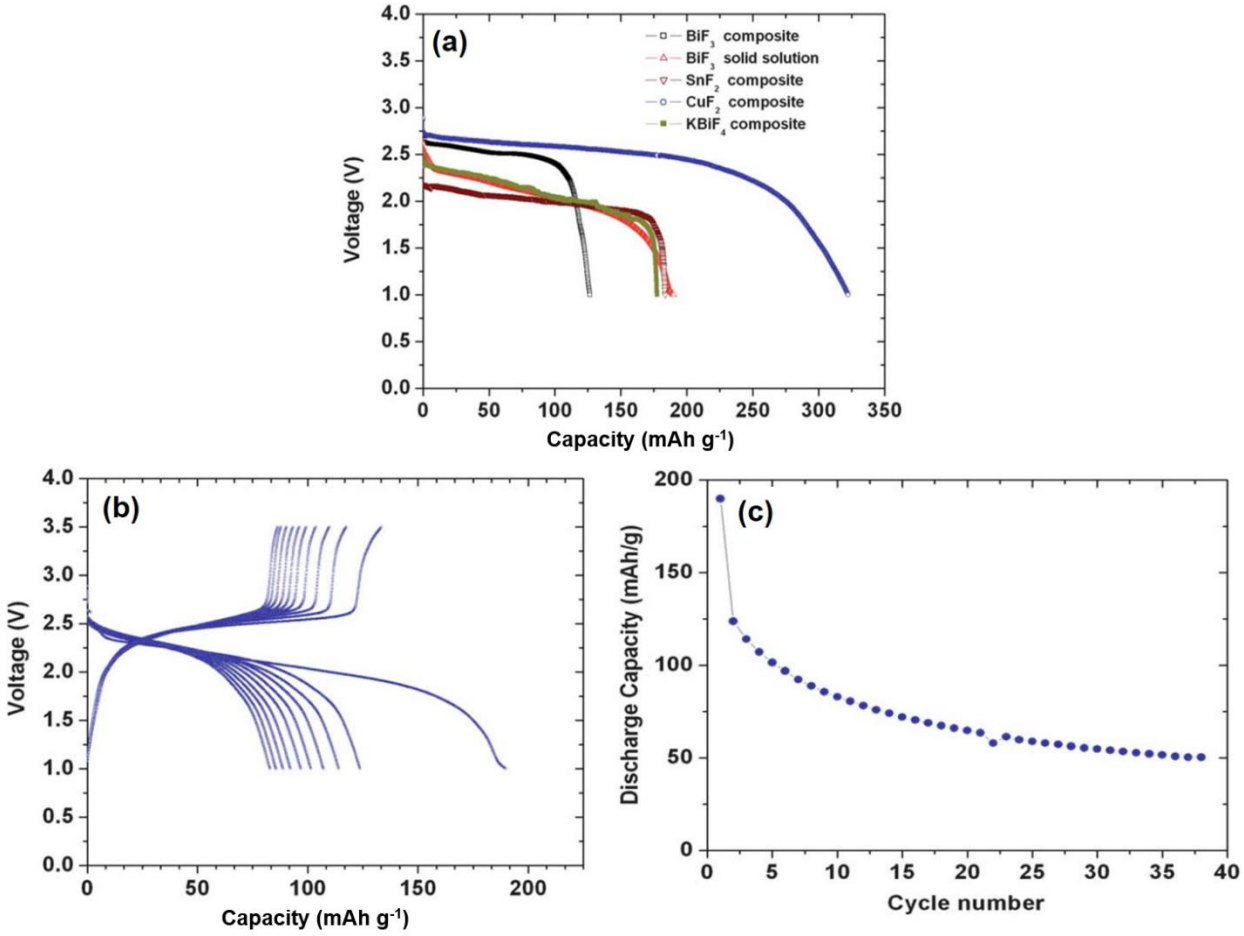


*Figure 14. (a) Voltage-capacity profiles of various metal fluorides vs. Ce metal. The discharge curves were obtained at 150 °C with a current density of 10 mA/cm$^2$; (b) Cycling performance of the $BiF_3$ (solid solution)/Ce cell for the first 10 cycles; (c) changes of discharge capacity with cycle numbers for the same electrochemical cell. The figures have been reproduced with some modifications from ref.[8] (an original RSC publication).*

The cycling performance of $BiF_3$ against Ce reveals a large capacity loss (~ 35 %) already after the first cycle, followed by rapid capacity fading over the next cycles, leading to only ~ 26 % capacity retention after 40 cycles (see Figure 14b, c). Interestingly, it was found that synthesizing the $La_{0.9}Ba_{0.1}F_{2.9}$ solid electrolyte by co-precipitation could lead to a significant increase in the discharge capacity of a $BiF_3$|Ce electrochemical cell of up to 250 mAh g$^{-1}$. Though the cell still suffered from a strong capacity fading upon cycling (the discharge capacity reached to 90 mAh g$^{-1}$ after only 8 cycles, when the cells were cycled at 150 °C), these findings indicate that the performance of certain electrode materials can highly depend on the detailed morphological and compositional aspects of the solid electrolyte used in the electrode composite mixture.[43]

Cathode composites of Bi+$BiF_3$ were also studied in detail by Grenier et al.[142] by means of pair distribution function analysis of synchrotron data, revealing a complex transformation reaction comprising also the formation of oxyfluoride compounds at intermediate cycling states. Further, they could show that such oxide impurities cannot migrate through the fluoride conducting electrolyte, and thus remain at the respective electrode side.

In another report,[24] electrochemical activities of Bi and Cu (active cathode materials in discharged states) against $CeF_3$, $CaF_2$, $MgF_2$ and $Mg+MgF_2$ anode composites have been studied. The results suggested that the electrochemical fluorination of Bi against $CeF_3$ (during charging) takes place in several steps as was found by Grenier et al.[142] and that the transformation process can be very complex: First, traces (remaining from the starting powder) of $Bi_2O_3$ were fluorinated, and $\beta$-$BiF_{3-2x}O_x$ is formed, which was accompanied by a charge plateau below 2.4 V. In the second step, $BiF_3$ forms from Bi (desired reaction) and a plateau between 2.5 − 2.7 V could be observed. The last step was referred to as the formation of $BiF_5$ from previously formed $BiF_3$. Considering the theoretical capacity related to the reaction of three fluoride ions with Bi (385 mAh $g^{-1}$), the first charge capacity was ~ 404 mAh $g^{-1}$, indicating that a reaction of $BiF_3$ to $BiF_5$ might be partly involved in the redox process. Other possibilities such as carbon or electrolyte decomposition were not evaluated as the source of the side reaction related to the observed excessive charge capacity. When using the other mentioned anode materials, similar charging behaviors were found. However, a considerable reversibility upon discharging could only be obtained when using $CeF_3$ and $MgF_2$ based anode composites. A significant improvement of the cyclability was further observed when a $Mg+MgF_2$ anode composite, containing a mixture of Mg and $MgF_2$, was used (see also section 6.3).

A slightly improved cycling stability has been reported[31] for Bi|$CaF_2$ cells using a thin film $La_{0.9}Ba_{0.1}F_{2.9}$ electrolyte (see also section 4.2). In this study, $SnO_2$ and indium tin oxide (ITO) instead of carbon nanotubes as the electronic conductor have been investigated to study the role of the electron-conducting additive for the electron transfer to the active electrode material. It was observed that the best cycling behavior could be observed using carbon nanotubes as the electronic conductor. Despite of a low Coulombic efficiency in the first cycle (the cell has been initially charged up to ca. 320 mAh $g^{-1}$ but only 120 mAh $g^{-1}$ could be reversed), in the next cycles, the capacity fading was less severe compared to the first cycle. Nevertheless, the discharge capacity reached to ca. 66% of its initial value (~ 120 mAh $g^{-1}$) within only 10 cycles. Recently, Konishi et al. showed [121] that pulverization of $BiF_3$ with the conductive material by ball milling can improve the practical capacity of the FIB system. This has been explained by the reduction of the particle size and a stronger adhesion of the conductive particle to the $BiF_3$ electrode material. Another approach to improve the capacity retention of $BiF_3$ was proposed very recently by Konishi et al.[143] In this publication, it was shown that a solid solution of $BiF_3$ and $BaF_2$ ($Bi_{1-x}Ba_xF_{3-x}$, $0<x<0.4$) as the cathode material made by mechanical alloying, offers a higher capacity retention during cycling for x = 0.4. However, the overall capacity was reduced to almost 50 % of the one for pure $BiF_3$. This has been claimed to be due to an excess amount of barium fluoride that did not contribute to the redox reaction.

Apart from using Bi/$BiF_3$ as a cathode in an all-solid-state modification, it has also been used as the cathode in a liquid electrolyte system. In 2019 Yamanaka et al. reported [144] on using orthorhombic-$BiF_3$ microparticles in a gold plating film as a cathode material against Pb wire as the counter electrode. Then the structural transformation and reaction mechanisms within $BiF_3$ as the active electrode material were studied by means of in-situ Raman microscopy. The authors showed that by discharging the cell within a potential range of 0.45 – 0.2 V (against. Pb), a part of the orthorhombic-$BiF_3$ is deposited as Bi on the gold plate, which is indicative for a direct de-fluorination process while the rest of the orthorhombic-$BiF_3$ was transformed to cubic-$BiF_3$. The de-fluorination of the cubic-$BiF_3$ was observed only below 0.2 V (vs. Pb) and with a slower rate

as compared to orthorhombic-$BiF_3$. Moreover, it is suggested [145] that electronic diffusion is the rate-limiting process during the de-fluorination: The de-fluorination of orthorhombic-$BiF_3$ starts from the cluster that is in contact with conductive gold plate and not from the cluster that is in contact with the liquid electrolyte. This non-uniformity in the de-fluorination would not have been observed if the electronic diffusion at the surface of the $BiF_3$ cluster in contact with the liquid electrolyte was as fast as the ionic diffusion at the surface of $BiF_3$. In a recent attempt [34] to build up a room-temperature FIB, $Cu/CuF_2$ redox couple has been used as a conversion-based cathode in a nanostructured core-shell modification with a redox-inert thin shell of $LaF_3$ ($Cu@LaF_3$) around the active material. The cell was prepared as a standard three-electrode with a liquid electrolyte (also see section 5 for the view-point of the liquid electrolyte design). The results reveal that the Cu has been charged up to at least 80 mAh $g^{-1}$, of which 50 mAh $g^{-1}$ could be reversed during the first cycle. With respect to the theoretical capacity of $Cu/CuF_2$ (843 mAh $g^{-1}$) the obtained discharge capacity is much lower than the theoretical capacity. The capacity within the first 7 cycles seems to be stable, though, the Coulombic efficiency appeared to be low (<50%).

Very recently, Takami et al. have introduced the use of multinary oxyfluorides as active electrode materials.[135] In this report, by chemical fluorination with PVDF, quaternary $Bi_{0.7}Fe_{1.3}O_{1.5}F_{1.7}$ was synthesized, and then the phase was used as a charged cathode material. The $Bi_{0.7}Fe_{1.3}O_{1.5}F_{1.7}$ cathode material has been discharged against $Pb+PbF_2$ composites, and a discharge capacity of 500 mAh $g^{-1}$ has been obtained. However, this capacity is much larger than the theoretical capacity corresponding to a de-fluorination of 1.7 $F^-$ ions. Nevertheless, during the charge step, an effective charge plateau of about 190 mAh $g^{-1}$ can be observed, which is in the order of the theoretical capacity. No subsequent cycling experiments were possible for the cell, which the authors assigned to a poor reaction activity and low electronic conductivity of the active cathode material itself.[135]

### 6.3 Conversion-based Anode Materials

Due to the strong interplay between the cathode and anode, a strict separation of the influences of individual electrode materials on the cycling performance and the overall improvement of FIBs is challenging. As already introduced in the previous section, significant contributions to the development of conversion-based electrodes have been made by the research groups of Reddy and Fichtner. On the anode side, composites based on the $Ce/CeF_3$ [8, 24], $Ca/CaF_2$ [24, 31] and $Mg/MgF_2$ [24] redox couples have been intensively studied. For $Ce/CeF_3$, experiments were conducted starting from the charged state of Ce [8] as well as the discharged state of $CeF_3$.[24] As reported by Rongeat et al.[24], the use of an anode composite in a “half-discharged” state, containing a mixture of the discharge and charge products leads to the presence of more reactive interfaces within the composite and, therefore, to a better reactivity during charging ($MF_x \rightarrow M$) and discharging ($M \rightarrow MF_x$). This is shown for the cell $Bi/La_{0.9}Ba_{0.1}F_{2.9}/Mg+MgF_2$ in comparison to the cell $Bi/La_{0.9}Ba_{0.1}F_{2.9}/MgF_2$ in Figure 15. While for the cell containing the $Mg+MgF_2$ anode, reversibility upon discharging could be observed and cycling was possible, the cell with the pure $MgF_2$ anode showed a very low discharge capacity, and cycling could not be achieved. A strong capacity fading was also observed for the $Bi/La_{0.9}Ba_{0.1}F_{2.9}/Mg+MgF_2$ cell with increasing cycling number. Further, the use of composite mixtures as the starting point already indicates that the fully charged or fully discharged state might be unfavourable for maintaining the overall integrity of the electrode.

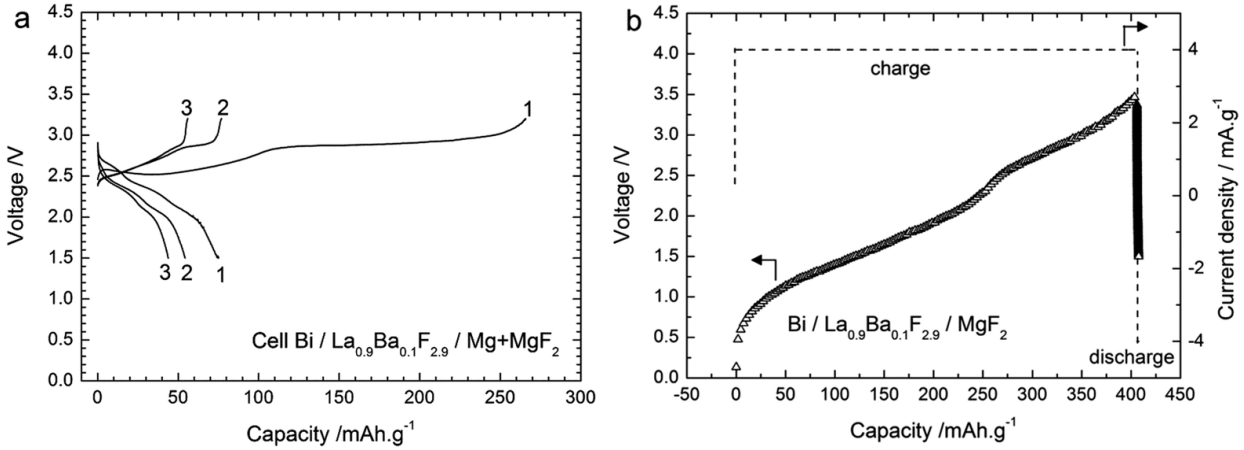


*Figure 15: Voltage profiles of the first three cycles of a cell Bi/$La_{0.9}Ba_{0.1}F_{2.9}$/Mg+$MgF_2$ (a) and of the first charging and discharging of a cell Bi/$La_{0.9}Ba_{0.1}F_{2.9}$/$MgF_2$. The cells were heated to 150 °C, a current density of 4 $mAg^{-1}$ (10 $mAcm^{-2}$) was applied. The figures have been reproduced from ref.[24] (an original RSC publication).*

The successful application of a Pb+$PbF_2$ anode composite in combination with an intercalation-based $LaSrMnO_4$ cathode in a FIB was firstly demonstrated by Nowroozi et al.[96] DFT based calculation predicted a redox potential of 2.26 V vs. Li/LiF for the Pb/$PbF_2$ redox couple, making it a suitable material for its use as anode material. Upon charging of the cell, a transformation of $PbF_2$, contained in the anode composite, into Pb takes place. As it was observed for Mg+$MgF_2$ anodes, when using this Pb+$PbF_2$ anode composite instead of a composite, containing only $PbF_2$, lower overpotentials and better cycling performances with much more pronounced charging plateaus and higher phase fractions of the fluorinated $LaSrMnO_4F_{2-\delta}$ could be identified, even though the involved redox couple remained the same. This shows that the complex conversion process taking place within the anode has a significant influence on the charging (and discharging) behavior of the cells. To gain a deeper understanding of the influence of such conversion-based anode materials on the cycling stabilities, the authors conducted an additional study, addressing the conversion reactions and determined limiting factors, including volume changes upon the occurring phase transformations.[137] Different conversion-based anodes, containing Pb and $PbF_2$, Zn and $ZnF_2$, and Mn and $MnF_2$ were investigated against an intercalation-based cathode composite containing $La_2CoO_4$ as an active material. In particular, for cells with a Mn+$MnF_2$ anode, a strong change in the impedance response due to increasing capacitive behavior was found upon charging above a certain capacity. This change was related to the strong volume decrease of $MnF_2$ when transformed to Mn ($\Delta V > 300$ %), which leads to a loss of contact between the active material and the electrolyte and carbon additive. This general dependency of cycling stabilities on the volume changes could also be confirmed based on the investigation of symmetrical cells. It was found that overpotentials increase much stronger for symmetrical cells with Zn+$ZnF_2$ electrodes over prolonged cycling in comparison to the observed stable overpotentials for respective Pb+$PbF_2$ cells, as the Zn and $ZnF_2$ undergo stronger volume changes. Overall, it appears that large and soft cations, with corresponding low melting points of the metal and high ionic conductivity within the metal fluoride state, seem to be preferable for maintaining structural integrity, which can be key for reversibility.

## 6.4 Intercalation-based Cathode Materials

Investigations on fluorine insertion in oxides via electrochemical fluorination have been performed even before the recent development of FIBs. For instance, $Y_1Ba_2Cu_3O_{7-x}$ has been electrochemically fluorinated in an all-solid-state configuration in 1991 by MacManus et al.[146] using a single crystal of Eu-doped in $LaF_3$ as the ion conductor and $Cu/CuF_2$ as the counter electrode at very high temperatures of ~ 300 °C. After careful evaluation of the structural changes upon fluorine insertion, they reached the conclusion that the electrochemical process resulted in a shrinkage of the *c* parameter of the unit cell, which has been explained by the occupation of oxygen sites by fluoride in the basal plane of the lattice. The other example is the electrochemical fluorination of $La_2CuO_4$ in a classic three-electrode configuration using organic fluorinated electrolytes (in liquid state) and gold foil and Pt wire as counter and reference electrodes, respectively.[147] In this work, it was reported that 0.18 fluoride ions had been electrochemically inserted in the vacant interlayers of $La_2CuO_4$, resulting in an increase in the parameter *c* of the cell from 13.141 Å to 13.205 Å. The results were in good agreement with what was found using chemical fluorination methods using $F_2$ gas. It should be taken into consideration that in both mentioned cases, no electrochemical reversibility has been reported since the investigations were solely devoted to the fluorine insertion (intercalation).

Attempts to develop all-solid-state FIBs based on the intercalation mechanism was first reported by Clemens et al. in 2014 on anion deficient perovskite-related $BaFeO_{2.5}$, which showed low uptake of fluoride and poor performance as a cathode material.[140] As today, the three structure types of Ruddlesden-Popper ($K_2NiF_4$-type structure), Schafarzikite ($MSb_2O_4$) and (anion deficient) perovskite ($AMO_{3-y}$) have been investigated as potential intercalation-based cathode materials for FIBs. Among these, Ruddlesden-Popper-type compounds (e.g., $La_2MO_4$ and $LaSrMO_4$) appeared to be the most promising candidates.

The Ruddlesden-Popper structure type can be regarded as a perovskite-related structure with a general formula of $A_{n+1}M_nO_{3n+1}$ (or $(AMO_3)_nAO$),[148] where n shows the number of connected layers of vertex sharing $MO_6$ (n perovskite layers are stacked between rock-salt AO layers along the *c*-axis). Figure 16 schematically illustrates the Ruddlesden-Popper-type structure with n = 1 and formula of $(ABO_3)_nAO$ (also known as $K_2NiF_4$-type structure). In a $K_2NiF_4$ ($A_2MO_4$) structure $MO_6$ octahedra share corners with each other to form $AMO_3$ (two-dimensional) perovskite layers and the AO rock salt units exist between multiple layers of the perovskite along the c-axis, resulting in a tetragonal unit cell with an aristotype symmetry of *I*4/*mmm*[148]; for compositions close to $A_2BO_4$ the lattice parameter *c* normally ranges between ~12.6 – 13.2 Å.[149-153] The vacant anion positions within the rock salt-type interlayers are suitable for the accommodation of fluoride ions (Figure 16): $K_2NiF_4$-type compounds are capable of accepting up to 2 fluoride ions per formula unit, resulting in theoretical capacities (normally between 130 – 160 mAh $g^{-1}$) comparable to various state of the art materials for LIBs (intercalation cathodes in mAh $g^{-1}$, $LiMn_2O_4$: 120 mAh $g^{-1}$, and $LiFePO_4$: 165 mAh $g^{-1}$ [154-156]). This fluorine insertion most often, but not always, results in an expansion of the lattice along the *c*-axis. For instance, fluorination of $LaSrMnO_4$ leads to an increase in lattice parameter *c* to around ~14.2 Å for the occupation of only one interlayer ($A_2MO_4F$) and 15.5 Å for an ideal full occupation of both anion sites ($A_2MO_4F_2$).[157]

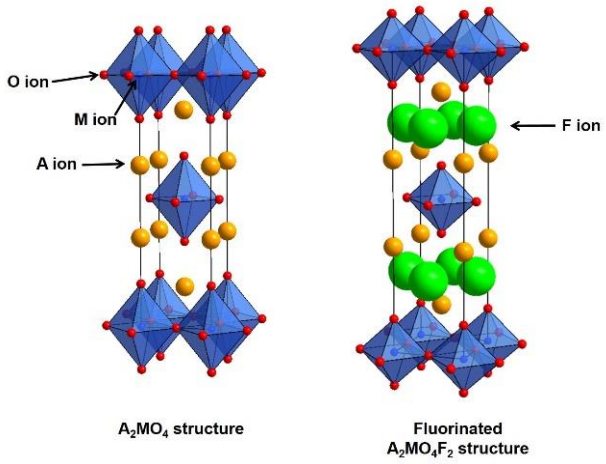


*Figure 16. Schematic illustration of the n = 1 Ruddlesden-Popper ($A_2MO_4$) structure (left) and fully fluorinated $A_2MO_4F_2$ structure (right).*

The reversible electrochemical intercalation and deintercalation of fluoride ions into the Ruddlesden-Popper type compound $LaSrMnO_4$ using a $Pb/PbF_2$ counter electrode (anode) was reported by Nowroozi et al.[96] in 2017. In this work, it has been shown that the structural changes upon electrochemical fluorination are in principle agreement with the results of chemical fluorination experiments of $LaSrMnO_4$[157, 158]: The fluorination process occurs in two steps, in the first step partially fluorinated $LaSrMnO_4F$ with a *c*-parameter of ~14.2 Å forms and in the second step a new phase with an extended *c*-parameter up to ~15.6 Å is obtained which is an indication for formation of the rich-fluoride content phase of $LaSrMnO_4F_{2-\delta}$. The initial structure could be recovered by discharging the cell (electrochemical de-intercalation) to negative potentials (down to – 3.5 V against $PbF_2$). This indicates that for the recovery of initial $LaSrMnO_4$, the overpotentials which were created during the charging step could only be overcome at negative potentials. Such large overpotentials were attributed to the decomposition of the carbon conductive matrix during the charging step.[96] Successful insertion/removal of the fluoride ions into/from the anion interlayers of Ruddlesden-Popper type $LaSrMnO_4$ serves as proof of principle for developing intercalation-based cathodes for FIBs, and meanwhile, reversed cycling at low capacities could be found for higher-order manganates.[138] The need to optimize cycling conditions has been related to the deterioration of the conductivity of the cell as a result of decomposition of the conductive carbon.[96]

Unlike the fluorination of $LaSrMnO_4$, which takes place in a layer-wise manner, the transformation of the Ruddlesden-Popper-type compounds $La_2NiO_{4+d}$ and $La_2CoO_{4+d}$ to $La_2MO_{4+d}F_y$ ($1 \leq y \leq 2$) occurs in only one step, and no stage-ordered fluorinated $La_2MO_{4+d}F_1$ phase could be observed during the charging (electrochemical fluorination) step.[30, 134] For the charged $La_2NiO_{4+d}$ particles, the data obtained from electron diffraction tomography (ADT) suggests that 1.59 to 1.72 fluoride ions can be inserted within the interlayers of a $La_2NiO_{4+d}$ unit cell, which corresponds to a change in the oxidation state of Ni from close to +2 for un-fluorinated particles to almost +4 for the fluorinated particles. This change in the oxidation state of Ni is also confirmed by XANES analysis.[134] In the case of $La_2CoO_{4.16}$, the number of inserted fluoride ions calculated (based on the effective charge capacity) is around 1.2 $F^-$ per formula unit. Furthermore, a separation between the side reaction of the carbon additive and the desired electrochemical redox reaction

can be observed in the charge curves of $La_2CoO_{4+d}$ which has been reported to be in favor controlling the degree of the side reactions taking place.[30]

Based on the extended cycling experiments on $La_2NiO_{4+d}$ and $La_2CoO_{4+d}$, it is reported [30, 134] that the choice of the cutoff criteria (capacity and potential) can significantly influence the cycling stability of cathodes with Ruddlesden-Popper-type structures. For instance, higher charging cutoff capacities such as 120 or 80 mAh $g^{-1}$ would significantly deteriorate the cyclic stability of $La_2NiO_{4+d}$ (as can be seen in Figure 17a), while at a lower cutoff capacity of 50 mAh $g^{-1}$ the cyclic stability becomes much better (~ 60 cycles) and a cycle life of more than 220 cycles with a Coulombic efficiency of close to 100 % is reported for the cutoff capacity of 30 mAh $g^{-1}$ (see Figure 17a). A similar dependency on the cutoff criterion of the cycling behavior has also been observed for $La_2CoO_{4.16}$[30, 137]: The Coulombic efficiency at the first cycle of the $La_2CoO_{4.16}$|Pb+$PbF_2$ cell that was charged up to 65 mAh $g^{-1}$ is calculated to be almost 50 % while it is only ~ 18 % for the cell charged up to 130 mAh $g^{-1}$. The discharge capacity decreases to less than 10 mAh $g^{-1}$ starting from the second cycle for the charge cutoff capacity of 130 mAh $g^{-1}$, showing the severity of the capacity fading for this cell. On the other hand, the discharge capacity for the cell that was initially charged up to 65 mAh $g^{-1}$ was still above 15 mAh $g^{-1}$ after 20 cycles, which is roughly half of the discharge capacity at the first cycle (Figure 17b). The reason for the stability upon limiting the cutoff criteria can be understood as a result of limited oxidation of carbon facilitating the maintenance of electrically conducting interfaces.[134]

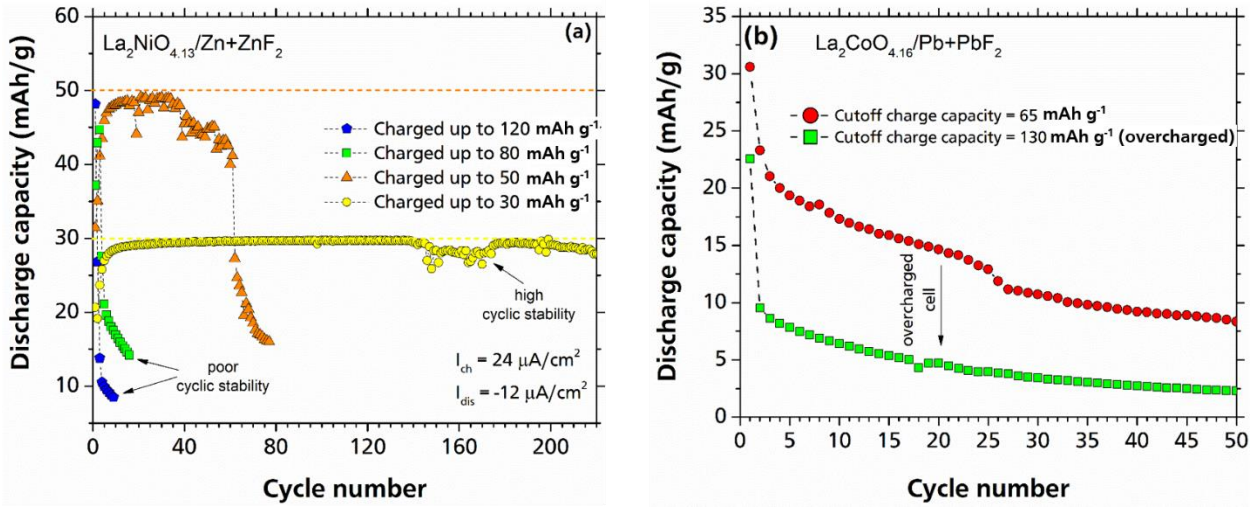


*Figure 17. (a) Cycling stability of the $La_2NiO_{4.13}$|Zn+$ZnF_2$ cell at different cutoff capacities [134]; (b) the effect of overcharging on cycling stability of a $La_2CoO_{4.16}$|Pb+$PbF_2$ cell. All cells were heated at 170 °C and charged/discharged at a current of 24/-12 μA/$cm^2$. Reproduced from ref.[30].*

The effect of the counter electrode (anode material) on the hysteresis potentials have also been found for the $La_2NiO_{4+d}$ intercalation-based system.[134] In fact, by using anode materials with a lower intrinsic volume change during the redox reactions, less overpotentials would be introduced to the $La_2NiO_{4+d}$ system, and therefore the cycling stability of the cell may be improved especially at higher cutoff capacities (Figure 18a). However, such a strategy does not improve the cycling stability of the $La_2CoO_{4.16}$ cathode material. This inconsistency between the effect of the anode material on $La_2NiO_{4+d}$ and $La_2CoO_{4+d}$ may arise from a higher internal resistivity of the $La_2CoO_{4+d}$ composite material, which might originate from some unknown low-potential side reactions.[137]

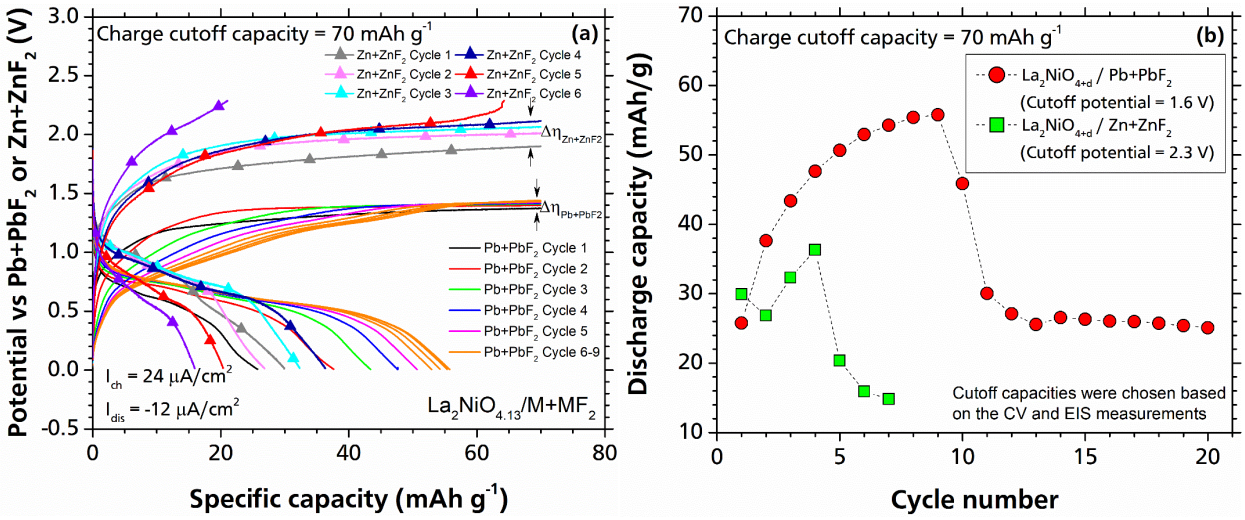


*Figure 18. The effect of anode material on the overpotential and cycling behavior of $La_2NiO_{4.13}$ by showing (a) the first few cycles of $La_2NiO_{4+d}$ against $Zn+ZnF_2$ and $Pb+PbF_2$ anode materials (b) discharge capacities of $La_2NiO_{4+d}$ against $Zn+ZnF_2$ and $Pb+PbF_2$ anode materials. Reproduced with some modifications from ref.[134].*

Electrochemical cycling of the n = 2 Ruddlesden-Popper-type $La_{1.3}Sr_{1.7}Mn_2O_7$ has been performed by Vasala et al.[138] in order to reversibly tune the ferromagnetic properties of the compound. For this, $La_{1.3}Sr_{1.7}Mn_2O_7$ has been charged up to 0.45 or 0.6 V against $Pb+PbF_2$ corresponding to specific capacities of ~15 and ~25 mA/g during the charging step and down to -0.3V during the discharging. Over a span of 10 – 45 cycles, the electrochemical behavior of the cells is very stable without any significant capacity fading during the cycling. Upon cycling, the compound shows a change of the ferromagnetic behavior from strong (defluorinated state) to weak (fluorinated state) ferromagnetism.

Besides Ruddlesden-Popper type oxides, Ruddlesden-Popper-type oxyfluorides $A_{n+1}B_nO_{3n+1-x}F_{2x}\square_{2-x}$ with $x < 2$ were also found to be suitable as intercalation-based cathode materials. Such oxyfluorides can be prepared via low-temperature topochemical fluorination reactions of the respective Ruddlesden-Popper type oxide using fluorine-containing polymers such as polyvinylidene difluoride (PVDF) as fluorination reagent [35, 159-162]. The fluorination takes place via a coupled substitution and intercalation process, in which for each substituted oxide ion, two fluoride ions are intercalated under the maintenance of the oxidation state. When used as active cathode materials for FIBs (the oxyfluoride represents the discharged state), additional fluoride ions are intercalated into these oxyfluorides upon charging. Therefore, anion vacancies □ have to be present after the topochemical fluorination in order to enable oxidative fluorination of these compounds during the electrochemical fluorination. This is, for example, given for non-oxidatively fluorinated $A_2BO_3F_2\square$, derived from an n = 1 Ruddlesden-Popper type oxide $A_2BO_4$.

The topochemical fluorination of $La_2NiO_{4+d}$ using PVDF leads to the formation of $La_2NiO_3F_2\square$.[163] In this compound, only half of the interstitial anion sites are occupied. Thus, additional fluoride intercalation of up to one ion per formula unit is possible, leading to the formation of $La_2NiO_3F_3$ within the charged cathode composite.[35] As for the cycling of cells $La_2NiO_{4+d}|Zn+ZnF_2$, the choice of the cutoff capacity has a significant influence on the cycling stabilities. For cells $La_2NiO_3F_2|Pb+PbF_2$, best performances are found when using a cutoff capacity of 30 mAh $g^{-1}$ (Figure 19). For these cells, comparatively stable cycling can be observed over at least 50 cycles.

However, the Coulombic efficiency is considerably reduced compared to the cells $La_2NiO_{4+d}$|Zn+$ZnF_2$ of the pure oxide compound, even though a steady increase of the efficiency occurs with increasing cycling numbers. In contrast to the high cycling stabilities of the cells $La_2NiO_{4+d}$|Zn+$ZnF_2$, cycling of $La_2NiO_3F_2$ against Zn+$ZnF_2$ leads to an early onset of capacity fading. Further, it was found that apart from the importance of this synthesis route for new battery technologies, such routes can play a vital role for the synthesis of metastable oxyfluoride: a chemical preparation of $La_2NiO_3F_3$ via common topochemical reaction approaches using $F_2$ gas has not been successful.[35, 136] For the electrochemical route, the controllability is obtained by adjusting the potential, whereas the chemical potential of chemical reactants cannot be altered.

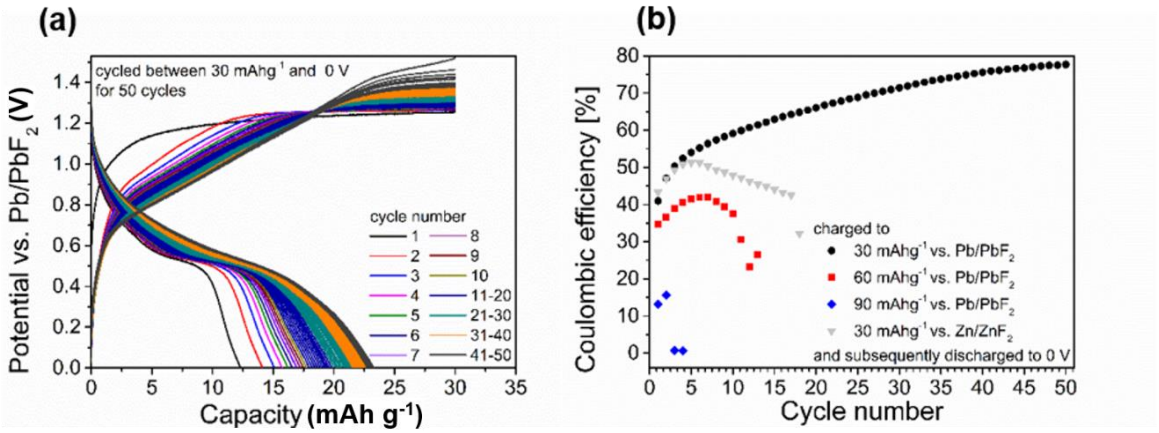


*Figure 19. a) Cycling curves of a cell $La_2NiO_3F_2$ against Pb+$PbF_2$. The cell was cycled between a charging cutoff capacity of 30 mAh $g^{-1}$ and a discharging cutoff potential of 0 V, b) Coulombic efficiencies of cells $La_2NiO_3F_2$ against Pb+$PbF_2$ and $La_2NiO_3F_2$ against Zn+$ZnF_2$ charged to different cutoff capacities. The cells were heated to 170 °C, a current of ~2.5 $mAg^{-1}$ (~ C/25 rate) was applied. Reproduced from ref.[136] with permission[xiv].*

The one-dimensional tunnel structure of Schafarzikite-type compounds with a general composition of $MSb_2O_4$[164] has recently attracted some attentions for the application of intercalation-based electrodes for FIBs.[139, 165] Schafarzikite type compounds possess a tetragonal symmetry (space group $P4_2/mbc$), and the structure can be understood as being built up of chains of edge-linked $MO_6$ octahedra running along the [0 0 1] direction; the chains are connected via trigonal pyramidal $SbO_3$ units (Figure 20). Recent studies have shown that it is possible to fluorinate variants of this material, which contain $Fe^{2+}$ on the M site, via topochemical reactions.[166] This material can thus be of interest for making electrode materials for FIBs because of the mechanism for the inclusion of excess fluoride ions within the channel of the structure (Figure 20). Therefore, it can be considered to be a 1D intercalation material, like olivine type materials for lithium-ion batteries.[167] This is in contrast to the layered ordering of intercalated fluoride ions within Ruddlesden-Popper-type compounds that has been discussed in the previous sections, which are 2D intercalation materials.

Nowroozi et al. reported[139] on the successful electrochemical fluorination/de-fluorination of Schafarzikite-type compounds $(Co/Mn)_{0.5}Fe_{0.5}Sb_2O_4$ at 170 °C. Recently, Zaheer et al. reported [165] on room temperature topochemical fluorination and defluorination of $FeSb_2O_4$ by stirring the Schafarzikite-type and $XeF_2$ within an acetonitrile solution showing the principle of fluoride ion

[xiv] Copyright © 2020 American Chemical Society

insertion/removal in Schafarzikite-type structures at room temperature. Though the Schafarzikite compounds [139] showed poor cycling performance in FIBs using solid electrolytes, this might highlight the potential of these materials to be used in a liquid electrolyte based battery systems at ambient conditions.

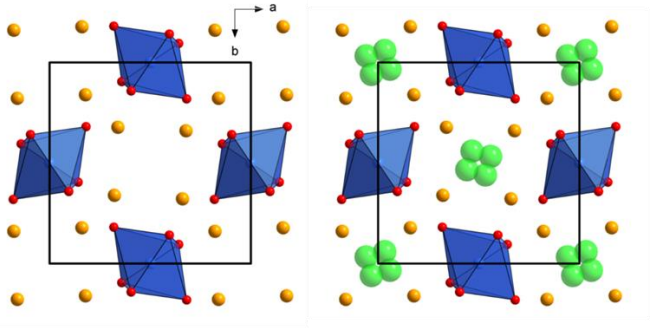


*Figure 20. Schematic presentation of the non-fluorinated $MSb_2O_4$ (left) and fluorinated $MSb_2O_4F_y$ (right) Schafarzikite-type structure. Sb orange, M (Fe, Co) blue, O red, F (partially occupied to ~15 %) green. Reproduced from ref.[139] (open source publication).*

Anion-deficient perovskite-type compounds such as $BaFeO_{2.5}$[140] and $SrFeO_2$[28] have also been investigated as potential intercalation-based cathode materials for FIBs. It is reported that $SrFeO_2$ has insufficient chemical stability towards the other components used in the electrode composite at the applied experimental conditions (T = 170 °C) and the active cathode material undergoes an oxidation reaction resulting in the formation of a compound with high similarity to $SrFeO_2F$. It is not clear how this oxidation takes place and it seems that $SrFeO_2$ can only be stabilized under highly reductive conditions (such as in the presence of excess of $CaH_2$ used during its synthesis).[168]

In another effort by Clemens et al.[28], $BaFeO_{2.5}$ has been investigated against Ce/$CeF_3$ or Mg/$MgF_2$ (conversion-based anode) materials using $La_{0.9}Ba_{0.1}F_{2.9}$ electrolyte (at 150 °C). The cell has been charged up to 4.0 V (vs. $CeF_3$), corresponding to ~ 80 mAh $g^{-1}$, which is slightly larger than the theoretical capacity of $BaFeO_{2.5}$/$BaFeO_{2.5}F_{0.5}$ (57.5 mAh $g^{-1}$). This was claimed to be arising from side reactions. Diffraction experiments revealed that upon the electrochemical fluorination (charging), a decrease in the cell volume per $BaFeX_{3-y}$ unit, down to the range where oxidatively fluorinated compounds are expected, could be observed together with a symmetry change from a vacancy ordered modification to a cubic perovskite. These structural changes upon electrochemical fluorination are in agreement with what was found on fluorinating $BaFeO_{2.5}$ via chemical fluorination using $F_2$ gas. Although the chemical fluorination was successful, only negligible discharge capacities of around 6 mAh $g^{-1}$ could be obtained upon discharging the cell against $CeF_3$[28]

Figure 21 sums up the discharge profiles (after the first charging cycle) of some intercalation-based cathodes that have been discussed in this chapter. The discharge capacity for Ruddlesden-Popper-type $La_2NiO_{4+d}$ appeared to be the highest among all other cathodes: The highest stable discharge capacity that has been so far obtained for an intercalation-based cathode material for FIB was measured to be about 70 mAh $g^{-1}$ (accompanied by a high average discharge potential of ~ 1.2 V) for $La_2NiO_{4+d}$ against a Zn+$ZnF_2$ anode composite material. The discharge capacity for $La_2CoO_{4+d}$ and $LaSrMnO_4$ cathode materials was found to be in a similar range, around 30

mAh $g^{-1}$ (however, $LaSrMnO_4$ provides a higher potential as compared to $La_2CoO_{4+d}$), while $LaSr(Co/Fe)O_4$ cathode materials showed only a poor performance with respect to their discharge capacity (Figure 21). A much poorer performance of the $LaSr(Co/Fe)O_4$ cathode is indicated [28] to result from a structural instability of the active cathode material upon electrochemical fluorination, though these materials might require further elaboration. The lowest discharge capacity is observed for the Schafarzikite-type structure ($Co_{0.5}Fe_{0.5}Sb_2O_4$) around 5 mAh $g^{-1}$, which is in the same capacity range as that of the anion-deficient perovskite structure of $BaFeO_{2.5}$. This comparison reveals the great potential of the Ruddlesden-Popper-type compounds (especially $La_2MO_{4+d}$) as promising intercalation-based cathode materials for FIBs. Furthermore, a high degree of structural reversibility has been observed over a routine discharging process for $La_2NiO_{4.13}$ and $La_2CoO_{4.16}$: After a discharge step, there is no sign of the high fluorine content phase with an extended *c*-parameter (up to ~ 15.2 Å) and the initial $La_2MO_{4+d}$ structure could be recovered.[30, 134]

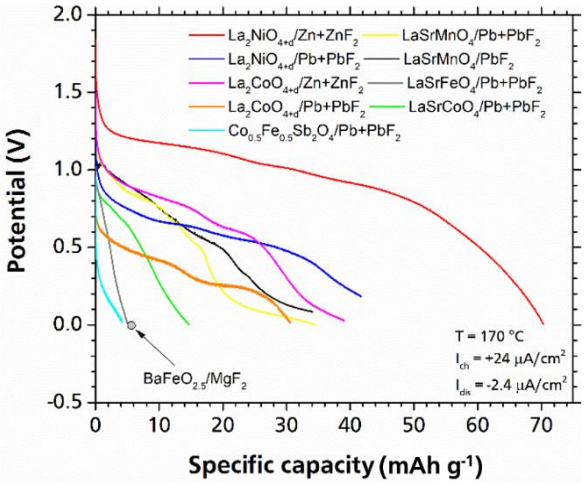


*Figure 21. Discharge profiles of some of the so far proposed intercalation-based cathode materials for FIBs. Reproduced with some modifications from ref.[28].*

## 6.5 Intercalation-based Anode Materials

So far, only a few reports about intercalation-based anode materials exist. A suitable active anode material should be a strong reductant in its charged (defluorinated) state, i.e., the redox-active cation should have an unusually low oxidation state. Thus, the involved redox couple should have a low potential against Li|LiF. As has been described in the previous section, compounds with Ruddlesden-Popper-type structure offer great potential for their use as intercalation-based active cathode materials since the structure shows flexibility towards reversible oxidative intercalation of fluoride ions upon charging and discharging of FIBs. The topochemical modification of Ruddlesden-Popper-type oxides $A_{n+1}B_nO_{3n+1}$ via non-oxidative fluorination reactions, leading to the formation of oxyfluorides $A_{n+1}B_nO_{3n+1-x}F_{2x}\square_{2-x}$ with $x < 2$ offers possibilities for the development of intercalation-based anode materials.[35] Such oxyfluorides represent the discharged states of potential anode materials, while electrochemical charging leads to reductive defluorination reactions. Apart from Ruddlesen-Popper-type compounds, layered electride materials such as $Ca_2N$ or $Y_2C$ and their transformation to the fluorinated states $Ca_2NF$ or $Y_2CF$ were recently

studied by Hartman et al.[169], indicating that these materials could work as high-energy anode materials, if stability towards other battery components can be achieved.

A synthesis process for the chemical low-temperature preparation of the charged states of Ruddlesden-Popper-type anode materials has been recently introduced by Wissel et al.[170] This strongly reductive process allows for an in-depth structure and property analysis of the anode materials in their charged states. It is based on a reaction between the Ruddlesden-Popper-type oxyfluoride and sodium hydride, resulting in selective extraction of fluoride ions from the oxyfluoride. So far, the chemical defluorination behavior of n = 1 $Sr_2TiO_3F_2$, n = 2 $Sr_3Ti_2O_5F_4$ and n = 1 $La_2NiO_3F_2$ has been investigated.[35, 170-172] This defluorination reaction is favoured by the high lattice energy of NaF, which helps to prepare anode materials in the charged state down to a potential of < ~ 1V against Li/LiF.

The feasibility of topochemical modifications of these Ruddlesden-Popper-type oxyfluorides, when used as active anode materials, via electrochemical defluorination reactions in FIBs have also been investigated.[35, 136] A significant redox-activity of the active materials has been only found for the Ni-based compound. Electrochemical charging of cells with a $La_2NiO_3F_2$-containing anode and a Pb+$PbF_2$-based cathode resulted in the formation of a $Ni^+$-containing phase with reduced monoclinic symmetry (space group *C*12/*c*1) and an approximate composition of $La_2NiO_3F_{1.9}$ (i.e., containing 10 % of monovalent Ni species). Changes in the crystal structures due to the successful deintercalation of fluoride ions can be related to the chemically formed reduced phases and are also found for electrochemical reactions (Figure 22).

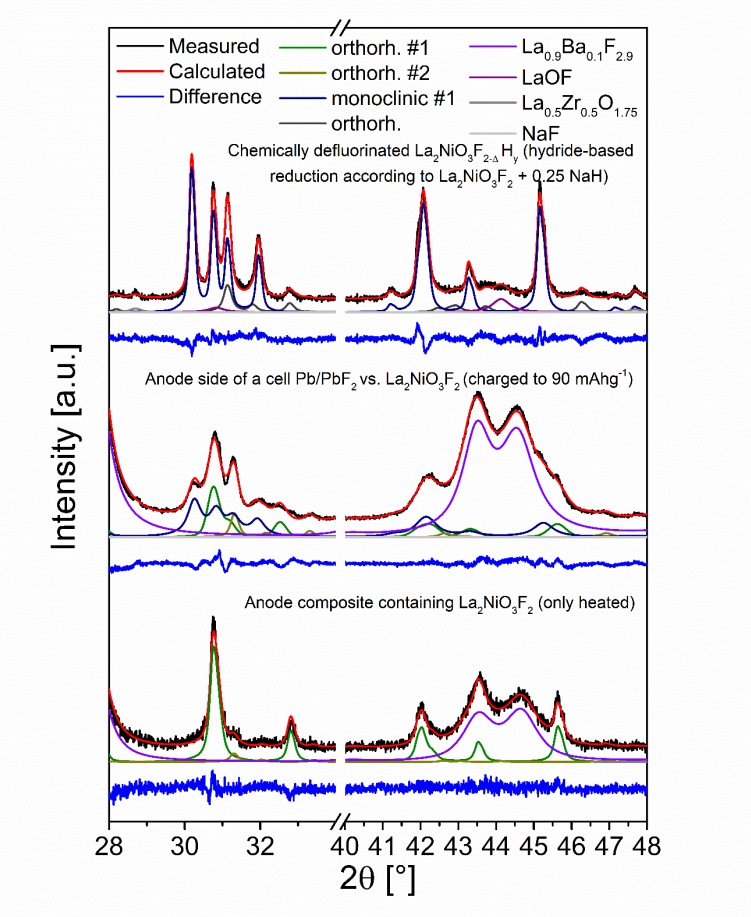


*Figure 22: Comparison of selected angular ranges of XRD patterns of chemically (top) and electrochemically (middle) defluorinated $La_2NiO_3F_{2-x}$. The chemical defluorination was obtained via a hydride-based reduction, the electrochemical defluorination within a FIBs, in which an anode material containing $La_2NiO_3F_2$ was used. In addition, an XRD pattern of the anode composite before electrochemical treatment (bottom) is given, highlighting the change in the reflection patterns of the reduced $La_2NiO_3F_{2-x}$ and the precursor phase $La_2NiO_3F_2$. Reproduced from ref.[136] with permission[xv].*

A typical charging curve of a cell of $Pb+PbF_2$ against $La_2NiO_3F_2$ is given in Figure 23a. A comparison between the theoretical capacity related to the extraction of one fluoride ion from $La_2NiO_3F_2$ to the actually observed capacities illustrates that substantial side reactions are taking place in parallel to the reduction of $La_2NiO_3F_2$ (see also section 6.6) and can be assigned to changes in the carbon matrix. Moreover, large overpotentials and low Coulombic efficiencies have been found (Figure 23b), resulting in negligible reversible capacities on discharging to 0 V. Nevertheless, by discharging to negative potentials, full reversibility of the structural changes has been reported. This is similar to what is reported for $LaSrMnO_4$ in section 6.4.

Overall, a closer examination of the origin and influence of the side reactions, which seem to play a crucial role in the defluorination process, has been found to be very important. This has also become obvious with regards to the unsuccessful electrochemical reduction of the Ti-based compounds[89] (see also section 6.6).

[xv] Copyright © 2020 American Chemical Society

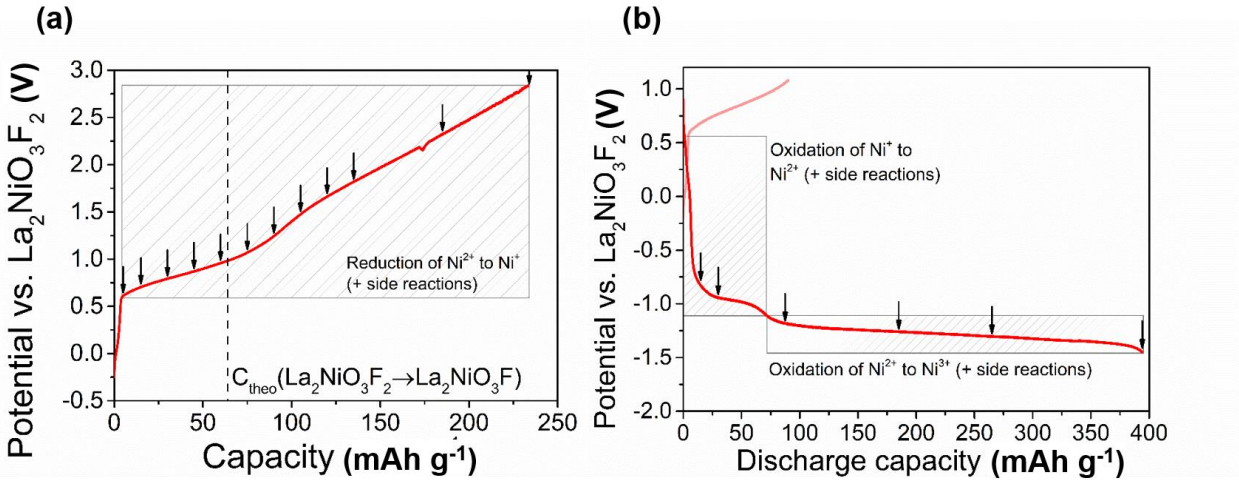


*Figure 23: a) Charging curve of a cell Pb+$PbF_2$ against $La_2NiO_3F_2$, b) Charging and discharging curves of a cell Pb+$PbF_2$ against $La_2NiO_3F_2$. The cell was charged to 90 mAh $g^{-1}$ prior to the discharging. The cells were heated to 170 °C, a current of ~2.5 $mAg^{-1}$ (~ C/25 rate) was applied. Reproduced with some modifications from ref.[136] with permission[xvi].*

## 6.6 The Issue of Carbon Side Reactions for the Application of Electrode Materials

Due to the low electronic conductivity, usually the active electrode materials are mixed with carbon black/carbon nanotubes.[8, 30, 96, 134, 137, 139, 140] The possibility of the occurrence of the carbon side reaction has been reported by different research groups in several studies.[48, 96, 140] Dambournet et al.[48] carried out investigations on possible interactions of carbonaceous additives (as electronic conductor) with the fluoride conducting electrolyte. After the ball milling of the LBF electrolyte and carbon, no indication of the formation of insulating graphite fluorite ($CF_x$) could be determined by NMR. However, according to impedance measurements, the conductivity of the mixed LBF-C composite (produced by ball milling) is lower by one order of magnitude ($5 \times 10^{-8}$ S $cm^{-1}$ at 30 °C) as compared to milled $La_{0.95}Ba_{0.1}F_{2.95}$ ($5.4 \times 10^{-7}$ S $cm^{-1}$ at 30 °C). The authors have further investigated the presence of a reaction of carbon with the LBF electrolyte to yield $CF_x$ by conducting cyclic voltammetry experiments on Li|LBF|LBF-C cells. They showed a rapid increase in the measured current at a potential range between 4.2 – 4.8 V. The standard potential of the electrochemical fluorination reaction of carbon (according to: 1/3 $LaF_3$ + C ⟶ CF + 1/3 La) had been calculated to be 4.19 V which is very close to the contribution to the current behaviour observed in the CV measurements of the LBF-C cell, suggesting that carbon probably undergoes electrochemical fluorination to form $CF_x$.

It was also shown [28] that cyclic voltammograms of a carbon electrode (as the positive electrode) feature an irreversible anodic peak (as can be seen in Figure 24a), which has been attributed to the irreversible oxidation (fluorination; e.g., formation of $CF_x$) of the carbon.[28] Such irreversible anodic peaks can also be observed in the cyclic voltammograms of the $La_2NiO_{4.13}$ cells. However, the peak slightly shifted towards the lower potential range (Figure 24a), which has been explained by a catalytic effect of the active cathode material towards the carbon side reaction.[134] Interestingly, reversible cathodic peaks corresponding to the de-fluorination of $La_2NiO_{4.13}F_x$ in the cathode composite material can only be observed upon limiting the cycling voltage range below

[xvi] Copyright © 2020 American Chemical Society

the range for the occurrence of the irreversible anodic peaks (Figure 24b), suggesting that oxidation reactions of C within the cathode composite result in electrochemical irreversibility of the cell.[134] Other characterization methods also support the oxidation of carbon during the charging step within the $La_2MO_{4+d}$ systems. For instance, XPS measurements confirm an increase in the oxidation state of carbon within the $La_2NiO_{4+d}$ systems during the charge step. Further, electrochemical impedance measurements show a rapid change in the impedance behavior of the $La_2NiO_{4+d}$ cells from a Warburg-type behavior (indicative for electrochemical reactions) to a capacitive behavior, which is indicative for a blocking effect. This rapid change occurs within the region in which the irreversible cathodic reactions are seen within the cyclic voltammograms of $La_2NiO_{4+d}$ cathode material. Moreover, electrochemical impedance spectroscopy (EIS) measurements reveal a sharp increase in resistivity of the cells after ~ 60 mAh $g^{-1}$ in the $La_2CoO_{4+d}$ systems, which is explained as a significant deterioration in the conductivity of the cell due to carbon oxidation.[30, 137]

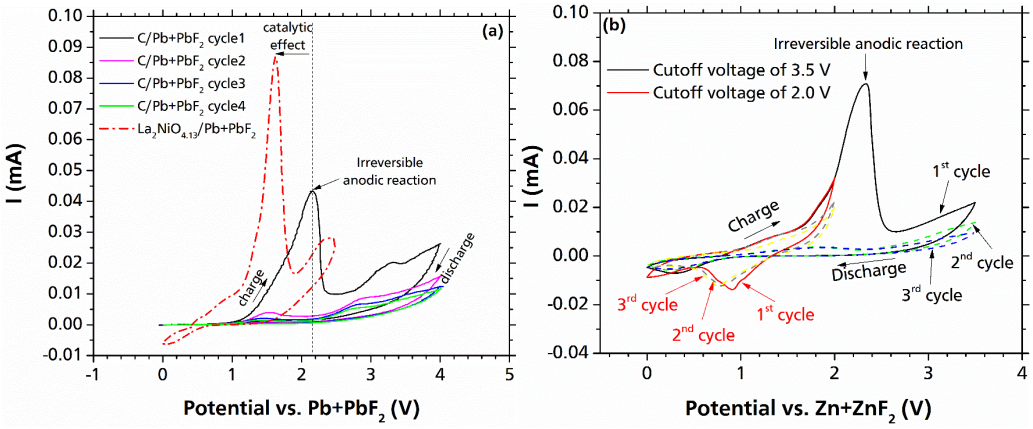


*Figure 24. Cyclic voltammorgarms of a carbon electrode as compared to $La_2NiO_{4+d}$ cathode material ($Pb+PbF_2$ as counter electrode); (b) Cyclic voltammograms of $La_2NiO_{4+d}$ cathode material vs. $Zn+ZnF_2$ in two different potential range of 0 – 2 V and 0 – 3.5 V. Figures are reproduced with some modifications from ref.[28].*

On the anode side, there has also been an indication for the occurrence of side reactions in the form of a carbon reduction. The detailed nature of this reaction is yet to be understood and could involve the release of surface-adsorbed oxygen or a reaction of carbon with La or Ba of the electrolyte LBF (according to $C + x\ LaF_3 \rightarrow CLa_x + 3F^-$).[35] Cyclic voltammetry measurements showed that these irreversible side reactions take place largely in parallel with the desired reactions during the charging of the $La_2NiO_3F_2$-based anode composites. XPS measurement revealed, furthermore, that the carbon additive is reduced during this process. The carbon reduction and the associated destruction of the electronically conductive matrix within the electrode material also provides an explanation of why $Sr_2TiO_3F_2$ and $Sr_3Ti_2O_5F_4$ could not be defluorinated electrochemically when used as anode material. Due to the low potential of $Ti^{3+}|Ti^{4+}$, the carbon reduction sets in at much higher potentials compared to the desired reduction of the Ti-based compound. This impairs a reduction of the Ti-based compounds.

While the reaction of carbon within the FIB cells is often considered to be a side reaction [27, 30, 134] affecting the conductivity of the cell, fluorine-intercalated graphite has recently been proposed [173] as a cathode material (positive electrode) for FIBs. In this study, the active cathode material of $C_xF$ has been made in a charged state by the reaction of graphite powder and fluorine gas in

anhydrous HF at room temperature to form $C_{2.8}F$. The full cell was built up using $PbSnF_4$ as the electrolyte and a Pb plate as the anode material. To increase the discharge capacity, the active cathode material was mixed with $CuF_2$. The highest discharge capacity of 230 mAh $g^{-1}$ with a voltage plateau of 0.6 – 0.55 V is reported for the cathode composite with a $CuF_2$ weight fraction of 80 %. The obtained capacity lies around half of the theoretical capacity of $C_{2.8}F$ (521 mAh $g^{-1}$). However, since the active carbon cathode is mixed with $CuF_2$, it is not clear if all the obtained capacity is arising from the defluorination of carbon or a contribution of the $CuF_2$ to the Cu conversion-type reaction exists, which could also be responsible for some fraction of the discharge capacity.

## 7 Conclusions and Future Challenges

In this review, the improvements of FIBs from the early 1970s until today have been discussed with respect to the development of the electrolytes as well as cathode and anode materials.

In contrast to LIBs, the first cells suggested for FIBs relied on the use of solid fluoride ion conductors due to the difficulty of transporting a “naked” fluoride ion in liquid conditions. The respective doped binary fluorides are easy to make and commercially available but have limited conductivities at room temperature and thus require heating to ~ 150 °C or above in order to be charged/discharged with reasonable C-rates. Therefore, in the future, a critical focus must be based on the development of RT-FIB systems with either solid or liquid electrolytes, which could make the technology a real alternative to the current commercial batteries, especially for localized storage applications.

In particular, since less attention has been paid to develop FIBs based on liquid electrolytes, their further elaboration and determination of compatibility with various electrode materials can play an important future role in making efficient cells. In this subfield, it will be important to stabilize a weakly coordinated fluoride species, while maintaining high compatibility towards the electrode materials as well as additives in the cell. Especially for carbon-based additives, their interaction with liquids is known to be complex, and needs to be studied in detail for the different materials to be developed, conversion- and intercalation-based systems, thus providing a large exploitation space. Further, safety aspects have not discussed for liquid electrolytes to any extent, and it is not clear if dendritic growth of the electrode materials (which could in principle account for both, cathode and anode, if conversion-based systems are being used) can occur for specific elements and/or at increased C-rates. In addition, we would like to acknowledge that the use of liquid electrolytes could result in the preparation of new oxyfluoride materials with exciting magnetic or electronic properties via topochemical methods; since such oxyfluorides are metastable most frequently, reduction of synthesis temperature might be achievable within such battery cells.

A big advantage of solid ion conductors lies in a maximal transport number for a certain ionic species approaching a value of t ~ 1, which can facilitate high C-rates. For LIBs, it is considered that this can prevent certain polarization issues arising at high current densities,[22] and it is valid to assume similar behavior for FIBs. However, due to the intrinsically lower ionic conductivity of FIBs, the breakthrough of solid ion conductors can be measured primarily by the challenges of operating temperature and cell preparation before the consideration of high-performance issues should take place. The operating temperature can, in principle, be matched by few materials containing $ns^2$ cations ($PbSnF_4$ has the highest conductivity of around $10^{-3}$ $S \cdot cm^{-1}$ at room temperature until present), which show a lower electrochemical stability window. Again, this gives some similarity to solid lithium-ion conductors, such as thiophosphate based compounds, which have high conductivities, but low electrochemical stability.[174] Potentially, such instabilities could be circumvented in future by applying coating to electrode materials or using interlayer approaches. Clearly, the design strategies cannot be adopted one by one, but a certain similarity might also account here. Stabilization of the cathode side towards the solid electrolyte might be easier to be achieved, since known solid ion conductors such as $La_{0.9}Ba_{0.1}F_{2.9}$, which would have sufficient conductivity to be applied as a coating, have high stability towards oxidizing reactions. In contrast, metals with low electronegativity such as Mg or Ce used on the anode side will be more difficult to be stabilized by coating since they perform conversion reactions with large volume

changes and have similar redox potentials than $La_{0.9}Ba_{0.1}F_{2.9}$, which might imply a certain cross-reactivity. Lower redox potentials and thus higher stability towards anode materials would be expected for alkaline fluorides AF (A = Li, Na, K) as a coating, but these materials are bad fluoride ion conductors and would rather be expected to be conductive for the $A^+$ cations at least partially. Thus, explorative work is required in order to find strategies to stabilize such coatings against electropositive metals while avoiding blocking of transport pathways to the highest extent possible. Regardless of the work that has to be done in the future, the authors of this review assume that solid electrolytes will still be of importance for the development of other cell components such as electrode materials within the upcoming years in any case. Thus, it can be expected that many reports will be based on the development of solid-state FIB concepts. In this context, also novel solid conductors should be explored, e. g., by using weakly charged cage molecules, such as boranes, as cationic counterparts to fluoride ions, a concept which also proved successful for sodium ion conductors.[175]

Cell preparation is another important aspect of FIBs. Fluorides have in general lower melting temperatures than oxide materials and thus can show easier thermal handling in order to minimize grain boundary resistances. Other methods such as cold sintering or spark plasma sintering might bring into play new aspects for the preparation of ceramic conductors, which have been basically unexplored. Further, though some reports have considered the use of thin films, the exploration space provided in this field is large, with aspects such as the exploration of multilayers (where interlayers could act as protective coatings), interface studies, thin-film batteries, strain engineering, etc., deserving future focus. Especially for the use of 1D or 2D intercalation-based materials, the use of epitaxially grown materials or the introduction of strong texturing into polycrystalline films could facilitate the use of larger C-rates, required for bringing the method closer to application.

Another point to be considered for future applications lies in the fact that rare earth fluoride conductors present challenges in terms of weight and material costs (for example, La, Ce, Sr). These materials neither possess a large availability for large scale applications nor a strong interest for applications such as electromobility. Though alkaline earth or lanthanide fluorides possess good stability against humidity and do not release HF easily (e. g., $LaF_3$ can be precipitated from aqueous solutions), certain alkali metal fluorides are more sensitive to humidity and acidic conditions especially, and can release corrosive HF gas; therefore, replacement with lower weight cations might come at the cost of safety and must be assessed critically. Further, elements such as Pb and Sb imply certain environmental concerns, and would be desirable to be replaced or limited in use for real applications.

The authors also would like to emphasize that solid-state batteries are in general less understood than the liquid electrolyte-based counterparts and that research performed in this context can lead to co-operative effects in creating a deeper understanding of the matter for LIBs.

Recent developments of the electrode materials (both cathodes and anodes) for FIBs were discussed in the context of intercalation and conversion mechanisms. It is shown that conversion-based systems mainly provide large capacities, though, they often suffer from poor cycling stability. Therefore, the highest cycle life has been so far observed for intercalation-based cathode materials with Ruddlesden-Popper-type structure. It is worth mentioning that to overcome intrinsic problems with conversion-based electrode materials, several strategies have been derived for

lithium-ion batteries, which might be conceptually adaptable to improve conversion-based electrodes for FIBs within future research directions. These strategies comprise the preparation of cells in thin electrode configurations,[1] encapsulation of the electrode material in a hollow structure,[176, 177] or the infiltration of materials into porous carbon hosts.[178] Nevertheless, considering the limitations of the conversion- based electrode materials, even the state of the art of the LIBs still mainly relies on intercalation-based electrode materials. Thus, the solution to the problem of obtaining functional intercalation-based materials might not necessarily be fully chemistry-related, but also include materials science and engineering aspects, such as the application of pressure during cycling, or the exploration of suitable binders even for all solid state cells. In contrast, a chemical approach for improving conversion materials might be in finding suitable combination of various fluorides within multinary materials, e.g., within high-entropy fluorides (high-entropy oxides were recently found to show improved reversibility as conversion-based electrodes for LIBs[179]). Therefore, by such further improvement and exploration of the conversion-based electrode materials, they may enter into the market of reversible batteries, especially due to their high energy capacity required for large scale energy storage,[40] in case the problem of long-term operation can be reasonably addressed.

With respect to intercalation-based systems, there is still a wide space for exploration, especially for anode materials, where the concept of oxide for fluoride substitution and subsequent reductive fluoride extraction could be adopted to metal cations such as $Sn^{4+}$, $In^{3+}$, $Ru^{6+}$, etc. to stabilize them in more reductive, lower oxidation states, or by exploring electrides as suggested recently.[169] However, also the field of layered oxides for lithium-ion batteries was not pushed forwards by using other materials, but by developing doped (e. g., redox-inert cations such as $Al^{3+}$) or substituted/multinary (e. g., Co for Ni and Mn) isostructural compounds, which gave a boost of stability as well as intrinsic conductivity at the same time, and is yet to be explored for FIBs. For intercalation materials, another issue lies in the replacement of heavy alkaline earths or lanthanides, such as Sr, Ba, or La by lower weight and higher abundant cations such as Ca or Sc for Ruddlesden-Popper based systems, which would help to increase the specific capacity strongly, since the redox-inert cations contribute to the weight of the active material upto ~ 75 %. In addition, topochemical reactions based on anions are not limited to Ruddlesden-Popper type compounds, but can also occur for other perovskite related materials, which use would decrease the amount of redox-inert cations per redox-active cation.[180] Alternatively, a lighter matrix could also be achieved by using fluoride in combination with polyanions such as phosphate or sulphate, by which the stabilization of the host matrix might occur via the polyanion instead of the alkaline / rare earth metals. In this respect, one must succeed in adopting topochemical fluorination routes away from perovskite-related systems[160] to other structural settings. In the other hand, the issues related to the carbon side reaction need to be further investigated, and techniques to mitigate the negative effect of carbon degradation should be developed; this can imply the use of different kinds of carbon materials (e.g., multi-wall carbon nanotubes), or suitable nanostructures of conductive redox-stable oxides. In this context, materials engineering can be highly important, where contact points between the different cell components might be optimized by using nano-rod morphologies, particle coating strategies and core-shell structures, or by using thin films.

Although commercial application of FIBs lies in the far future, it is worth to think on how the materials discussed here could be exploited for large-scale fabrication processes. For oxide materials used as cathode materials for LIBs in combination with liquid electrolytes, various

procedures exist for the preparation of electrode coatings, which require the formation of slurries as starting point. Such slurries are made from a dispersant, binder, conductive additive and the active material itself. For intercalation-based oxide materials for FIBs, such procedures might be easily transferable; in contrast, preparation strategies might have to change drastically when moving to conversion based-materials, e. g., metal fluorides, which can be expected to have different interactions with dispersants, and will thus require solution strategies of material engineers. On the other hand, for fully conversion-based batteries, fabrication processes can be expected to be similar, potentially simplifying the overall process.

Though many improvements were made over the last years, FIBs are still at an early stage of development; their performance is not yet close to the state-of-the-art LIBs, but they can approach other alternative battery technologies such as chloride, magnesium or aluminum ion batteries. For certain applications, the development of room temperature solid-state and liquid electrolytes is an obligation in order to attract more interest in FIBs. However, high-temperature batteries might still fill a niche for certain applications,[181] might not be as critical considering electromobility (where the so-called ZEBRA battery has been used already[182]), and might be unproblematic for large scale energy storage, for which the energy losses can be minimized using well-engineered thermal insulation.

## Acknowledgments

O. Clemens, K. Wissel and A. Nowroozi acknowledge funding from the German Research Foundation within CL551/2-1

### References

1. N. Nitta, F. Wu, J. T. Lee and G. Yushin, *Mater. Today*, 2015, **18**, 252-264.
2. M. Sawicki and L. L. Shaw, *RSC Adv.*, 2015, **5**, 53129-53154.
3. J. W. Choi and D. Aurbach, *Nat. Rev. Mater*, 2016, **1**, 16013.
4. Y. Shao, M. Gu, X. Li, Z. Nie, P. Zuo, G. Li, T. Liu, J. Xiao, Y. Cheng, C. Wang, J. G. Zhang and J. Liu, *Nano Lett.*, 2014, **14**, 255-260.
5. A. M. Melemed, A. Khurram and B. M. Gallant, *Batteries & Supercaps*, 2020, **3**, 570-580.
6. H. Jiao, C. Wang, J. Tu, D. Tian and S. Jiao, *Chem. Commun.*, 2017, **53**, 2331-2334.
7. X. Zhao, S. Ren, M. Bruns and M. Fichtner, *J. Power Sources*, 2014, **245**, 706-711.
8. M. Anji Reddy and M. Fichtner, *J. Mater. Chem.*, 2011, **21**, 17059-17062.
9. D. R. Lide, *CRC Handbook of Chemistry and Physics* CRC Press, Boca Raton, FL, Internet Version 2005 edn., 2005.
10. List of Occurrences, http://www.mindat.org/min-1576.html, (accessed 09.07.2019, 2019).
11. F. Gschwind, H. Euchner and G. Rodriguez-Garcia, *Eur. J. Inorg. Chem.*, 2017, **2017**, 2784-2799.
12. W. Baukal, *Electrochim. Acta*, 1974, **19**, 687-694.
13. J. H. Kennedy and R. C. Miles, *J. Electrochem. Soc.*, 1976, **123**, 47-51.
14. J. H. Kennedy and J. C. Hunter, *J. Electrochem. Soc.*, 1976, **123**, 10-14.
15. J. Schoonman, *J. Electrochem. Soc.*, 1976, **123**, 1772-1775.
16. Y. Danto, G. Poujade, J. D.Pistré, C. Lucat and J. Salardenne, *Thin Solid Films*, 1978, **55**, 347-354.
17. J. Schoonman, K. E. D. Wapenaar, G. Oversluizen and G. J. Dirksen, *J. Electrochem. Soc.*, 1979, **126**, 709-713.
18. J. Schoonman and A. Wolfert, *J. Electrochem. Soc.*, 1981, **128**, 1522–1523.
19. J. Schoonman and A. Wolfert, *Solid State Ionics*, 1981, **3-4**, 373-379.

20. R. Shannon, *Acta Crystallogr. A*, 1976, **32**, 751-767.
21. R. Murugan, V. Thangadurai and W. Weppner, 2007, **46**, 7778-7781.
22. B. V. Lotsch and J. Maier, *J. Electroceram.*, 2017, **38**, 128-141.
23. A. Hayashi, K. Noi, A. Sakuda and M. Tatsumisago, *Nature Communications*, 2012, **3**, 856.
24. C. Rongeat, M. A. Reddy, T. Diemant, R. J. Behm and M. Fichtner, *J. Mater. Chem. A*, 2014, **2**, 20861-20872.
25. H. Konishi, A. C. Kucuk, T. Minato, T. Abe and Z. Ogumi, *J. Electroanal. Chem. Interfacial Electrochem.*, 2019, **839**, 173-176.
26. A. Düvel, P. Heitjans, P. Fedorov, G. Scholz, G. Cibin, A. V. Chadwick, D. M. Pickup, S. Ramos, L. W. L. Sayle, E. K. L. Sayle, T. X. T. Sayle and D. C. Sayle, *J. Am. Chem. Soc.*, 2017, **139**, 5842-5848.
27. A. Grenier, A. G. Porras-Gutierrez, M. Body, C. Legein, F. Chrétien, E. Raymundo-Piñero, M. Dollé, H. Groult and D. Dambournet, *J. Phys. Chem. C*, 2017, **121**, 24962-24970.
28. M. A. Nowroozi, Ph.D., Technische Universität Darmstadt, 2020, DOI: 10.25534/tuprints-00011523.
29. L. Zhang, Ph.D., Helmholtz Institute Ulm, 2016, DOI: 10.18725/OPARU-4272.
30. M. A. Nowroozi, S. Ivlev, J. Rohrer and O. Clemens, *J. Mater. Chem. A*, 2018, **6**, 4658-4669.
31. L. Zhang, M. A. Reddy and M. Fichtner, *J. Solid State Electrochem.*, 2018, **22**, 997–1006.
32. A. Grenier, A. G. Porras Gutierrez, H. Groult and D. Dambournet, *J. Fluor. Chem.*, 2016, **191**, 23-28.
33. F. Gschwind, Z. Zao-Karger and M. Fichtner, *J. Mater. Chem. A*, 2014, **2**, 1214-1218.
34. V. K. Davis, C. M. Bates, K. Omichi, B. M. Savoie, N. Momcilovic, Q. Xu, W. J. Wolf, M. A. Webb, K. J. Billings, N. H. Chou, S. Alayoglu, R. K. McKenney, I. M. Darolles, N. G. Nair, A. Hightower, D. Rosenberg, M. Ahmed, C. J. Brooks, T. F. Miller, 3rd, R. H. Grubbs and S. C. Jones, *Science*, 2018, **362**, 1144-1148.
35. K. Wissel, Ph.D., Technische Universität Darmstadt, 2020, DOI: 10.25534/tuprints-00013383.
36. L. Zhang, M. Anji Reddy and M. Fichtner, *Solid State Ionics*, 2015, **272**, 39-44.
37. C. Rongeat, M. A. Reddy, R. Witter and M. Fichtner, *ACS Appl. Mater. Interfaces*, 2014, **6**, 2103-2110.
38. S. Breuer, M. Gombotz, V. Pregartner, I. Hanzu and M. Wilkening, *Energy Storage Materials*, 2019, **16**, 481-490.
39. B. P. Sobolev, A. M. Golubev and P. Herrero, *Crystallogr. Rep.*, 2003, **48**, 141-161.
40. F. Gschwind, G. Rodriguez-Garcia, D. J. S. Sandbeck, A. Gross, M. Weil, M. Fichtner and N. Hörmann, *J. Fluorine Chem.*, 2016, **182**, 76-90.
41. K. Motohashi, T. Nakamura, Y. Kimura, Y. Uchimoto and K. Amezawa, *Solid State Ionics*, 2019, **338**, 113-120.
42. M. Wilkening, A. Düvel, F. Preishuber-Pflügl, K. da Silva, S. Breuer, V. Šepelák and P. Heitjans, *Z. Krist. - Cryst. Mater.*, 2017, **232**.
43. H. Bhatia, D. T. Thieu, A. H. Pohl, V. S. K. Chakravadhanula, M. H. Fawey, C. Kubel and M. Fichtner, *ACS Appl. Mater. Interfaces*, 2017, **9**, 23707-23715.
44. J. Chable, A. G. Martin, A. Bourdin, M. Body, C. Legein, A. Jouanneaux, M. P. Crosnier-Lopez, C. Galven, B. Dieudonné, M. Leblanc, A. Demourgues and V. Maisonneuve, *J. Alloys Compd.*, 2017, **692**, 980-988.
45. A. Roos, F. C. M. v. d. Pol, R. Keim and J. Schoonman, *Solid State Ionics*, 1984, **13**, 91-203.
46. J. Chable, B. Dieudonne, M. Body, C. Legein, M. P. Crosnier-Lopez, C. Galven, F. Mauvy, E. Durand, S. Fourcade, D. Sheptyakov, M. Leblanc, V. Maisonneuve and A. Demourgues, *Dalton Trans.*, 2015, **44**, 19625-19635.

47. L. Zhang, M. Anji Reddy, P. Gao and M. Fichtner, *J. Alloys Compd.*, 2016, **684**, 733-738.
48. B. Dieudonné, J. Chable, M. Body, C. Legein, E. Durand, F. Mauvy, S. Fourcade, M. Leblanc, V. Maisonneuve and A. Demourgues, *Dalton Trans.*, 2017, **46**, 3761-3769.
49. B. Dieudonné, J. Chable, F. Mauvy, S. Fourcade, E. Durand, E. Lebraud, M. Leblanc, C. Legein, M. Body, V. Maisonneuve and A. Demourgues, *J. Phys. Chem. C*, 2015, **119**, 25170-25179.
50. P. Molaiyan and R. Witter, *Mater. Lett.*, 2019, **244**, 22-26.
51. B. Ruprecht, M. Wilkening, S. Steuernagel and P. Heitjans, *J. Mater. Chem.*, 2008, **18**.
52. M. Heise, G. Scholz, A. Düvel, P. Heitjans and E. Kemnitz, *Solid State Sci.*, 2016, **60**, 65-74.
53. N. I. Sorokin, E. A. Krivandina, Z. I. Zhmurova, B. P. Sobolev, M. V. Fominykh and V. V. Fistul', *Phys. Solid State*, 1999, **41**, 573-575.
54. R. Witter, M. Roming, C. Feldmann and A. S. Ulrich, *J. Colloid Interface Sci.*, 2013, **390**, 250-257.
55. B. P. Sobolev, I. A. Sviridov, V. I. Fadeeva, S. N. Sul'yanov, N. I. Sorokin, Z. I. Zhmurova, P. Herrero, A. Landa-Canovas and R. M. Rojas, *Crystallogr. Rep.*, 2005, **50**, 478-485.
56. F. Preishuber-Pflugl, P. Bottke, V. Pregartner, B. Bitschnau and M. Wilkening, *Phys. Chem. Chem. Phys.*, 2014, **16**, 9580-9590.
57. A. Düvel, J. Bednarcik, V. Šepelák and P. Heitjans, *J. Phys. Chem. C*, 2014, **118**, 7117-7129.
58. C. Rongeat, M. A. Reddy, R. Witter and M. Fichtner, *J. Phys. Chem. C*, 2013, **117**, 4943-4950.
59. S. Chaudhuri, F. Wang and C. P. Grey, *J. Am. Chem. Soc.*, 2002, **124**, 11746-11757.
60. F. Preishuber-Pflügl, V. Epp, S. Nakhal, M. Lerch and M. Wilkening, *Phys. Status Solidi C*, 2015, **12**, 10-14.
61. N. I. Sorokin, *Inorg. Mater.*, 2004, **40**, 989-997.
62. P. Ravindran, R. Vidya, A. Kjekshus, H. Fjellvåg and O. Eriksson, *Phys. Rev. B*, 2006, **74**, 224412.
63. O. Clemens, R. Kruk, E. A. Patterson, C. Loho, C. Reitz, A. J. Wright, K. S. Knight, H. Hahn and P. R. Slater, *Inorg. Chem.*, 2014, **53**, 12572-12583.
64. M. M. Ahmad, Y. Yamane and K. Yamada, *Journal of Applied Physics*, 2009, **106**, 074106.
65. I. Mohammad, R. Witter, M. Fichtner and M. A. Reddy, *ACS Appl. Energy Mater.*, 2018, **1**, 4766-4775.
66. I. Mohammad, PhD, TALLINN UNIVERSITY OF TECHNOLOGY, 2019, DOI: doi.org/10.23658/TALTECH.27/2019.
67. I. Mohammad, R. Witter, M. Fichtner and M. A. Reddy, *ACS Appl. Energy Mater.*, 2019, **2**, 1553-1562.
68. I. Mohammad, J. Chable, R. Witter, M. Fichtner and M. A. Reddy, *ACS Appl. Mater. Interfaces*, 2018, **10**, 17249-17256.
69. E. Murray, D. F. Brougham, J. Stankovic and I. Abrahams, *J. Phys. Chem. C*, 2008, **112**, 5672-5678.
70. V. Y. Kavun, A. I. Ryabov, I. A. Telin, A. B. Podgorbunskii, S. L. Sinebryukhov, S. V. Gnedenkov and V. K. Goncharuk, *J. Struct. Chem.*, 2012, **53**, 290-294.
71. M. Murakami, Y. Morita and M. Mizuno, *J. Phys. Chem. C*, 2017, **121**, 2627-2634.
72. V. Trnovcová, P. P. Fedorov and I. Furár, *Russ. J. Electrochem.*, 2009, **45**, 630-639.
73. M. Heise, G. Scholz, A. Düvel, P. Heitjans and E. Kemnitz, *Solid State Sci.*, 2018, **77**, 45-53.
74. P. A. Popov, A. A. Sidorov, E. A. Kul'chenkov, A. M. Anishchenko, I. C. Avetissov, N. I. Sorokin and P. P. Fedorov, *Ionics*, 2017, **23**, 233-239.
75. V. Trnovcova, P. P. Fedorov, Buchinskaya, II, V. Smatko and F. Hanic, *Solid State Ionics*, 1999, **119**, 181-189.

76. P. Molaiyan and R. Witter, *J. Electroanal. Chem.*, 2019, **845**, 154-159.
77. M. Murakami, Y. Morita, M. Yonemura, K. Shimoda, M. Mori, Y. Koyama, T. Kawaguchi, K. Fukuda, Y. Ishikawa, T. Kamiyama, Y. Uchimoto and Z. Ogumi, *Chem. Mater.*, 2019, **31**, 7704-7710.
78. A. M. Melemed and B. M. Gallant, *J. Electrochem. Soc.*, 2020, **167**.
79. Y. Saito and J. Maier, *J. Electrochem. Soc.*, 1995, **142**, 3078-3083.
80. P. Molaiyan and R. Witter, *Mat Design Process Comm.*, 2019, **1**, e44.
81. S. Breuer and M. Wilkening, *Dalton Trans.*, 2018, **47**, 4105-4117.
82. A. M. Ibraheem, M. A. H. Khalafalla and M. H. Eisa, *Eur. Phys. J. B*, 2017, **90**, 42.
83. P. Jain, S. Kim, R. E. Youngman and S. Sen, *J. Phys. Chem. Lett.*, 2010, **1**, 1126-1129.
84. P. Molaiyan, Ph.D., TALLINN UNIVERSITY OF TECHNOLOGY, 2020, DOI: 10.23658/taltech.4/2020.
85. N. I. S. B.P. Sobolev, N.B. Bolotina, in *Photonic and Electronic Properties of Fluoride Materials*, ed. K. P. Alain Tressaud, Elsevier, 1st edn., 2016, DOI: 10.1016/B978-0-12-801639-8.00021-0, pp. 465-491.
86. G. Scholz, I. Dörfel, D. Heidemann, M. Feist and R. Stösser, *J. Solid State Chem.*, 2006, **179**, 1119-1128.
87. V. Trnovcová, P. P. Fedorov and I. Furár, *J. Rare Earths*, 2008, **26**, 225-232.
88. G. George, J. I. Hayes, C. N. Collins, J. E. Davis, L. Yu, Y. Lin, J. Wen, D. Ila and Z. Luo, *J. Alloys Compd.*, 2020, DOI: 10.1016/j.jallcom.2020.157591.
89. L. N. Patro, *J. Solid State Electrochem.*, 2020, **24**, 2219-2232.
90. G. Scholz, K. Meyer, A. Duvel, P. Heitjans and E. Kemnitz, *Z. Anorg. Allg. Chem.*, 2013, **639**, 960-966.
91. G. Scholz, S. Breitfeld, T. Krahl, A. Düvel, P. Heitjans and E. Kemnitz, *Solid State Sci.*, 2015, **50**, 32-41.
92. A. Duvel, M. Wilkening, R. Uecker, S. Wegner, V. Sepelak and P. Heitjans, *Phys. Chem. Chem. Phys.*, 2010, **12**, 11251-11262.
93. A. Duvel, L. M. Morgan, G. Cibin, D. Pickup, A. V. Chadwick, P. Heitjans and D. C. Sayle, *J Phys Chem Lett*, 2018, **9**, 5121-5124.
94. C. Rongeat, M. A. Reddy, R. Witter and M. Fichtner, *ACS Appl Mater Interfaces*, 2014, **6**, 2103-2110.
95. C. Suryanarayana, *Research (Wash D C)*, 2019, **2019**, 4219812.
96. M. A. Nowroozi, K. Wissel, J. Rohrer, A. R. Munnangi and O. Clemens, *Chem. Mater.*, 2017, **29**, 3441-3453.
97. J. T. S. Irvine, C. S. Derek and A. R. West, *Adv. Mater.*, 1990, **2**, 132-138.
98. M. R. Lukatskaya, B. Dunn and Y. Gogotsi, *Nat Commun*, 2016, **7**, 12647.
99. L. N. Patro and K. Hariharan, *Solid State Ionics*, 2013, **239**, 41-49.
100. L. Liu, L. Yang, M. Liu, X. Y. Wang, X. L. Li, D. S. Shao, K. L. Luo, Z. G. Luo and G. R. Chen, *J. Energy Storage*, 2019, **25**, 100886.
101. A. Roos and J. Schoonman, *Solid State Ionics*, 1984, **13**, 205-211.
102. M. Gombotz, V. Pregartner, I. Hanzu and H. M. R. Wilkening, *Nanomaterials*, 2019, **9**, 1517.
103. F. Fujara, D. Kruk, O. Lips, A. F. Privalov, V. Sinitsyn and H. Stork, *Solid State Ionics*, 2008, **179**, 2350-2357.
104. N. Sorokin and B. Sobolev, *Physics of the Solid State*, 2011, **50**, 416-421.
105. K. Mori, Y. Morita, T. Saito, T. Kamiyama, T. Otomo, T. Abe and T. Fukunaga, *J. Phys. Chem. C*, 2020, **124**, 18452-18461.
106. K. Mori, A. Mineshige, T. Saito, M. Sugiura, Y. Ishikawa, F. Fujisaki, K. Namba, T. Kamiyama, T. Otomo, T. Abe and T. Fukunaga, *ACS Appl. Energy Mater.*, 2020, **3**, 2873-2880.
107. P. Molaiyan and R. Witter, *Mat Design Process Comm.*, 2019, **2**, e76.

108. *US Pat.,* US9166249B2, 2015.
109. *EP Pat.,* EP3719908A1, 2020.
110. *WO Pat.,* WO2020118108A1, 2020.
111. *WO Pat.,* WO2019188358A1, 2019.
112. *DE Pat.,* DE102017108650A1, 2017.
113. F. Gschwind and J. Bastien, *J. Mater. Chem. A*, 2015, **3**, 5628-5634.
114. K. Takahashi, A. Yokoo, Y. Kaneko, T. Abe and S. Seki, *Electrochem.*, 2020, **88**, 310-313.
115. K.-i. Okazaki, Y. Uchimoto, T. Abe and Z. Ogumi, *ACS Energy Lett.*, 2017, **2**, 1460-1464.
116. H. Konishi, T. Minato, T. Abe and Z. Ogumi, *J. Electrochem. Soc.*, 2017, **164**, A3702-A3708.
117. H. Konishi, T. Minato, T. Abe and Z. Ogumi, *J. Electroanal. Chem.*, 2018, **826**, 60-64.
118. H. Konishi, T. Minato, T. Abe and Z. Ogumi, *Chem. Lett.*, 2018, **47**, 1346-1349.
119. H. Konishi, T. Minato, T. Abe and Z. Ogumi, *J. Electroanal. Chem.*, 2020, **871**, 114103.
120. H. Konishi, T. Minato, T. Abe and Z. Ogumi, *J. Phys. Chem. C*, 2019, **123**, 10246-10252.
121. H. Konishi, T. Minato, T. Abe and Z. Ogumi, *ChemistrySelect*, 2020, **5**, 6237-6241.
122. H. Konishi, T. Minato, T. Abe and Z. Ogumi, *ChemistrySelect*, 2019, **4**, 5984-5987.
123. J. Haruyama, K. I. Okazaki, Y. Morita, H. Nakamoto, E. Matsubara, T. Ikeshoji and M. Otani, *ACS Appl Mater Interfaces*, 2020, **12**, 428-435.
124. T. Yamanaka, A. C. Kucuk, Z. Ogumi and T. Abe, *ACS Appl. Energy Mater.*, 2020, **3**, 9390-9400.
125. H. Konishi, T. Minato, T. Abe and Z. Ogumi, *Mater. Chem. Phys.*, 2019, **226**, 1-5.
126. V. K. Davis, S. Munoz, J. Kim, C. M. Bates, N. Momčilović, K. J. Billings, T. F. Miller, R. H. Grubbs and S. C. Jones, *Mater. Chem. Front.*, 2019, **3**, 2721-2727.
127. T. Yamamoto, K. Matsumoto, R. Hagiwara and T. Nohira, *ACS Appl. Energy Mater.*, 2019, **2**, 6153-6157.
128. Z. Zhang, X. Hu, Y. Zhou, S. Wang, L. Yao, H. Pan, C.-Y. Su, F. Chen and X. Hou, *J. Mater. Chem. A*, 2018, **6**, 8244-8250.
129. X. Hou, Z. Zhang, K. Shen, S. Cheng, Q. He, Y. Shi, D. Y. W. Yu, C.-y. Su, L.-J. Li and F. Chen, *J. Electrochem. Soc.*, 2019, **166**, A2419-A2424.
130. I. Mohammad and R. Witter, *Mater. Lett.*, 2019, **244**, 159-162.
131. R. A. Huggins, *Energy Storage*, Springer, New York, 2010.
132. R. Koerver, W. Zhang, L. de Biasi, S. Schweidler, A. O. Kondrakov, S. Kolling, T. Brezesinski, P. Hartmann, W. G. Zeier and J. Janek, *Energ Environ Sci*, 2018, **11**, 2142-2158.
133. S. Luo, K. Wang, J. Wang, K. Jiang, Q. Li and S. Fan, *Adv. Mater.*, 2012, **24**, 2294-2298.
134. M. A. Nowroozi, K. Wissel, M. Donzelli, N. Hosseinpourkahvaz, S. Plana-Ruiz, U. Kolb, R. Schoch, M. Bauer, A. M. Malik, J. Rohrer, S. Ivlev, F. Kraus and O. Clemens, *Comms. Mater*, 2020, **1**, 27.
135. T. Takami, T. Saito, T. Kamiyama, K. Kawahara, T. Fukunaga and T. Abe, *APL Mater.*, 2020, **8**, 051103.
136. K. Wissel, R. Schoch, T. Vogel, M. Donzelli, G. Matveeva, U. Kolb, M. Bauer, P. R. Slater and O. Clemens, *Chem. Mater.*, 2020, DOI: 10.1021/acs.chemmater.0c01762.
137. M. A. Nowroozi and O. Clemens, *ACS Appl. Energy Mater.*, 2018, **1**, 6626−6637.
138. S. Vasala, A. Jakob, K. Wissel, A. I. Waidha, L. Alff and O. Clemens, *Adv. Electron. Mater.*, 2019, **6**, 1900974.
139. M. A. Nowroozi, B. de Laune and O. Clemens, *ChemistryOpen*, 2018, **7**, 617-623.
140. O. Clemens, C. Rongeat, M. A. Reddy, A. Giehr, M. Fichtner and H. Hahn, *Dalton Trans.*, 2014, **43**, 15771-15778.
141. M. Hammad Fawey, V. S. Chakravadhanula, M. A. Reddy, C. Rongeat, T. Scherer, H. Hahn, M. Fichtner and C. Kubel, *Microsc. Res. Tech.*, 2016, **79**, 615-624.

142. A. Grenier, A.-G. Porras-Gutierrez, H. Groult, K. A. Beyer, O. J. Borkiewicz, Karena W. Chapman and D. Dambournet, *J. Mater. Chem. A*, 2017, **5**, 15700-15705.
143. H. Konishi, T. Minato, T. Abe and Z. Ogumi, *ChemistrySelect*, 2020, **5**, 4943-4946.
144. T. Yamanaka, K. Okazaki, Z. Ogumi and T. Abe, *ACS Appl. Energy Mater.*, 2019, **2**, 8801-8808.
145. T. Yamanaka, K. I. Okazaki, T. Abe, K. Nishio and Z. Ogumi, *ChemSusChem*, 2019, **12**, 527-534.
146. J. L. MacManus, D. J. Fray and J. E. Evetts, *Physica C*, 1991, **184**, 172-184.
147. M. H. Delville, D. Barbut, A. Wattiaux, J. M. Bassat, M. Menetrier, C. Labrugere, J. C. Grenier and J. Etourneau, *Inorg. Chem.*, 2009, **48**, 7962-7969.
148. T. Ishihara, *Perovskite Oxide for Solid Oxide Fuel Cells*, Springer, 2009.
149. J. M. Longo; and P. M. Raccah, *J. Solid State Chem.*, 1973, **6**, 526-531.
150. C. Bansal, H. Kawanaka, H. Bando, A. Sasahara, R. Miyamoto and Y. Nishihara, *Solid State Commun.*, 2003, **128**, 197-202.
151. T. D. Thanh, H. T. Van, D. T. A. Thu, L. V. Bau, N. V. Dang, D. N. H. Nam, L. V. Hong and S. C. Yu, *IEEE Trans. Magn.*, 2017, **53**, 1-4.
152. D. E. Bugaris and J. A. Ibers, *Dalton Trans.*, 2010, **39**, 5949-5964.
153. S. J. Skinner and G. Amow, *J. Solid State Chem.*, 2007, **180**, 1977-1983.
154. J. Cho, Y. W. Kim, B. Kim, J. G. Lee and B. Park, *Angew. Chem. Int. Ed.*, 2003, **42**, 1618-1621.
155. M. J. Lee, S. Lee, P. Oh, Y. Kim and J. Cho, *Nano Lett.*, 2014, **14**, 993-999.
156. S. C. C. A. Yamada, and K. Hinokuma, *J. Electrochem. Soc.*, 2001, **148**, A224-A229.
157. L. D. Aikens, R. K. Li and C. Greaves, *Chem. Commun.*, 2000, **21**, 2129-2130.
158. L. D. Aikens, L. J. Gillie, R. K. Li and C. Greaves, *J. Mater. Chem.*, 2002, **12**, 264-267.
159. C. Greaves and M. G. Francesconi, *Curr. Opin. Solid State Mater. Sci.*, 1998, **3**, 132-136.
160. O. Clemens and P. R. Slater, *Rev. Inorg. Chem.*, 2013, **33**, 105-117.
161. P. Slater and L. Driscoll, in *Photonic and Electronic Properties of Fluoride Materials*, eds. A. Tressaud and K. Poeppelmeier, Elsevier, Boston, 1st edn., 2016, DOI: 10.1016/b978-0-12-801639-8.00018-0, pp. 401-421.
162. E. E. McCabe and C. Greaves, *J. Fluorine Chem.*, 2007, **128**, 448-458.
163. K. Wissel, J. Heldt, P. B. Groszewicz, S. Dasgupta, H. Breitzke, M. Donzelli, A. I. Waidha, A. D. Fortes, J. Rohrer, P. R. Slater, G. Buntkowsky and O. Clemens, *Inorg. Chem.*, 2018, **57**, 6549-6560.
164. B. P. de Laune and C. Greaves, *J. Solid State Chem.*, 2012, **187**, 225-230.
165. W. Zaheer, J. L. Andrews, A. Parija, F. P. Hyler, C. Jaye, C. Weiland, Y.-S. Yu, D. A. Shapiro, D. A. Fischer, J. Guo, J. M. Velázquez and S. Banerjee, *ACS Energy Lett.*, 2020, DOI: 10.1021/acsenergylett.0c01328, 2520-2526.
166. B. P. de Laune, G. J. Rees, J. F. Marco, H. Y. Hah, C. E. Johnson, J. A. Johnson, F. J. Berry, J. V. Hanna and C. Greaves, *Inorg. Chem. Commun.*, 2017, **56**, 10078-10089.
167. A. K. Padhi, K. S. Nanjundaswamy and J. B. Goodenough, *J. Electrochem. Soc.*, 1997, **144**, 1188-1197.
168. T. Yamamoto and H. Kageyama, *Chem. Lett.*, 2013, **42**, 946-953.
169. S. T. Hartman and R. Mishra, *Journal of Materials Chemistry A*, 2020, DOI: 10.1039/d0ta06162j.
170. K. Wissel, S. Dasgupta, A. Benes, R. Schoch, M. Bauer, R. Witte, A. D. Fortes, E. Erdem, J. Rohrer and O. Clemens, *J. Mater. Chem. A*, 2018, **6**, 22013-22026.
171. K. Wissel, A. M. Malik, S. Vasala, S. Plana-Ruiz, U. Kolb, P. R. Slater, I. da Silva, L. Alff, J. Rohrer and O. Clemens, *Chem. Mater.*, 2020, **32**, 3160-3179.
172. K. Wissel, T. Vogel, S. Dasgupta, A. D. Fortes, P. R. Slater and O. Clemens, *Inorg Chem*, 2020, **59**, 1153-1163.

173. Y. Matsuo, J. Inamoto, A. Mineshige, M. Murakami, K. Matsumoto and R. Hagiwara, *Electrochem. Commun.*, 2020, **110**, 106626.
174. J. Janek and W. G. Zeier, *Nat. Energy*, 2016, **1**, 16141.
175. L. Duchêne, S. Lunghammer, T. Burankova, W.-C. Liao, J. P. Embs, C. Copéret, H. M. R. Wilkening, A. Remhof, H. Hagemann and C. Battaglia, *Chem. Mater.*, 2019, **31**, 3449-3460.
176. N. Jayaprakash, J. Shen, S. S. Moganty, A. Corona and L. A. Archer, *Angew. Chem. Int. Ed.*, 2011, **50**, 5904-5908.
177. W. Li, G. Zheng, Y. Yang, Z. W. Seh, N. Liu and Y. Cui, *Proc. Natl. Acad. Sci. USA*, 2013, **110**, 7148-7153.
178. Y. Liu, J. Wang, Y. Xu, Y. Zhu, D. Bigio and C. Wang, *J. Mater. Chem. A*, 2014, **2**, 12201-12207.
179. A. Sarkar, L. Velasco, D. Wang, Q. Wang, G. Talasila, L. de Biasi, C. Kubel, T. Brezesinski, S. S. Bhattacharya, H. Hahn and B. Breitung, *Nat Commun*, 2018, **9**, 3400.
180. K. G. Ranmohotti, E. Josepha, J. Choi, J. Zhang and J. B. Wiley, *Adv. Mater.*, 2011, **23**, 442-460.
181. R. A. Guidotti and P. Masset, *J. Power Sources*, 2006, **161**, 1443-1449.
182. J. W. B. a. W. L. Auxer, in *Handbook of Batteries*, eds. D. Linden and T. B. Reddy, McGraw-Hill, New York, 3rd edn., 2001, ch. 40, p. 1453.